RCA Review

June 1969 Volume 30 No. 2

RCA CORPORATION

DAVID SARNOFF, *Chairman of the Board*

ELMER W. ENGSTROM, *Chairman of the Executive Committee of the Board*

ROBERT W. SARNOFF, *President and Chief Executive Officer*

GEORGE E. MORRIS, *Secretary*

ERNEST B. GORIN, *Vice-President and Treasurer*

RCA RESEARCH AND ENGINEERING

J. HILLIER, *Executive Vice-President*

RCA LABORATORIES

W. M. WEBSTER, *Vice-President*

RCA REVIEW

C. C. FOSTER, *Manager*

R. F. CIAFONE, *Administrator*

AUG 4 19[illegible]

PRINTED IN U.S.A.

RCA REVIEW, published quarterly in March, June, September, and December by RCA Research and Engineering, RCA Corporation, Princeton, New Jersey 08540. Entered as second class matter July 3, 1950 under the Act of March 3, 1879. Second-class postage paid at Princeton, New Jersey, and at additional mailing offices. Subscription price in the United States and Canada: one year $4.00, two years $7.00, three years $9.00; in other countries, one year $4.40, two years $7.80, three years $10.20. Single copies up to five years old $2.00. For copies more than five years old, contact Walter J. Johnson, Inc., 111 Fifth Ave., New York, N. Y. 10003.

RCA REVIEW

a technical journal

Published quarterly by

RCA RESEARCH AND ENGINEERING

in cooperation with all subsidiaries and divisions of the

RCA CORPORATION

VOLUME 30	JUNE 1969	NUMBER 2

CONTENTS

PAGE

Digit-by-Digit Transcendental-Function Computation 209
R. J. LINHARDT AND H. S. MILLER

Transmission and Reflection Group Delay of Butterworth, Chebychev, and Elliptic Filters 248
C. M. KUDSIA AND N. K. M. CHITRE

High-Frequency Behavior of Microstrip Transmission Lines 268
L. S. NAPOLI AND J. J. HUGHES

Single-Frequency Argon Laser 277
L. GOROG AND F. W. SPONG

Vapor Pressure Data for the Solid and Liquid Elements 285
R. E. HONIG AND D. A. KRAMER

The Effect of Barrier Recombination on Production of Hot Electrons in a Metal by Forward Bias Injection in a Schottky Diode 306
R. WILLIAMS

Current–Voltage Characteristics of Silver-n-Type GaP Schottky Barriers 314
C. R. WRONSKI

Double Injection Electroluminescence in Anthracene 322
J. DRESNER

Switching and Storage Characteristics of MIS Memory Transistors .. 335
J. T. WALLMARK AND J. H. SCOTT

Theory of the Switching Behavior of MIS Memory Transistors 366
E. C. ROSS AND J. T. WALLMARK

RCA Technical Papers 382

Patents 385

Authors 389

© 1969 by RCA Corporation
All rights reserved.

RCA REVIEW is regularly abstracted and indexed by *Abstracts of Photographic Science and Engineering Literature, Applied Science and Technology Index, Bulletin Signalétique des Télecommunications, Chemical Abstracts, Electronic and Radio Engineer, Mathematical Reviews,* and *Science Abstracts* (I.E.E.-Brit.).

RCA REVIEW

BOARD OF EDITORS

Chairman
J. A. RAJCHMAN
RCA Laboratories

E. D. BECKEN
RCA Communications, Inc.

G. H. BROWN
RCA Patents and Licensing

A. L. CONRAD
RCA Education Systems

A. N. GOLDSMITH
Honorary Vice President, RCA

N. L. GORDON
RCA Laboratories

G. B. HERZOG
RCA Laboratories

J. HILLIER
RCA Research and Engineering

R. S. HOLMES
RCA Research and Engineering

E. O. JOHNSON
RCA Electronic Components

H. W. LEVERENZ
RCA Patents and Licensing

H. R. LEWIS
RCA Laboratories

D. S. MCCOY
RCA Laboratories

L. S. NERGAARD
RCA Laboratories

H. F. OLSON
RCA Laboratories

K. H. POWERS
RCA Laboratories

P. RAPPAPORT
RCA Laboratories

F. D. ROSI
RCA Laboratories

L. A. SHOTLIFF
RCA International Licensing

T. O. STANLEY
RCA Laboratories

W. M. WEBSTER
RCA Laboratories

E. C. HUGHES
RCA Electronic Components

Secretary
C. C. FOSTER
RCA Research and Engineering

REPUBLICATION AND TRANSLATION

Original papers published herein may be referenced or abstracted without further authorization provided proper notation concerning authors and source is included. All rights of republication, including translation into foreign languages, are reserved by RCA Review. Requests for republication and translation privileges should be addressed to *The Manager*.

DIGIT-BY-DIGIT TRANSCENDENTAL-FUNCTION COMPUTATION*

BY

R. J. LINHARDT† AND H. S. MILLER‡

Summary—A very fast new algorithm for computer evaluation of transcendental functions is described. This algorithm was designed for hardware implementation in the LIMAC computer. The hardware implementation of the new algorithm is more than three times as fast as the software polynomial approximation while hardware implementation of the polynomial approximation method yields only a 10% speed increase over the software method. The accuracy of the new method is better than two parts in 2^n, where n is the number of bits in the word.

INTRODUCTION

THE DIGIT-BY-DIGIT method of numerical computation has been known for a long time.[1-4] One of its earliest applications occurred in 1624 when Briggs used this method to generate his table of logarithms. In recent times, this technique has been developed and expanded by J. R. Volder[1] in coordinate-rotation and conversion problems and by J. E. Meggitt[2] for general arthimetic subroutines. Other applications by digit-by-digit computations are contained in References (3) and (4). The application of digit-by-digit computational methods to the evaluation of transcendental functions is particularly

* The research reported in this paper was jointly supported by the Air Force Avionics Laboratory, Air Force Systems Command, Wright-Patterson Air Force Base, Ohio, under contract No. AF33(615)3491, and by RCA Laboratories.

† RCA Information Systems Division, Camden, N. J.

‡ RCA Laboratories, Princeton, N. J.

[1] J. E. Volder, "The CORDIC Trigonometric Computing Technique", *IRE Transactions on Elec. Computers*, Vol. EC-8, pp. 330-334, September 1959.

[2] J. E. Meggitt, "Pseudo Division and Pseudo Multiplication Processes", *IBM J. of Res. and Devel.*, pp. 210-226, April 1962.

[3] G. Sideus, "Inertial Navigation at a Bargain Price", *Electronics*, pp. 108-112, May 17, 1965.

[4] J. M. Parini, "Divic Gives Answer to Complex Navigation Questions", *Electronics*, pp. 105-111, September 5, 1966.

attractive, since the logical structure of the algorithms is nearly identical to those of multiplication and nonrestoring division found in most computers.[5] This near equivalence in logical structure enables evaluation of transcendental functions in an amount of time that approaches the sum of one multiplication and one division time. The accuracies of the digit-by-digit algorithms are within two parts out of 2^n where n is the number of bits in the word.

This paper develops the digit-by-digit algorithms including evaluation of sine, cosine, arctangent, and the hyperbolic functions of sinh, cosh, and arctanh.

Compatible algorithms for square root and natural logarithms were investigated, and it was found that for the square root the iteration equations, unlike those for sine/cosine, etc., become data dependent. Thus, the logical structure of the square-root algorithm does not retain the same simple structure as those for sine and cosine, etc. For natural logarithms, the iteration equations introduce an error each time an addition step occurs in the nonrestoring division-like process. This error is negligible for the least-significant bits of the quotient, but it could amount to 25% for the most significant bit. The results of these two investigations are contained in Appendixes I and II.

A detailed evaluation of polynomial methods of transcendental-function computation is contained in Appendix III. The results of this investigation led to the selection of the digit-by-digit algorithms for implementation in the experimental Large Integrated Monolithic Array Computer (LIMAC).[6,7] In particular, it was found that construction in hardware of a polynomial evaluator for a one-address machine would provide, on the average, only a 10% improvement in evaluation speed over an all-software evaluation implementation. Increased speed is gained only through the reduction in total instruction "overhead time" (i.e., time consumed for instruction address incrementing, instruction fetching, instruction operation code decoding, operand address generation, and operand fetching), and since argument reduction prior to polynomial evaluation requires a significant number of instructions, the hardward polynomial evaluator has little to offer. In contrast, digit-by-digit algorithms are over three times faster than an all-software evaluation.

---

[5] I. Flores, *The Logic of Computer Arithmetic*, Prentice-Hall, 1963.

[6] S. Y. Levy, et al., "System Utilization of Large-Scale Integration," *IEEE Transactions on Electronic Computers*, Vol. EC- 16, No. 5, pp. 562-566, October 1967.

[7] H. R. Beelitz, et al., "System Architecture for Large-Scale Integration," *AFIPS Conference Proceedings*, Vol. 30 (1967 FJCC), pp. 185-200, November 1967.

BRIGGS' METHOD

Briggs computed logarithms of numbers not much greater than unity by using the approximation.

$$\ln(1+x) \approx x - \frac{1}{2}x^2, \quad x < 1.$$

Logarithms of numbers greater than unity were obtained by expressing these large numbers as a product of smaller numbers; each of these smaller numbers was less than two. This procedure provided Briggs with a "boot strap" approach to compiling his table of logarithms.

Generally, any number Y such that $1 < Y < 1000$ can be represented as a product of simple factors to an accuracy of n significant digits

$$Y = \prod_{j=0}^{n} (1 + 10^{-j})^{q_j} \tag{1}$$

where q_j is an integer (0, 1, 2, 3, 4, 5. 6, 7, 8. 9) that gives the number of times the factor $(1 + 10^{-j})$ is to be used. The q_j's can be determined successively, starting with the initial value $j = 0$. The procedure is as follows:

The maximum number of integer times that Y is divisible by $(1 + 10^{-0})$ is q_0. The remainder of this division process becomes the new number Y_1. Then q_1 is the maximum number of integers times Y_1 is divisible by $(1 + 10^{-1})$ with a remainder of Y_2. For example,

$$\begin{aligned} Y &= 19.66 \\ &= (2)^4(1.1)^2(1.01)^1(1.001)^5(1.0001)^4 \end{aligned}$$

where $q_0 = 4$, $q_1 = 2$, $q_2 = 1$, $q_3 = 5$, $q_4 = 4$, and $n = 4$. If we take the log of both sides of Equation (1), we obtain

$$\log Y = \sum_{j=0}^{n} q_j \log(1 + 10^{-j}) . \tag{2}$$

Again, for our example,

$$\begin{aligned} \log 19.66 = 4 \log(1 + 10^0) + 2 \log(1 + 10^{-1}) + \log(1 + 10^{-2}) \\ + 5 \log(1 + 10^{-3}) + 4 \log(1 + 10^{-4}) = 1.29357 \end{aligned}$$

From 5-place log tables, $\log(19.66) = 1.29358$.

The calculation for log Y can be split into two parts as shown in Equations (1) and (2) and as illustrated by the example. In Equation (1) the digits q_j are calculated in a process that resembles division: Y_j is the partial remainder and q_j is the quotient digit; after each q_j is determined, the divisor is modified to a new constant. In Equation (2), the logarithm is calculated from stored constants, log $(1 + 10^{-j})$, in a process that resembles multiplication: the multiplier is the string of digits q_j; the multiplicand is changed to a new constant after each step; and the answer is developed as the product.

The object in developing these algorithms is to arrange the generation of the desired function into a form that permits this two-part type of evaluation. In all cases one step should closely resemble the division process while the other step resembles the multiplication process. In this way a standard hardware multiplier and divider can be converted into a transcendential function generator by means of a small amount of additional control logic and storage provision for a few constants. Figure 1 shows the functional flow of a basic, binary, nonrestoring divider and Figure 2 the functional flow of a basic binary multiplier. This is the starting point of the formal development of the digit-by-digit algorithms.

Sine and Cosine Algorithm

Consider the sine and cosine of an angle θ as the ordinate and abscissa, respectively, of a unit vector rotated from the zero axis through an angular displacement of θ. This rotation can be performed in a number of fixed predetermined step rotations, e.g., $\pm \pi/2$, $\pm \pi/4$, $\pm \pi/8$, ... The first part in a two-part algorithm for the evaluation of the sine and cosine is to transform this angle θ into a string of standard component parts. For example,

$$128^\circ \cong 90^\circ + 45^\circ - 22.5^\circ + 11.3^\circ + 5.7^\circ - 2.9^\circ + 1.5^\circ - 0.8^\circ.$$

Rotation of a unit vector starting from the positive abscissa through this sequence of standard angular increments is the second part of this two-part sine/cosine algorithm. The direction of rotation for each increment was determined in part 1. Projections of the unit vector on the ordinate and abscissa are, of course, the sine and cosine of the angle θ. The virtue of this two-part algorithm is that a division procedure transforms the angle θ into a string of standard angular increments, and a multiplication procedure performs the rotation of the unit vector with the sine and cosine values residing in the multiplicand and product registers at the conclusion of this algorithm. This two-part algorithm is described in detail as follows.

Part 1

Angle θ is the dividend while the divisor is an angular constant, a constant that is changed before a new quotient digit is generated. The quotient is generated as a series of "1's" and "0's"; if the angular constant is added to the partial remainder (divisor initially) the quotient digit is "0"; otherwise, the angular constant is subtracted from the partial remainder and the quotient digit is "1". The divisor or angular constant is changed at each step in the division cycle; the most significant constant is used first. As is the case of normal nonrestoring division (Figure 1), a negative partial remainder calls for the addition of

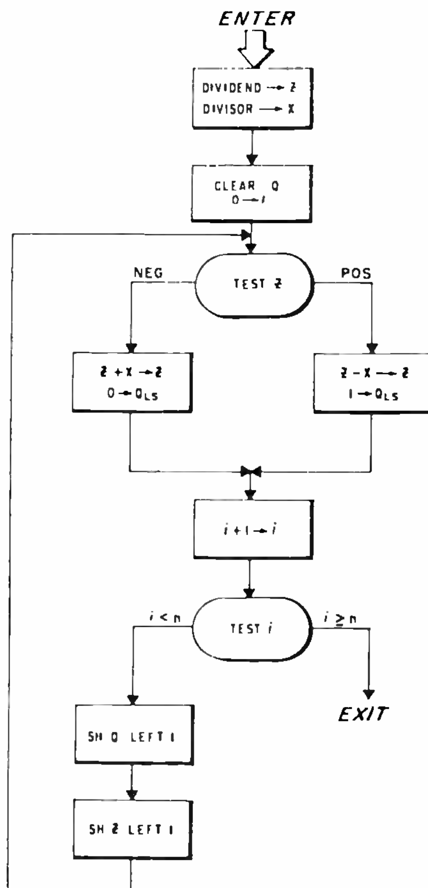

Fig. 1—Functional flow binary nonrestoring divider.

the divisor (angular constant here) and a positive partial remainder calls for subtraction.

Part 1 uses the recursive equation

$$Z_{i+1} = 2(Z_i \pm 2^i \tan^{-1} 2^{-i}), \quad i = 0, 1, \ldots n$$

where Z_i represents the partial remainder and the factor $(2^i \tan^{-1} 2^{-i})$ represents leftward displacements of the angular constants 90°, 45°. 26.5°, 14.0°, etc.

In effect, Part 1 of this algorithm starts with a vector displaced from the positive abscissa axis by the angle θ and rotates it through a series of ever decreasing angular increments. The sum of all these

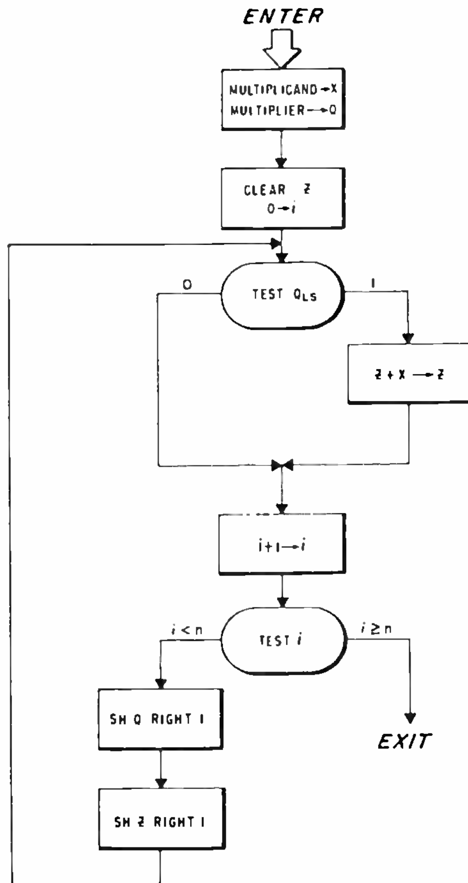

Fig. 2—Functional flow binary multiplier.

rotational steps, if taken in the same direction, must at least equal the maximum value of the angle θ. Similarly successive rotational steps should differ from each other by a factor either equal to or slightly less than two. The accuracy attainable depends on the number of step rotations used. For angles between −180° and +180°, eight steps are required to obtain accuracies of better than one degree. A quotient digit of "1" can be interpreted as a counter-clockwise rotation, "0" as a clockwise rotation.

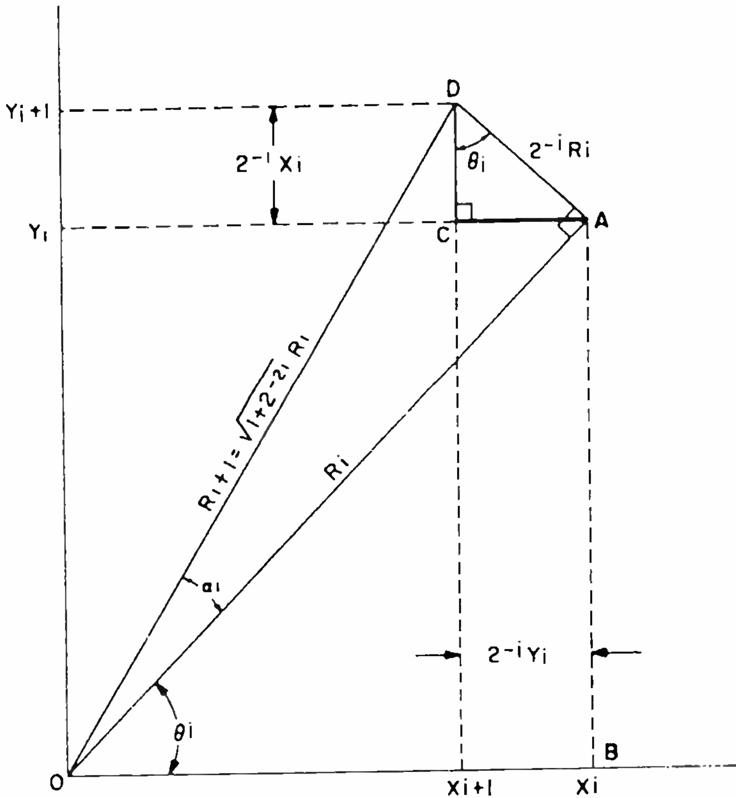

Fig. 3—Rotation vector diagram.

Part 2

In Figure 3, assume that we have just finished the ith rotational step and the vector is positioned as shown by R_i. Further, assume that we are to rotate R_i *counterclockwise* by α_i to obtain the vector position R_{i+1}. (The angular rotation α_i chosen for any step rotation is the angle whose tangent is 2^{-i}.) The side AD of triangle OAD is $2^{-i}R_i$. Right-triangle DCA is similar to triangle OBA, and therefore, CA $= 2^{-i}Y_i$ and CD $= 2^{-i}X_i$, and we obtain the following relationships:

$$Y_{i+1} = Y_i + 2^{-i}X_i$$

$$X_{i+1} = X_i - 2^{-i}Y_i$$

A *clockwise* rotation of R_i by α_i would only change the signs of the modifying terms; so the general equations are,

$$Y_{i+1} = Y_i \pm 2^{-i}X_i \tag{3}$$

$$X_{i+1} = X_i \mp 2^{-i}Y_i . \tag{4}$$

Although the recursion Equations (3) and (4) are derived with an increasing index value i, they could have been derived with a decreasing index value, namely,

$$Y_{i-1} = Y_i \pm 2^{-i}X_i \tag{3a}$$

$$X_{i-1} = X_i \mp 2^{-i}Y_i \tag{4a}$$

Looking again at Figure 3, we observe that the vector increases in magnitude after each rotation by a factor $\sqrt{1 + 2^{-2i}}$. Therefore, to obtain a unit vector after n rotations, the vector should initially be less than unity, namely,

$$\frac{1}{\prod_{i=0}^{n} \sqrt{1 + 2^{-2i}}} \tag{5}$$

and this is the initial value of X (abscissa) while the initial value of Y (ordinate) is zero. The final value of X after n rotations is the cosine of the angle, while the final value of Y is the sine of the angle.

The directions of incremental rotations for the unit vector of Part 2 were determined in Part 1 of this sine and cosine algorithm. These directions are indicated by "1's" and "0's" stored in the quotient register. The direction indicator bit for the largest rotation had to be determined first and corresponds to the most significant bit in the quotient register. Since Part 1 was inherently a division type of process, Part 2 should be a multiplication type of process using the quotient register now as the multiplier register. The old partial remainder register now becomes the partial product register.

The recursive ordering in Part 1 was *most significant* to *least significant* ($i = 0$ to n) and conforms with the ordering in classical divi-

sion. Part 2 is a multiplication-type process, and while it is possible to implement the algorithm with a most-to-least ordering, it is more convenient to use the recursion Equation (3a) and (4a) with a *least significant* to *most significant* ($i = n$ to 0) ordering and conform to the ordering in classical multiplication.

To aid in the mechanization of this function, we can make the following substitution in the general Equations (3a) and (4a):

$$Z_i = 2^i Y_i ,$$

which gives the following recursion equations

$$Z_{i-1} = 2^{-1}(Z_i \pm X_i) \tag{6}$$

$$X_{i-1} = X_i \mp 2^{-2i} Z_i \tag{7}$$

The substitution of Z for Y requires no transformation in initial conditions or final value since, as previously stated, the initial value of Y is zero (i.e., $Y_n = Z_n = 0$) and the final value of Z is Z_0 (i.e., $Z_0 = 2^0 Y_0 = Y_0$). The contents of an accumulator are represented by Z_i, to which the contents of the multiplicand register X_i are either added or subtracted as signified by a "1" or "0" multiplier bit, respectively. A subsequent right shift of the accumulator implements the division by two. Updating the multiplicand register by the factor $(2^{-2i}Z_i)$ completes the cycle. The factor $(2^{-2i}Z_i)$ is developed in an auxiliary register at the start of a new cycle.

This procedure chosen for Part 2 starts by adding the contribution of the $\tan^{-1} 2^{-n}$ rotation and concludes with the contribution of the $\tan^{-1} 2^0$ (or 45°) rotation. The algorithm can be extended beyond an angular range of 45°. For example, a 90-degree rotation of any vector is identical to interchanging the X and Y components and reversing the sign of either the X or Y component, depending on quadrant location of the vector and the direction of rotation. A 180-degree rotation is accomplished by changing the signs (form 2's complements) of the two components.

Consider an example in which we want to find the sine and cosine of 142°. Expressed in radians, 142° is 0.789 π radians or, in binary, 0.1100101 π radians.

In Part 1 we place the angle as a binary fraction of π radians in the Z (or accumulator) register, which is equivalent to the dividend in the division process. This is shown in Figure 4. Since in our case the sign of the Z register is positive, we subtract a predetermined

stored divisor of 90° expressed as a binary fraction of π radians (called Step 1). The subtraction places a "1" in the Q register signifying a counter-clockwise rotation. This procedure continues with the direction of rotation determined by the sign of Z. New subtrahends or addends equal to the angle whose tangent is 2^{-i} expressed

$Z_{i+1} = 2(Z_i \pm 2^i X_i)$ $X_i = \arctan 2^{-i}$

Z	X	Q
0.1100101	0.1000000	1
−0.1000000		
0.0100101		
0.1001010	0.0100000	11
−0.1000000		
0.0001010		
0.0010100	0.0010010	111
−0.1001000		
1.1001100		
1.0011000	0.0001001	1110
+0.1001000		
1.1100000		
1.1000000	0.0000101	11100
+0.1010000		
0.0010000		
0.0100000	0.0000010	111001
−0.1000000		
1.1100000		
1.1000000	0.0000001	1110010
+0.1000000		
0.0000000		

Fig. 4—Sine-cosine, Part 1.

as a binary fraction of π radians are introduced and shifted $(i+1)$ places to the left. After the addition or subtraction, Z and Q are shifted left one place and the procedure continued until $i = n$.

The shift is a result of employing a division type of process. When the Z register is positive, the next operation is a subtraction and a "1" is entered into the least significant bit of Q. When the Z register is negative, the next operation is an addition and a "0" is entered into the least significant bit of Q. The results shown in Figure 4 give, for $n = 5$, a Q of 1110010 or

$$142° = 90 + 45 + 26.5 - 14 - 7.1 + 3.6 - 1.8$$

Thus, Part 1 is a binary nonrestoring division process with the divisor changed after each bit of the quotient is generated.

Figure 5 details Part 2 in the calculation of this sine and cosine algorithm. The initial value of X is computed from Equation (5) with n set equal to 5 and the initial value of Z is 0. The procedure for Part 2 is essentially the mechanization of Equations (6) and

	$Z_{i-1} = 2^{-1}(Z_i \pm X_i)$	$X_{i-1} = X_i \mp 2^{-2i} Z_i$	
i	Z	X	Q
	00.0000000	0.1001101	.1110010
5	−0.1001101	+0.0000000	
	11.0110011	0.1001101	
	11.1011001	0.1001101	.111001
4	+0.1001101	−1.1111111	
	00.0100110	0.1001110	
	00.0010011	0.1001110	.11100
3	−0.1001110	+0.0000000	
	11.1000101	0.1001110	
	11.1100010	0.1001110	.1110
2	−0.1001110	+1.1111110	
	11.0010100	0.1001100	
	11.1001010	0.1001100	.111
1	+0.1001100	−1.1110010	
	00.0010110	0.1011010	
	00.0001011	0.1011010	11
0	+0.1011010	−0.0001011	
	00.1100101	0.1001111	
−1	00.1001111	0.1100101	1
	00.1001111	1.0011010	

Fig. 5—Sine-cosine, Part 2.

(7) with the upper sign used when the quotient bit is 1 and the lower sign when the quotient bit is 0. The $(i = -1)$ step is the 90-degree rotation, which is an interchange of the X and Z registers. Since both registers are positive, the vector is in the first quadrant. A counterclockwise rotation of 90 degrees places the vector in the second quadrant, which requires the X register to be complemented. The final content of the Z register is the cosine of the angle. The results obtained for $n = 5$ and a 7-bit word (two decimal digits accuracy) are

$$\text{sine } 142° = 0.6157 \text{ actual}$$

$$= 0.617 \text{ calculated}$$

$$\text{cosine } 142° = 0.7880 \text{ actual}$$

$$= 0.789 \text{ calculated}$$

The mechanization of the sine and cosine functions requires a minimum of four storage locations, which we shall call the Z, Q, X and M registers. In Part 1 of the algorithm, we use only Z, Q, and X registers. The Z register contains initially the angle whose sine and cosine is required in terms of a fraction of π radians (negative angles are expressed as a two's complement fraction of π radians). Register X contains the angular increment constants while Q indicates the resultant direction of rotation for each increment. In Part 2 of the algorithm, we use all four registers. The initial value of X is determined by Equation (5), and the initial value of Z is zero. As in Part 1, the Q register holds the direction of rotation for each increment. The M register is used as temporary storage to hold the value of $2^{-2i}Z_i$ of Equation (7). After the M register is loaded, the Z register is updated as in Equation (6) followed by updating the X register is in Equation (7). As previously stated, the final contents of the Z register are the sine of the angle, while the final contents of the X register are the cosine of the angle.

Arctangent Algorithm

The arctangent is generated by reversing the sine and cosine algorithm. In the evaluation of the arctangent of (Y/X), the X and Y components of the vector are given, and the procedure is to rotate the vector back to the positive X axis. The angle traversed is the angle whose tangent is Y/X and, therefore, is the solution.

Again the evaluation procedure is split into two parts. In the first part, the rotational directions are determined by using the recurrence relation in a division type of process, as in Part 2 in the sine-cosine evaluation. But, the sign of the Z register (not the value of the Q bit as before) determines the sign of the modifier term and the value of the Q bit. Also, the recurrence relations must be written in the forward direction as follows:

$$Z_{i+1} = 2(Z_i \pm X_i)$$

$$X_{i+1} = X_i \mp 2^{-2i}Z_i$$

The basic algorithm is limited to computations of angles between $-\pi/2$ and $\pi/2$ radians. The argument range can be extended to $\pm\pi$

radians by an argument reduction. Since the $\pi/2$ radians rotation essentially interchanges both variables and complements the appropriate one, this feature also will be used in the arctangent computation.

Part 2 of the process is a multiplication type of process, where the multiplier is the string of digits denoting the stepped rotational direction as generated in the Q register during Part 1. The multiplicand is changed after each multiplication step using the same string of stored constants ($\tan^{-1} 2^{-i}$) as in the sine-cosine computation.

	$Z_{i+1} = 2(Z_i \mp X_i)$	$X_{i+1} = X_i \pm 2^{-2i} Z_i$	
i	Z	X	Q
1	00.0101110	1.1000101	1
	00.0111011	0.0101110	
	00.0111011	0.0101110	11
0	-00.0101110	+0.0111011	
	00.0001101	0.1101001	
	00.0011010	0.1101001	111
1	-00.1101001	+0.0000110	
	11.0110001	0.1101111	
	10.1100010	0.1101111	1110
2	+00.1101111	-1.1110110	
	11.1010001	0.1111001	
	11.0100010	0.1111001	11100
3	+00.1110001	-1.1111110	
	00.0010011	0.1110011	
	00.0100110	0.1110011	111001
4	-00.1110011	+0.0000000	
	11.0101011	0.1110011	
	10.1010110	0.1110011	1110010
5	+00.1110011	-1.1111111	
	11.1001001	0.1110100	

Fig. 6—Arctan Y/X, Part 1.

For the evaluation of the arctangent (Y/X) the initial value of Z is the value of Y expressed as a binary fraction, and the initial value of X is the value of X also expressed as a binary fraction. For Part 2, the initial value of Z is zero and the X is $[2^i(\tan^{-1}2^{-i})]$ which will be added or subtracted depending on the value of the Q bit. The final value of Z is the angle whose tangent is (Y/X) and is expressed as a binary fraction π radians. Figures 6 and 7 give an example that demonstrates the reverse process of the sine-cosine calculation.

The initial conditions chosen correspond to the actual angle whose tangent is Y/X:

$$\alpha = \arctan \frac{0.3594}{-0.4531} = 141.58° \text{ actual}$$

From the algorithm demonstrated in Figures 6 and 7, we obtain for $n = 5$ (and a 7-bit, or two-decimal digit, word) the calculated value of α

$$\alpha = 0.789\ \pi \text{ radians}$$

$$\alpha = 142° \text{ calculated.}$$

Z_{i-1} $2^{-1}(Z_i \pm 2^i X_i)$ X_i arctan 2^{-i}

i	Z	X	Q
	0.0000000	0.0000001	1110010
5	-0.1000000		
	1.1000000		
	1.1100000	0.0000010	111001
4	+0.1000000		
	0.0100000		
	0.0010000	0.0000101	11100
3	-0.1010000		
	1.1000000		
	1.1100000	0.0001001	1110
2	-0.1001000		
	1.0011000		
	1.1001100	0.0010010	111
1	+0.1001000		
	0.0010100		
	0.0001010	0.0100000	11
0	+0.1000000		
	0.1001010		
	0.0100101	0.1000000	1
-1	+0.1000000		
	0.1100101		

Fig. 7—Arctan Y/X, Part 2.

Hyperbolic Functions

Hyperbolic vectors can be rotated in the same manner that trigonometric vectors were rotated to develop the sine-cosine and arctangent algorithms. In this case, however, the constants are the hyperbolic angles

$$\alpha_i = \tanh^{-1} 2^{-i}$$

A better insight into the analogy between rotation in trigonometric

and hyperbolic space is obtained from a graphical representation of hyperbolic functions as shown in Figure 8. Proceeding as we did for trigonometric functions (Figure 3) and using hyperbolic identities, we obtain the following relationships for hyperbolic functions:

$$X_i = R_i \cosh \gamma_i$$

$$Y_i = R_i \sinh \gamma_i$$

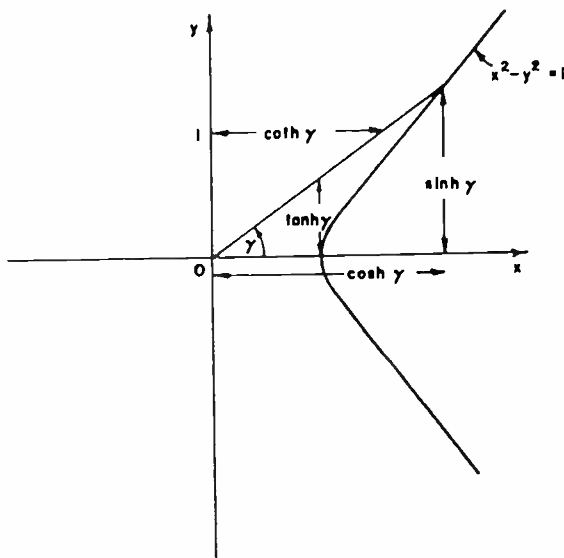

Fig. 8—The hyperbolic functions.

Again assume that the vector R_i is rotated by an increment $\pm \alpha_i$ where

$$\alpha_i = \tanh^{-1} 2^{-i}$$

or

$$\tanh \alpha_i = \frac{\sinh \alpha_i}{\cosh \alpha_i} = 2^{-i},$$

which reduces to

$$\cosh \alpha_i = \frac{1}{(1 - 2^{-2i})^{1/2}} \tag{8}$$

and

$$\sinh \alpha_i = \frac{2^{-i}}{(1 - 2^{-2i})^{1/2}}. \tag{9}$$

The recursive equations for hyperbolic rotations are

$$X_{i+1} = R_{i+1} \cosh (\gamma_i \pm \alpha_i) \tag{10}$$

$$Y_{i+1} = R_{i+1} \sinh (\gamma_i \pm \alpha_i) \tag{11}$$

Again using right-triangle relationships,

$$R_{i+1} = (1 - 2^{-2i})^{1/2} R_i . \tag{12}$$

Now, substituting Equations (8), (9), and (12) into Equation (10) and employing the identity function for $\cosh (\gamma_i \pm \alpha_i)$, we get

$$X_{i+1} = X_i \pm 2^{-i} Y_i . \tag{13}$$

In a similar fashion, substitution of Equations (8), (9), and (12) into Equation (11) yields

$$Y_{i+1} = Y_i \pm 2^{-i} X_i . \tag{14}$$

Equations (13) and (14) are the hyperbolic recursion equations for an increasing index, $i = 1$ to n. Similarly,

$$X_{i-1} = X_i \pm 2^{-i} Y_i \tag{13a}$$

$$Y_{i-1} = Y_i \pm 2^{-i} X_i \tag{14a}$$

are the recursive equations for a decreasing index.

As in the sine-cosine algorithm, the vector changes magnitude after each rotation. Therefore, to obtain a unit vector after n rotations one must initially start with the vector

$$\frac{1}{\prod_{i=1}^{n} (1 - 2^{-2i})^{1/2}}$$

Again, to aid in the mechanization of these functions, we make the substitution $Z_i = 2^i Y_i$. Equations (13a) and (14a) then yield

$$Z_{i-1} = 2^{-1}(Z_i \pm X_i) \tag{15}$$

$$X_{i-1} = X_i \pm 2^{-2i}Z_i \tag{16}$$

Thus, through use of a different set of constants and a slightly modified recursion routine, hyperbolic sine, cosine, and arctangent are obtained in the same arithmetic registers as the trigonometric functions sine, cosine, and arctangent. The exponential function e^γ is obtained by generating sinh γ and cosh γ and summing the two.

The natural logarithm function is obtained from the hyperbolic arctangent as follows:

$$d = \tanh \gamma = \frac{\sinh \gamma}{\cosh \gamma} \tag{17}$$

$$d = \frac{e^\gamma - e^{-\gamma}}{e^\gamma + e^{-\gamma}}$$

$$2\gamma = \ln\left[\frac{1+d}{1-d}\right],$$

or

$$\ln\left[\frac{1+d}{1-d}\right] = 2 \tanh^{-1} d\,.$$

Starting with an initial condition of $\gamma = (0.8)$ in Step 1, and proceeding in a manner identical to that shown in Figures 4 through 10, we obtain the following results:

	calculated	*actual*
$\sinh \gamma =$	0.867	0.8881
$\cosh \gamma =$	1.31	1.337
$e^\gamma =$	2.18	2.226

Also, starting with an initial condition of $Y = 0.1$ and $X = 0.5$, we obtain:

	calculated	*actual*
arctanh $Y/X =$	0.214	0.2028
$\ln\left(\frac{1+(Y/X)}{1-(Y/X)}\right) =$	0.429	0.4055

ACCURACY

The accuracy of the digit-by-digit methods has not been explored rigorously; however, preliminary checks show the accuracy to be sufficient for LIMAC.[6,7] Meggitt has stated that the only approximations occur when the shifted modifier is added to the divisor.[2] He showed that the worst-case error for decimal mechanization is a deviation of 2.5 in the last significant decimal digit. In LIMAC, constants will be stored in normalized form and the arithmetic word will be three extra bits in length to avoid elaborate round-off procedures.

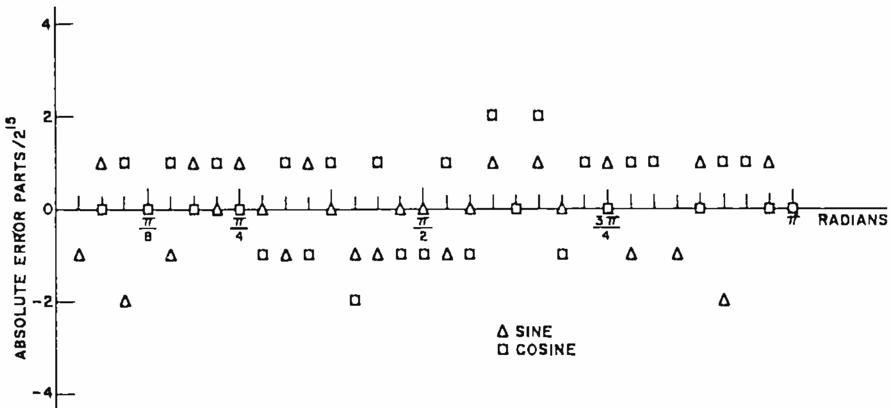

Fig. 9—Sine-cosine accuracy.

To obtain a check on the sine-cosine algorithm, the detailed mechanization steps of the algorithm, as it will appear in LIMAC, were programmed in FORTRAN for simulation on the RCA 601 computer. Sines and cosines were calculated in 32 equal steps from 0 to + 180° for 15 binary bits plus sign, as used in LIMAC, and were compared against the results of the double-precision sine-cosine subroutine available on the RCA 601 computer (this routine uses a polynomial approximation and provides a floating-point output of 108 binary bits). The absolute error obtained for truncation at 15 binary bits is shown in Figure 9. The results indicate an error of less than two parts in 2^{15}.

COMPARISON WITH POLYNOMIAL EVALUATION

Appendix III develops in detail the time requirements for evaluation of transcendental functions employing the more conventional numerical methods of polynomial approximations. The purpose of the

analysis is to provide a comparative basis for either implementing transcendental function evaluation with digit-by-digit techniques or retaining the polynomial method and enhancing performance by constructing in hardware a polynomial evaluator.

Total execution time with a polynomial approximation method is the sum of the time used in reducing the argument into the convergence range for the polynomial series approximation plus the time incurred in actual evaluation of the polynomial series. As polynomials are asked to converge over smaller ranges, the component of evaluation time decreases while the component of argument-reduction time increases. Tradeoffs can be made between argument reduction and series evaluation to achieve a minimum overall execution time given a set of machine parameters.

Rather than making an exhaustive determination in terms of the best tradeoffs for various sets of machine parameters, total execution time as well as each component for argument reduction and series evaluation times were determined for a rather common set of arithmetic unit parameters, namely:

$$\text{divide time} = 2 \text{ multiply times}$$

$$\text{multiply time} = n \text{ addition times}$$

where n is the number of binary bits in the arithmetic word. A subtraction time is assumed identical to an addition time and shift and compare times in the arithmetic logic are assumed to be negligible. Fixed-point arithmetic also was assumed (a floating-point representation only serves to increase the component of argument reduction time).

Enhanced execution time with the polynomial method will accrue only through the elimination of instruction overhead time (the sum of the times required to increment the instruction address, fetch the instruction from memory, decode the operation code, generate the operand address, and fetch the operand from memory) during the polynomial series evaluation by constructing in hardware a polynomial evaluator. Argument reduction for all the various transcendental functions has little in common and must remain in the software domain.

Thus, in order to determine by how much the total execution time will be enhanced with a polynomial evaluator, more machine parameters were assumed. A simple fetch–execute cycle and a one-address instruction format were selected. To carry out an arithmetic instruction, the instruction itself is first fetched from memory. A memory access is assumed to require one-half of a memory cycle. Within the

subsequent half-cycle, this instruction can be partially prepared for execution, i.e., operation code decoded and data-path gates set. At the start of the next memory cycle, the data word is accessed. Thus, 1.5 memory cycles are required to prepare a one-address instruction for execution.

Normally, one hardware addition can be performed within a memory half-cycle; two memory cycles allow for instruction preparation plus execution of one addition. Thus, with a logic-circuit pair delay selected as the unit of time measure, the assumed machine characteristics can be expressed:

one memory cycle	= 30 pair delays
one memory access	= 15 pair delays
overhead time	= 15 pair delays
hardware addition	= 10 pair delays
hardware multiply	= $10n$ pair delays
hardware divide	= $20n$ pair delays
software addition	= 60 pair delays
software multiply	= $60 + 10\ (n-1)$ pair delays
software division	= $60 + 20\ (n-1)$ pair delays

Tables I and II illustrate the results of Appendix III by giving argument reduction time and polynomial evaluation time when these are evaluated totally via software, and also by giving polynomial evaluation time when this function is performed in hardware. Percent speed improvement resulting from specialized polynomial evaluation hardware is given by

$$100 \left\{ 1 - \left[\frac{(\text{Argument Reduction Time}) + (\text{Hardware Polynomial Evaluation Time})}{(\text{Argument Reduction Time}) + (\text{Software Polynomial Evaluation Time})} \right] \right\}.$$

The results indicate that little more than a 10% performance improvement can be expected by attempting to enhance the polynomial evaluation method.

In contrast, the digit-by-digit method approaches one software

multiply time plus one software divide time, or

$$[60 + 10(n-1)] + [60 + 20(n-1)] = 120 + 30(n-1).$$

Thus, the best execution time for the digit-by-digit algorithms would be 570 pair delays for 16-bit words and 1050 pair delays for 32-bit words. Tables I and II indicate that 1510 and 3330 pair delays are required respectively for 16- and 32-bit word all software routines. Thus, digit-by-digit techniques offer a factor of three increase in performance.

Table I—16-Bit Word

Function	Argument Reduction Time	Software Polynomial Time	Hardware Polynomial Time	Percent Improvement
Sine/Cosine	970	540	370	11.1
Exponential	970	540	370	11.1
Square Root	430	540	370	17.5
Arc tangent	1340	270	200	4.3

Table II—32-Bit Word

Function	Argument Reduction Time	Software Polynomial Time	Hardware Polynomial Time	Percent Improvement
Sine/Cosine	1610	1720	1350	11.0
Exponential	860	1720	1350	14.4
Square Root	1500	860	690	7.1
Arc tangent	2300	2150	1680	10.5

Appendix I—Square Root

No way was found to manipulate the square root operation to a form that closely relates to the algorithm of the trigonometric and hyperbolic functions. A slight variation of the standard mechanization of square root, shown in Figure 10, bears a surface resemblance to a nonrestoring division operation. Although square root required normalization, this can be performed when setting the initial conditions. The difficulty arises in finding a recursive method of determining X that is of the form

$$X_{i+1} = X_i \pm 2^{-2i} Z_i \, .$$

As seen in Figure 10,

$$X_{i+1} = Q_i + 2^{-(i+1)} C$$

where C is the constant 0.01 or 0.11. The constant is 0.01 if Z_{i+1} is positive and 0.11 if Z_{i+1} is negative. The functional flow diagram for square root is shown in Figure 11.

```
          Z(i+1)  2(Z(i) ± X(i))       X(i+1) = Q(i) + 2^-(i+1) C

 i              Z                          X                   C

          0.000110111001
                       ↙2              0.000000
          0.0110111001                +0.01
 0       -0.010000                     0.010000
          0.0010111001                                       0.10
                       ↙               0.100000
          0.0101110010                +0.001
 1       -0.101000                     0.101000
          1.1011110010                                       0.10
                       ↙               0.100000
          1.0111100100                +0.0011
 2       +0.101100                     0.101100
          0.0010100100                                       0.101
                       ↙               0.101000
          0.0101001000                +0.00001
 3       -0.101010                     0.101010
          1.1010101000                                       0.101
                       ↙               0.101000
          1.0101010000                +0.000011
 4       +0.101011                     0.101011
          0.0000000000                                       0.1010
                                                                  ↘1
                                                             0.010101
```

Fig. 10—Square root.

Appendix II—Natural Logarithms

A form of the natural logarithm can be generated from the hyperbolic functions as shown in the body of this paper. However, the general method of evaluating the trigonometric and hyperbolic functions can be used directly to form the natural logarithm.

The general form for the evaluation of a logarithm, like the other functions, consists of a division-like process followed by a multiplication-like process. Depending on the constant string used (K_i), one can generate either the common or natural logarithm. The method consists

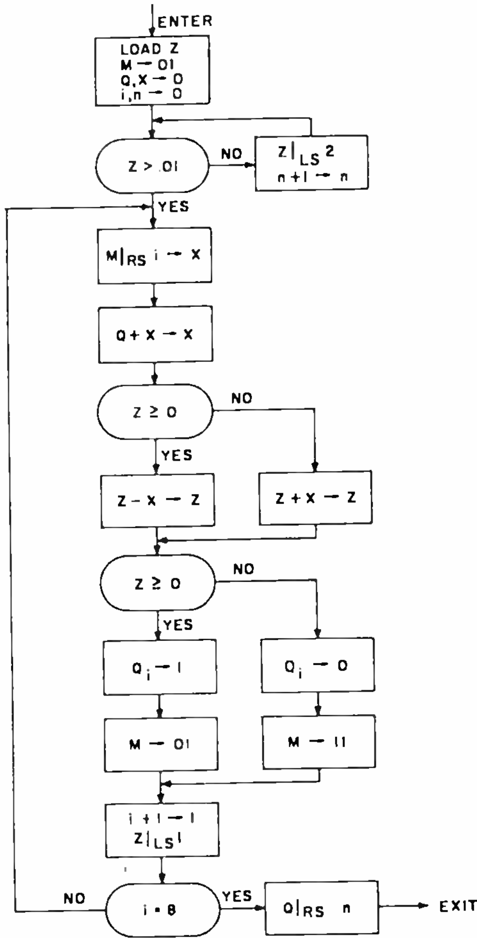

Fig. 11—Flow diagram—square root.

of determining the Q bits so that

$$Y + X = X \left[\prod_{i=0}^{n} (1 + 2^{-i})^{q_i} \right]$$

where X and Y are n-bit positive numbers. The calculation is made to resemble the division process of previous methods.

The calculation of the q_i bits is accomplished by minimizing the magnitude of the expression

$$Y - X\left[\prod_{i=0}^{n}(1+2^{-i})^{q_i} - 1\right] \qquad (18)$$

by choosing successive values of q^i of either +1 or −1. If after $k-1$ steps Expression (18) is negative, we choose $q_k = -1$; if the expression is positive, we choose $q_k = +1$. Again, with the substitution $Z_i = 2^i Y_i$, the following recurrence relations can be derived:

$$Z_{i+1} = 2(Z_i \mp K_i)$$

$$X_{i+1} = X_i \pm 2^{-2i} Z_i$$

Next, the multiplication-like process evaluates the logarithm from a standard set of constants as follows:

$$\ln\left[1 + \frac{Y}{X}\right] = \sum_{i=0}^{n} q_i \ln\,(1+2^{-i})\,.$$

If we set $X = W$ and $Y = 1 - W$,

$$-\ln W = \ln\,(1 + Y/X) = \ln\left(1 + \frac{1-W}{W}\right)$$

$$= \sum_{i=0}^{n} q_i \ln\,(1 - 2^{-i}).$$

In the evaluation of the logarithm, the initial value of Z is the binary value of $(1 - W)$ and the initial value of X is the binary value of W for Part 1 of the process. In Part 2, the initial value of Z is zero and the constant string used is $\ln\,(1 + 2^{-i})$, which is added or subtracted from Z depending on the value of q_i determined in Part 1. The final value of Z is the binary value of $-\ln W$. Figures 12 and 13 give an example of the process for $n = 9$. For this example:

$$-\ln W = \ln\left[1 + \frac{(1-W)}{W}\right]$$

$$\ln\,(1.25) = \ln\,(1 + .25) = \ln\left[1 + \frac{(1-0.8)}{0.8}\right]$$

$z_{i+1} = 1\,(z_i \mp x_i) \qquad x_{i+1} = x_i \pm 2^{-2i}\, z_i$

i	Z	X	Q_{LS}
	00.00110011	00.11001100	
0	-00.11001100	+00.00110011	+1
	11.01100111	00.11111111	
	10.11001110	00.11111111	
1	+00.11111111	-11.10110011	-1
	11.11001101	01.01001100	
	11.10011010	01.01001100	
2	+01.01001100	-11.11111001	-1
	00.11100110	01.01010011	
	01.11001100	01.01010011	
3	-01.01010011	+00.00000111	+1
	00.01111001	01.01011010	
	00.11110010	01.01011010	
4	-01.01011010	+00.00000000	+1
	11.10011000	01.01011010	
	11.00110000	01.01011010	
5	+01.01011010	-11.11111111	-1
	00.10001010	01.01011011	
	01.00010100	01.01011011	
6	-01.01011011	+00.00000000	+1
	11.10111001	01.01011011	
	11.01110010	01.01011011	
7	+01.01011011	-11.11111111	-1
	00.11001101	01.01011100	
	01.10011010	01.01011100	
8	-01.01011100	+00.00000000	-1
	00.00111110	01.01011100	
	00.01111100	01.01011100	
9	-01.01011100	+00.00000000	+1
	11.00100000	01.01011100	

Fig. 12—ln $(1 + (Y/X))$—Part 1.

$\ln (1.25) = (0.2231)_{10} = (0.001110010)_2$ actual

$\ln (1.25) = (0.2246)_{10} = (0.001110011)_2$ calculated

It should be possible to evaluate the exponential function by following the same procedure as for the previous functions. The main idea is to run the logarithm process in reverse using the same constants as in the sine-cosine and arctangent procedures.

For $0 \leq p \leq 1$ we can express e^p as;

$$e^p = \prod_{i=0}^{n} (1 + 2^{-i})^{q_i}$$

where

$$p = \sum_{i=0}^{n} q_i \ln (1 + 2^{-i}).$$

If p is negative, it is possible to make an expansion of p in terms of $\ln (1 - 2^{-i})$. The calculation can then be split into two steps. In the

$$z_{i+1} = z_i + q_i \ln (1 + 2^{-i})$$

i	z	q
	0.000000000	+1 -1 -1 +1 +1 -1 +1 -1 +1 +1
9	+0.000000001	
	0.000000001	
8	+0.000000010	+1 -1 -1 +1 +1 -1 +1 -1 +1
	0.000000011	
7	-0.000000100	+1 -1 -1 +1 +1 -1 +1 -1
	1.111111111	
6	+0.000001000	+1 -1 -1 +1 +1 -1 +1
	0.000000111	
5	-0.000010000	+1 -1 -1 +1 +1 -1
	1.111110111	
4	+0.000011111	+1 -1 -1 +1 +1
	0.000010110	
3	+0.000111100	+1 -1 -1 +1
	0.001010010	
2	-0.001110010	+1 -1 -1
	1.111100000	
1	-0.011001111	+1 -1
	1.100010001	
0	+0.101100010	+1
	0.001110011	

Fig. 13—ln(1 + (Y/X))—Part 2.

first, the q_i bits are determined by a division-like process; and in the second, the exponential is evaluated by a multiplication-like process. As before, use of nonrestoring binary division produces q_i's of +1 and −1 (represented by binary "1" and binary "0", respectively). The procedure works well for Part 1, but a recursive relation for Part 2 that will resemble multiplication is not obvious. The best one we developed introduces a significant error when the iteration index approaches zero. This can be shown as follows. Assume we have just calculated

the ith step and wish to go to the $i+1$ step, where

$$Z_i = \prod_{j=0}^{i} (1 + 2^{-j})^{q_j}.$$

Then

$$Z_{i+1} = [1 + 2^{-(i+1)}]^{q_{i+1}} Z_i .$$

The value of q_{i+1} can be either +1 or −1. When $q_{i+1} = +1$,

$$Z_{i+1} = Z_i + 2^{-(i+1)} Z_i \; ;$$

when $q_{i+1} = -1$,

$$Z_{i+1} = \frac{Z_i - 2^{-(i+1)} Z_i}{1 + 2^{-2(i+1)}} .$$

We see that the recursive relationships introduce an error every time $q_{i+1} = -1$. For $i \gg 0$, this error becomes negligible; but for small values of i (most significant contributions), the error is appreciable, amounting to 25% for the contribution of $i = 0$.

Appendix III—Polynomial Evaluation Methods

Polynomials

A polynomial approximation has the form

$$a_n x^n + a_{n-1} x^{n-1} + \ldots + a_1 x + a_0$$

and will approximate a transcendental function over a finite range of the argument, x. A polynomial can be rewritten in a more convenient format,

$$(\ldots([(a_n)x + a_{n-1}]x + a_{n-2})x + \ldots a_1)x + a_0$$

which illustrates that polynomials can be evaluated by a continuum of multiply–add operations (n such operation pairs for an nth degree polynomial).

To minimize running time with polynomial approximation techniques, tradeoffs are made between the degree of the series (evaluation

time) and argument range reduction. In the case of square root, the argument is classified into one of several subranges; the polynomial degree requirement for each of these subregions is significantly less than a polynomial required to converge to the same accuracy over the entire argument range. Time savings incurred in evaluating a lower-order polynomial more than offset the extra time lost in argument range reduction. With trigonometric transcendental functions, trigonometric identities are employed to reduce the argument into a smaller range. For example, the arctangent routine used on the RCA 601 computer reduces the angular argument into the range of 0° to +15° before calling in a polynomial approximation.

In this appendix, execution time for the various transcendental functions are expressed in terms of the number of additions required versus the number of bits in the binary arithmetic word. As the number of bits are increased, the degree of the polynomial has to increase in order to maintain the same degree of tolerance. Fortuitously, rational function fitting programs in a single and double precision had been developed by Roger L. Crane of RCA Laboratories at the time of this study. Crane's routines were used to determine the degree of a polynomial series required to maintain the same tolerance as the word lengths were increased.

Double precision transcendental function routines, also developed by Crane, were used to obtain the exact values against which to measure polynomial accuracy. The argument reduction methods employed in this analysis are based upon work by John L. O'Neil of RCA Laboratories in developing the elementary function evaluation subroutines for the RCA 601 computer.

Square Root

The most generally accepted machine method of obtaining square root is implementation of Newton's iteration formula

$$x_{n+1} = x_n - \frac{f(x_n)}{f'(x_n)},$$

where, for the square root, $f(x) = x^2 - A$. Thus, the iteration formula becomes $x_{n+1} = 1/2[x_n + (A/x_n)]$.

A polynomial approximation will generate the initial guess. As O'Neil points out, Newton's iteration formula exhibits quadratic con-

vergence; asymptotically, the number of significant figures doubles with each iteration. Therefore, a polynomial need not calculate this initial guess to full word accuracy; at the cost of one division time plus one add time, the accuracy of this initial guess, can be doubled.

A fractional argument was considered over the range $(1/65) \leq x \leq 1$. The lower argument bound cannot be zero; square root exhibits infinite slope at the origin, making reasonable polynomial fits impossible. An argument less than (1/64) requires an even number of left shifts to bring it into range. This even number of left shifts is divided by two, and that many right shifts are applied to the calculated square root answer, returning this answer to proper range.

Table III—Maximum Error of Polynomials in Fitting the Four Subranges of Square Root Algorithm. The Ratio of Errors Between Two Adjacent Ranges for a Polynomial of Degree n is $8^{1/4}$

Polynomial Degree	Maximum Error			
	Range #1	Range #2	Range #3	Range #4
1	2.71×10^{-3}	4.55×10^{-3}	7.66×10^{-3}	1.29×10^{-2}
2	3.46×10^{-4}	5.82×10^{-4}	9.79×10^{-4}	1.65×10^{-3}
3	5.52×10^{-5}	9.29×10^{-5}	1.56×10^{-4}	2.63×10^{-4}
4	9.86×10^{-6}	1.66×10^{-5}	2.79×10^{-5}	4.69×10^{-5}
5	1.89×10^{-6}	3.17×10^{-6}	5.34×10^{-6}	8.97×10^{-6}

Four logarithmically equal argument subregions were chosen; therefore the percentage error produced by each of the four polynomials in calculating the initial guess is nearly a constant. The maximum error that polynomials of degrees one through five will produce in each of these four subregions is tabulated in Table III. This table indicates, for example, that a fifth-degree polynomial will have a maximum error of 1.89×10^{-6} in range 1, or an error of 2 in the sixth-least-significant decimal position. The analysis determined that *only* a second- or third-degree polynomial approximation followed by Newton's iterations will yield the fastest execution time. All other approaches using higher order polynomials require a longer execution time.

These results are shown in Figure 14; square root execution time is plotted in terms of the number of full word arithmetic additions versus the number of bits in this binary arithmetic word. As shown

in Figure 14, the third-order polynomial for a first guess is superior to the quadratic approach only in a few limited ranges of arithmetic word length. Each sharp upward shift in the two curves corresponds

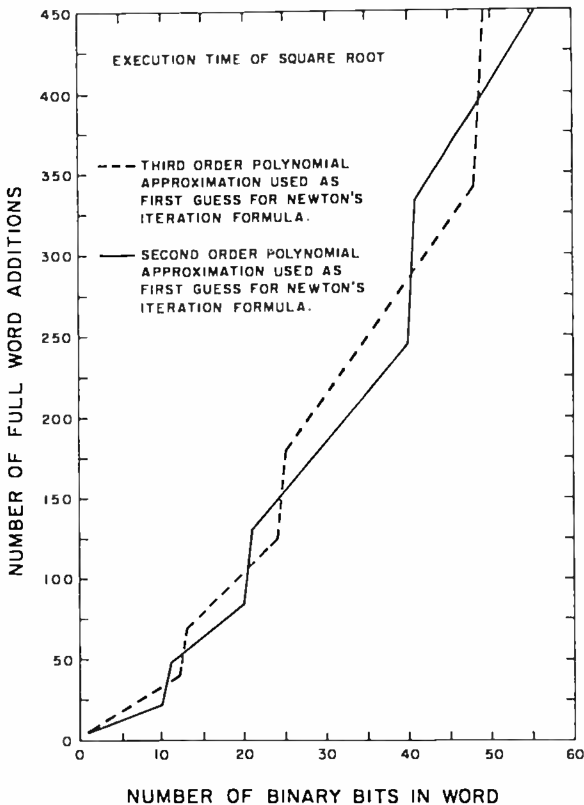

Fig. 14—Number of additions versus size of binary word (square root).

to another application of Newton's iteration formula. With floating-point binary numbers, shifting operations will yield the proper exponent in the square root; and an argument right shift along with proper exponent correction prior to square root execution will handle odd exponents.

Arctangent

The concept in arctangent evaluation is to balance the time component of argument reduction against the time component of polynomial evaluation. A choice for argument range for direct polynomial

evaluation is limited. Trigonometric identities allow reduction of any angle into an equivalent principle angle of $\tan^{-1}|x| = 0°$ to $\tan^{-1}|x| = 45°$. The crucial identity is $\tan^{-1}|x| = 90° - \tan^{-1}(1/|x|)$ when $\tan^{-1}|x| > 45°$ Polynomial approximation over this full range results in excessive execution time. First $0° \leqq \tan^{-1}|x| < 45°$ is subdivided into two ranges:

$$(1) \quad 0° \leqq \tan^{-1}|x| < 15° ,$$

$$(2) \quad 15° \leqq \tan^{-1}|x| < 45° .$$

Then a transformation is used on argument x in Range 2 such that this transformed argument z is $-15° < \tan^{-1}z < +15°$. The trigonometric identity permitting this transformation is

$$\tan^{-1}x = \mp \tan^{-1}c + \tan^{-1} \frac{x \pm c}{1 \mp xc}$$

where c is an appropriate constant. In this case, $c = 2 - \sqrt{3}$, or $\tan^{-1}c = 15°$. If the time cost of this argument reduction now matches the time cost of polynomial evaluation, we probably have a minimum execution time. If polynomial evaluation is still excessive, further transformations to reduce the polynomial's argument range to $0° \leqq \tan^{-1}|x| < 7\frac{1}{2}°$ can be applied.

For the machine characteristics considered, only one transformation is required for arithmetic words up to 30 bits in size (see Figure 15). Beyond this word size, as shown in Figure 15, the degree requirement on the polynomial climbs rapidly. Another transformation costing one divide time plus two add times may be offset by the time savings due to a reduction in polynomial degree requirement. Alternatively, substitution of continued fraction for a polynomial approximation may prove fruitful in yielding an overall minimum execution time.

Execution time versus arithmetic word length is plotted in Figure 15 for binary floating-point numbers (the value of $\tan^{-1}|x|$ can exceed 45°). For fractional binary number representation only, the value of $\tan^{-1}|x|$ is always less than 45° and "time cost of argument reduction" as shown in Figure 15 is one divide time ($2n$) too large.

Table IV—Maximum Error of Polynomials in Fitting the Argument Range 0.0 to $(2 - \sqrt{3})$ for the Arctangent Algorithm

Polynomial Degree	Maximum Error (0 to $\tan^{-1}x = 15°$)
1	1.52×10^{-3}
3	1.58×10^{-5}
5	1.97×10^{-7}
9	7.0×10^{-9}

Table IV lists the maximum error of the polynomial approximation to arctangent as a function of polynomial degree. Choice of odd polynomials simplifies handling of negative arguments $f(-x) = -f(x)$ for odd functions.

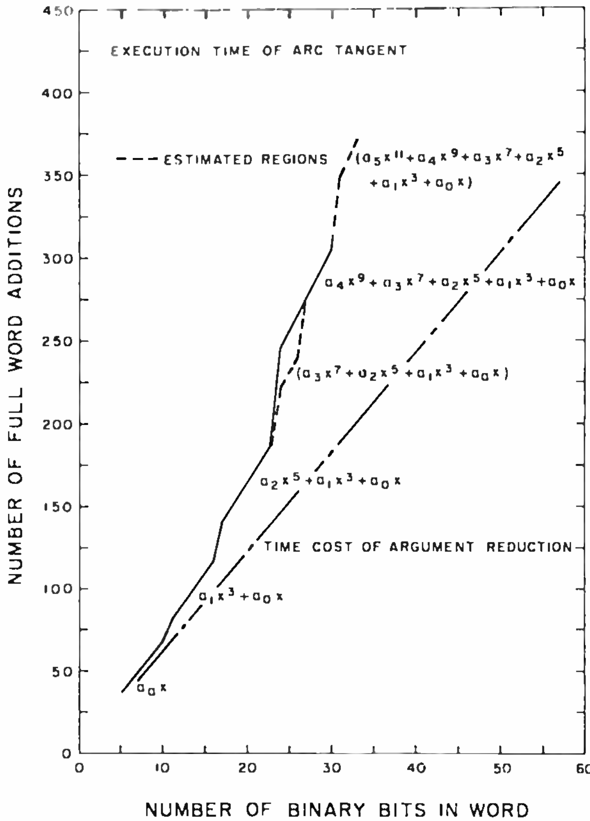

Fig. 15—Number of additions versus size of binary word (arc tangent).

Exponential

The function e^x is formed from 2^x by $e^x = 2^{x \log_2 e}$. Again, the concept is to compromise polynomial evaluation time versus argument reduction time. Consider arguments less than unity*: $0 \leq x < 1$. A polynomial asked to converge over this entire range will have an exceptionally high degree, about an eleventh degree for a 30-bit arithmetic word.

Instead we could subdivide this argument range into several smaller intervals and compute 2^x using the value of x to select the appropriate polynomial. Two argument subranges require polynomials of degree seven or eight each (for 30 binary bit arithmetic word). Eight argument subranges require four-degree polynomials for each range. An increase in argument subranges to eight doubles the "constant" storage requirements to 32 words but almost halves execution time.

At the expense of about one additional multiply time, substantial reductions in "constant" storage requirements can be achieved. The approach is to employ the additive property of exponents. Thus, let the original argument x equal the sum of two numbers such that

$$2^x = 2^{x_1} \times 2^{x_2} \tag{19}$$

Choose x_1 to be, say the four leading (or most significant) bits of argument x; then x_2 is all remaining bits of lesser significance. These two subarguments have the range

$$\begin{aligned} 1/16 &\leq x_1 < 1 \\ 0 &\leq x_2 < 1/16 \end{aligned} \tag{20}$$

The factor 2^{x_1} can be obtained from a stored table of powers of two in 1/16 increments. This table contains 15 words and is addressed by the four bits of x_1. The factor 2^{x_2} is approximated by a polynomial. One additional multiply time is then expended to form 2^x according to Equation (19).

Figure 16 illustrates the execution time of this approach for both a 4-bit x_1 (solid line) and a 3-bit x_1 (dashed line). The maximum errors generated by the polynomials used to approximate 2^{x_2} are shown in Table V.

O'Neil showed how relative accuracy can be increased without a significant increase in execution time. His approach is to make the

* For arguments greater than unity, the bits to the left of the radix point become the exponent of the result.

Table V—Maximum Error of Polynomials in Approximating 2^x in the range 0 to +1/16, 0 to +1/8, −1/32 to 0, and −1/16 to 0

Polynomial Degree	Maximum Error Range 0 to +1/16	Range 0 to +1/8	Range −1/32 to 0	Range −1/16 to 0
1	1.2×10^{-4}	4.9×10^{-4}	2.9×10^{-5}	1.1×10^{-4}
2	4.3×10^{-7}	3.5×10^{-6}	5.2×10^{-8}	4.1×10^{-7}
3	1.2×10^{-9}	1.0×10^{-8}	7.1×10^{-11}	1.1×10^{-9}
4	2.5×10^{-12}	8.3×10^{-11}	7.7×10^{-14}	2.4×10^{-12}
5	4.6×10^{-15}	3.0×10^{-13}	6.9×10^{-17}	4.4×10^{-15}

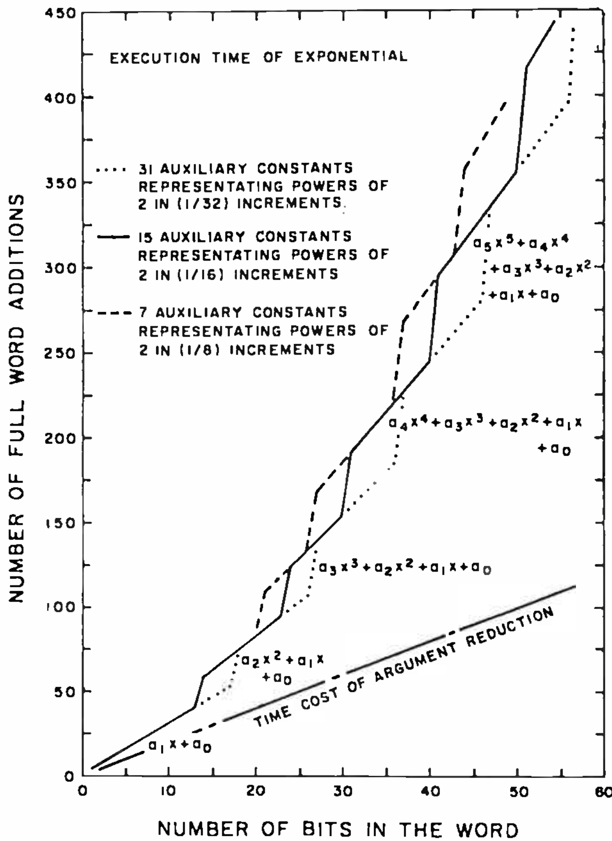

Fig. 16—Number of additions versus size of binary word (exponential).

following transformation on the subarguments x_1 and x_2. We shall illustrate this approach with a four-bit x_1.

$$2^x = 2^{x_1} \times 2^{x_2}$$
$$= 2^{(x_1+1/16)} \times 2^{(x_2-1/16)}$$

One sixteenth is now added to x_1 before the stored table of the powers of two is addressed. We now have

$$-\frac{1}{16} \leq \left[x_2 - \frac{1}{16} \right] < 0 . \tag{21}$$

While x_2 had five leading zeros including the one to the left of the radix point, the number $x_2 - (1/16)$ has five leading ones. On an absolute percentage basis, a polynomial approximating the range Equation (21) will have slightly less error than a polynomial approximately the range Equation (20) ; compare the maximum errors tabulated in Table V.

In some cases, execution time can be further reduced by one addition time. The approach is to halve the range of $x_2 - (1/16)$ and later restore the range by squaring the output of the polynomial approximation. That is,

$$2^x = 2^{x_1+(1/16)} (2^{(1/2)(x_2-1/16)})^2$$

and

$$-\frac{1}{32} \leq \frac{1}{2} \left[x_2 - \frac{1}{16} \right] < 0$$

is the new argument range for the polynomial approximation.

Halving of the convergence range for some word lengths reduces the polynomial's degree requirement by one, a saving of $(n+1)$ additions. But, range restoration costs one multiply time, a net reduction of execution time by one addition time. As O'Neil points out, this last step should be made only after a transformation of subarguments x_1 and x_2. Accuracy is lost in squaring, but this transformation of subarguments somewhat compensates. Figure 17 plots execution time of O'Neil's approach versus word length for two sizes of stored constants.

Sine and Cosine

Trigonometric identities are used to transform an argument x in the range

$$0 \leq x < 2\pi \tag{22}$$

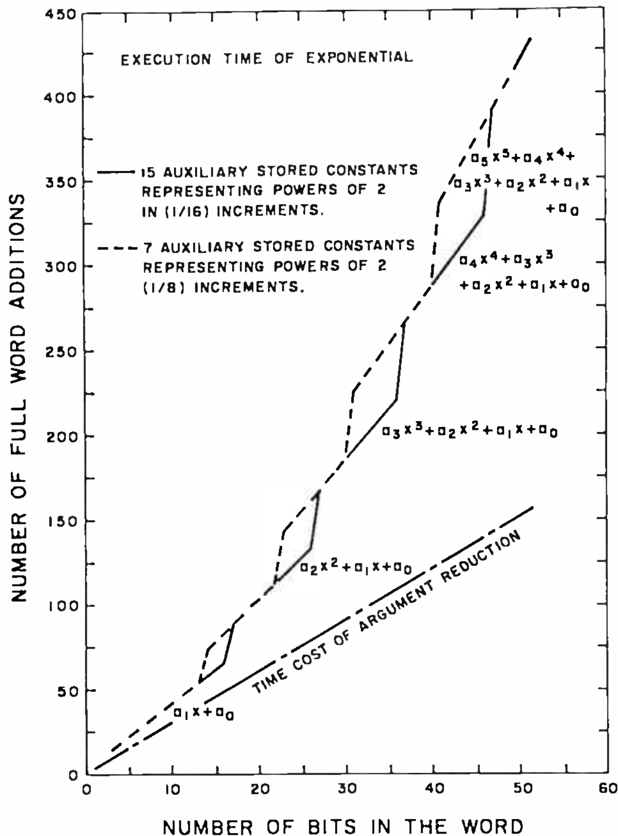

Fig. 17—Number of additions versus size of binary word (exponential).

into the range

$$0 \leq z < \frac{\pi}{4} \tag{23}$$

An argument outside the range of Equation (22) is first divided by

2π and then stripped of all bits to the left of the radix point; these bits represent the largest integer number of times that 2π divides the argument.

Trigonometric identies employed in range reduction of Equation (22) to Equation (23) involve both sine and cosine functions. Poly-

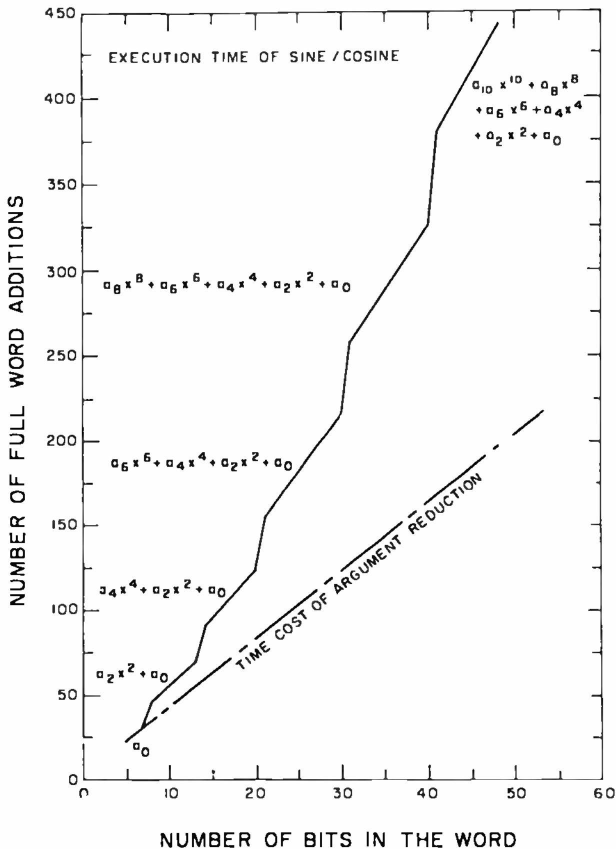

Fig. 18—Number of additions versus size of binary word (exponential).

nomials approximate both the functions $\cos z$ and $[\sin z]/z$ over the range of Equation (23); the function $[\sin z]/z$ is chosen for approximation rather than $\sin z$, as O'Neil points out, to preserve full significance of $\sin z$ near $z = 0$. Table VI illustrates the maximum error of even degree polynomials approximating $\cos z$ and $[\sin z]/z$ in the range of 0 to $\pi/4$. Execution time for sine or cosine evaluation is shown in Figure 18.

Table VI—Maximum Error for Even Polynomials Approximating cos x and $[\sin x]/x$ in the Argument Range 0 to $(\pi/4)$ Radians

Polynomial Degree	Maximum Error, Range $0 \leq x < \pi/4$	
	$\cos(x)$	$\sin(x)/x$
0	1.5×10^{-1}	5.0×10^{-2}
2	1.9×10^{-3}	3.9×10^{-4}
4	1.0×10^{-5}	1.4×10^{-6}
6	2.8×10^{-8}	3.0×10^{-9}
8	4.7×10^{-11}	4.3×10^{-12}
10	5.5×10^{-14}	4.3×10^{-15}
12	4.7×10^{-17}	3.1×10^{-18}
14	3.0×10^{-20}	

Summary-Polynomial Approximations

Polynomial approximation approaches described apparently yield a minimum execution time for word lengths up to 32 bits. Beyond 32, other alternatives such as continued fraction expansions should be explored.

Transcendental function evaluation is divisible into two categories—argument reduction and polynomial evaluation. Procedures for argument reduction are unique to each transcendental function. A polynomial evaluation is the only common denominator. Argument reduction is summarized for 16- and 32-bit words in Table VII. The number of arithmetic operations as well as the time cost equation are included.

Odd polynomials, such as

$$a_7x^7 + a_5x^5 + a_3x^3 + a_1x \tag{24}$$

are evaluated by first forming $z = x^2$ and then evaluating $y = \{[(a_7)z$

Table VII—Argument Reduction Arithmetic for 16- and 32-Bit Words

Function	Type of Polynomial	Number of Operations		Time Cost Equation	
		16 bits	32 bits	16 bits	32 bits
Sine/Cosine	Even	6	6	$4n + 3$	$4n + 3$
Exponential	All	4	4	$2n + 2$	$2n + 2$
Square Root	All	2	4	$2n + 1$	$4n + 2$
Arctangent	Odd	7	7	$6n + 3$	$6n + 3$

Table VIII—Execution Times in Terms of Number of Additions for 16-Bit Words

Function	Effective Degree	Constants		Polynomial Evaluation Time	Argument Reduction Time
		Poly.	Aux.		
Sine/Cosine	2	3	9	34	67
Exponential	2	3	7	34	34
Square Root	2	3	4	34	33
Arc tangent	1	2	6	17	99

$+ a_5]z + a_3\}z + a_1$, followed by another multiply operation to form xy. Thus, two multiply operations are "charged" against argument reduction arithmetic. The "effective degree" of polynomial, such as Equation (24) is defined as *three*. Even polynomial evaluation is treated by a similar time cost accounting procedure. Execution times in terms of number of additions for 16- and 32-bit words are summarized in Tables VIII and IX.

Table IX—Execution Time in Terms of Number of Additions for 32-Bit Words

Function	Effective Degree	Constants		Polynomial Evaluation Time	Argument Reduction Time
		Poly.	Aux.		
Sine/Cosine	4	5	9	132	131
Exponential	4	5	7	132	66
Square Root	2	3	4	66	130
Arc tangent	5	6	6	165	195

TRANSMISSION AND REFLECTION GROUP DELAY OF BUTTERWORTH, CHEBYCHEV, AND ELLIPTIC FILTERS

BY

C. M. KUDSIA AND N. K. M. CHITRE*

RCA Victor Company, Ltd.
Montreal, Canada

Summary—Transmission group delay of low-pass prototype filters is compared with the reflection group delay of high-pass prototype filters for Butterworth, Chebychev, and elliptic responses. The criterion chosen for comparison is a minimum value of isolation in the stop band, a maximum value of return loss in the pass band, and identical number of sections. Group delays are computed from the pole-zero configuration of transfer functions. Normalized tables of group delay for inverse Chebychev and elliptic function filters are provided to aid filter design.

INTRODUCTION

THE PRESENT-DAY, high-performance wide-band communication systems such as satellite communications require optimum performance from filtering networks. Any filtering network introduces a certain amount of distortion of information owing to the variation of group delay with frequency in its pass band. This variation also causes a variation in the insertion loss of the network, which also causes distortion. This study compares the group delays of filter networks with Butterworth, Chebychev, and elliptic responses for a given design objective and discusses the optimum performance available from any filtering network. These functions were chosen because they are the most popular ones and because they are the optimum functions for different design criteria.

The design of filters using these functions on an insertion-loss

---

* N. K. M. Chitre is presently with COMSAT.

basis (or magnitude function) is well established.[1-3] The insertion phase and group-delay characteristics of Butterworth and Chebychev filters were studied by Orchard[4] and Schreiber[5] who, respectively, gave the explicit expressions for group delay and published normalized tables. This paper extends this approach to the determination of phase and group delay of 'inverse Chebychev' and elliptic filters in transmission and discusses the reflection group delay of high-pass filters for the same design performance as that of low-pass filters in transmission. Normalized tables of group delay of inverse Chebychev and elliptic filters for $N = 2$ to 11 are provided to aid in filter design.

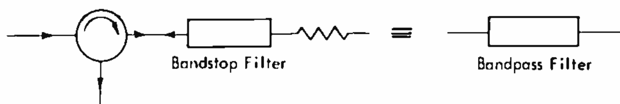

Fig. 1—Alternative band-pass arrangement.

Reflection Group Delay—Minimum Phase Networks

Any network whose transfer function has all its poles and zeros in the left half complex plane is said to be, by definition, a 'minimum phase' network, since such networks exhibit minimum phase shift. Such network functions can be uniquely determined[6,7] if either the magnitude function or the phase response is specified. In other words, if two minimum phase networks have identical magnitude response, their phase, and hence group delay, must also be identical.

Since the Butterworth, Chebychev, and elliptic functions are all minimum phase functions (no zeroes in the right half plane), any two arrangements of these filters having identical magnitude response must also have identical group delays. Figure 1 shows alternative

[1] R. Saal and E. Ulbrich, "On the Design of Filters by Synthesis," *IRE Trans. on Circuit Theory*, Dec. 1958.

[2] G. L. Matthaei, Leo Young, and E. M. T. Jones, *Microwave Filters, Impedance Matching Networks and Coupling Structures*, New York, McGrawHill Book Co., Inc., 1964.

[3] N. K. M. Chitre and M. V. O'Donovan, "A Unified Design Chart for Small VSWR Filters," *The Microwave Journal*, April 1967.

[4] H. J. Orchard, "The Phase and Envelope Delay of Butterworth and Tchebycheff Filters," *IEEE Trans. on Circuit Theory*, Vol. CT-7, p 180, June 1960.

[5] Heinz H. Schreiber, "Phase and Time Delay of Butterworth and Chebychev Filters," *Microwaves*, March 1965.

[6] E. A. Guillemin, *Synthesis of Passive Networks*, John Wiley & Sons 1957.

[7] Louis Weinberg, *Network Analysis and Synthesis*, McGraw Hill Book Company, Inc., 1962.

band-pass arrangements. Let us consider the three cases when the band-stop filter has Butterworth, Chebychev, or elliptic response.

(1) ***Butterworth Response*** (See Figure 2)

The nth order Butterworth response is given by

$$|Z_{12}(j\omega)|^2 = \frac{1}{1+\omega^{2n}} \tag{1}$$

where $Z_{12}(j\omega)$ is the transfer impedance of the filter with ω as the

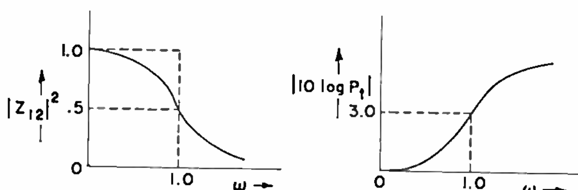

Fig. 2—Low-pass prototype response of a Butterworth filter.

frequency variable. In terms of the insertion loss function, the power transmitted through the filter per unit incident power is

$$P_t = \frac{1}{1+\omega^{2n}} \tag{2}$$

For doubly terminated filters, however, with unity generator and load resistors,

$$\frac{P_L}{P_{max}} = |t(j\omega)|^2 = |Z_{12}(j\omega)|^2, \tag{3}$$

where P_L is the power delivered to the load, P_{max} is the maximum available power from the source, and $t(j\omega)$ is the transmission coefficient of the filter. Therefore, if $P_{max} = 1$,

$$P_L = P_t = |t(j\omega)|^2 = |Z_{12}(j\omega)|^2 = \frac{1}{1+\omega^{2n}} \tag{4}$$

Equation (4) gives the low-pass prototype Butterworth response. To derive the high-pass response, we use the frequency transformation $\omega \rightarrow \omega^{-1}$,

$$P_{tHP} = \frac{1}{1 + \omega^{-2n}} = \frac{\omega^{2n}}{1 + \omega^{2n}}. \tag{5}$$

The reflected power is given by

$$P_{rHP} = 1 - P_{tHP} = 1 - \frac{\omega^{2n}}{1 + \omega^{2n}} = \frac{1}{1 + \omega^{2n}}, \tag{6}$$

which is identical to the low-pass response. In other words, the transmission response of the low-pass prototype filter is identical to the high-pass prototype filter in reflection provided the 3-dB bandwidth is the same in both cases. Consequently, the phase response and group delay in both cases would be identical.

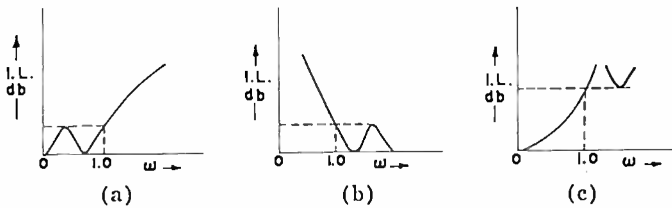

Fig. 3—Response of Chebychev filters: (a) low-pass prototype in transmission, (b) high-pass prototype in transmission, and (c) high-pass prototype in reflection.

(2a) Chebychev Response (See Figure 3)

The nth order Chebychev response is given by

$$|Z_{12}(j\omega)|^2 = \frac{1}{1 + \epsilon^2 T_n{}^2(\omega)} \tag{7}$$

where ϵ is the ripple factor in the pass band and $T_n(\omega)$ is the Chebychev polynominal of order n and first kind.

In terms of the insertion loss function,

$$P_t = \frac{1}{1 + \epsilon^2 T_n{}^2(\omega)} \tag{8}$$

which is the low-pass prototype response. The transmission response of the high-pass filter with the same cutoff value is

$$P_{tHP} = \frac{1}{1 + \epsilon^2 T_n^2(\omega^{-1})} \tag{9}$$

and reflected power is

$$P_{rHP} = 1 - P_{tHP} = \frac{\epsilon^2 T_n^2(\omega^{-1})}{1 + \epsilon^2 T_n^2(\omega^{-1})} = \frac{1}{1 + \epsilon^{-2} T_n^{-2}(\omega^{-1})} \tag{10}$$

This response is different from the low-pass prototype transmission response and hence its group delay would be different. This group delay is determined next and is compared with the group delay of other types of responses.

(2b) *Inverse Chebychev Response*

The nth order inverse Chebychev response is given by[7]

$$|Z_{12}(j\omega)|^2 = \frac{\epsilon^2 T_n^2(\omega^{-1})}{1 + \epsilon^2 T_n^2(\omega^{-1})}, \tag{11}$$

which is the same as the reflection response of a high-pass Chebychev filter (Equation (10)).

The transfer function may be expressed as

$$|Z_{12}(j\omega)|^2 = \frac{1}{1 + \epsilon^{-2} T_n^{-2}(\omega^{-1})}. \tag{12}$$

The poles of this function (see Figure 4) in the complex S plane are given by the roots of

$$1 + \epsilon^{-2} T_n^{-2}\left(-\frac{1}{js}\right) = 0$$

$$T_n\left(-\frac{1}{js}\right) = \pm \frac{j}{\epsilon} \tag{13}$$

where s is the complex frequency variable $\sigma + j\omega$. Equation (13) yields (see Appendix) the following roots

$$s_\nu = \sigma_\nu + j\omega_\nu, \quad \nu = 1, 2, 3, \ldots 2n$$

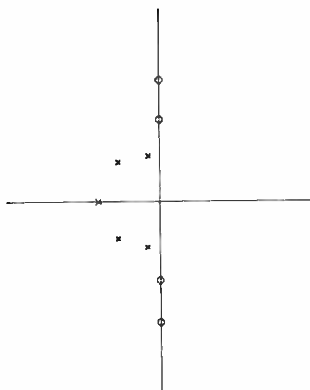

Fig. 4—Pole-zero configuration of an inverse Chebychev filter.

where

$$\sigma_\nu = \frac{\sinh\left(\frac{1}{n}\sinh^{-1}\frac{1}{\epsilon}\right)\sin\frac{(2\nu-1)\pi}{2n}}{D}$$

$$\omega_\nu = \frac{\cosh\left(\frac{1}{n}\sinh^{-1}\frac{1}{\epsilon}\right)\cos\frac{(2\nu-1)\pi}{2n}}{D} \tag{14}$$

$$D = \left[\sinh\left(\frac{1}{n}\sinh^{-1}\frac{1}{\epsilon}\right)\sin\frac{(2\nu-1)\pi}{2n}\right]^2 + \left[\cosh\left(\frac{1}{n}\sinh^{-1}\frac{1}{\epsilon}\right)\cos\frac{(2\nu-1)\pi}{2n}\right]^2$$

The left half plane roots are given by

$$\sigma_\nu = - \frac{\sinh\left(\frac{1}{n}\sinh^{-1}\frac{1}{\epsilon}\right)\sin\frac{(2\nu-1)\pi}{2n}}{D}$$

$$\omega_\nu = - \frac{\cosh\left(\frac{1}{n}\sinh^{-1}\frac{1}{\epsilon}\right)\cos\frac{(2\nu-1)\pi}{2n}}{D} \tag{15}$$

$$\nu = 1, 2, \ldots n$$

Hence the complete transfer function in the all-pole configuration can be written

$$Z_{12}(s) = \frac{K_o}{\prod_{\nu=1}^{n} (s - s_\nu)}$$

where K_o is an arbitrary constant and

$$s_\nu = \sigma_\nu + j\omega_\nu, \quad \nu = 1, 2, \ldots n.$$

The phase angle θ follows from the transfer function,

$$\theta = - \sum_{\nu=1}^{n} \tan^{-1} \frac{\omega - \omega_\nu}{\sigma_\nu} \tag{16}$$

and group delay is

$$\tau = - \frac{d\theta}{d\omega} = \sum_{\nu=1}^{n} \frac{|\sigma_\nu|}{\sigma_\nu^2 + (\omega - \omega_\nu)^2} \tag{17}$$

Thus phase and group delay of the inverse Chebychev function can be computed at any frequency. A sample output is shown in Figure 5.*

* Normalized tables of group delay for $n = 3$ to 12 with minimum attenuations of 20, 26, 30, 34 and 40 dB in the stop band may be obtained from the authors on request.

GROUP DELAY OF INVERSE CHEBYCHEV FILTERS

NUMBER OF SECTIONS = 5

TIME DELAY IN SECONDS

ω rad./sec.	A DB MIN. 20.0	26.0	30.0	34.0	40.0
0.00	0.2055053E 01	0.2607558E 01	0.3002275E 01	0.3422303E 01	0.4107876E 01
0.05	0.2061189E 01	0.2615961E 01	0.3012561E 01	0.3434879E 01	0.4124928E 01
0.10	0.2079827E 01	0.2641522E 01	0.3043891E 01	0.3473244E 01	0.4177119E 01
0.15	0.2111689E 01	0.2685342E 01	0.3097748E 01	0.3539426E 01	0.4267799E 01
0.20	0.2158053E 01	0.2749415E 01	0.3176845E 01	0.3637190E 01	0.4403405E 01
0.25	0.2220924E 01	0.2836909E 01	0.3285579E 01	0.3772797E 01	0.4595194E 01
0.30	0.2303272E 01	0.2952668E 01	0.3430860E 01	0.3956411E 01	0.4862540E 01
0.35	0.2409484E 01	0.3104103E 01	0.3623587E 01	0.4204625E 01	0.5238529E 01
0.40	0.2546093E 01	0.3302705E 01	0.3881145E 01	0.4544536E 01	0.5776989E 01
0.45	0.2723039E 01	0.3566588E 01	0.4231401E 01	0.5019261E 01	0.6552319E 01
0.50	0.2955821E 01	0.3924565E 01	0.4717922E 01	0.5690680E 01	0.7613570E 01
0.55	0.3269162E 01	0.4421630E 01	0.5402321E 01	0.6619300E 01	0.8798975E 01
0.60	0.3702942E 01	0.5122126E 01	0.6344043E 01	0.7760994E 01	0.9470434E 01
0.65	0.4320134E 01	0.6091446E 01	0.7499206E 01	0.8733997E 01	0.8955764E 01
0.70	0.5209166E 01	0.7296044E 01	0.8493950E 01	0.8838400E 01	0.7577614E 01
0.75	0.6441300E 01	0.8364451E 01	0.8640491E 01	0.7897030E 01	0.6130121E 01
0.80	0.7870315E 01	0.8574764E 01	0.7752182E 01	0.6544668E 01	0.4971464E 01
0.85	0.8794562E 01	0.7705346E 01	0.6443614E 01	0.5330693E 01	0.4112122E 01
0.90	0.8413043E 01	0.6393349E 01	0.5260912E 01	0.4397134E 01	0.3475530E 01
0.95	0.7082054E 01	0.5212072E 01	0.4350632E 01	0.3703323E 01	0.2992648E 01
1.00	0.5699374E 01	0.4311363E 01	0.3675149E 01	0.3181383E 01	0.2615764E 01
1.05	0.4635320E 01	0.3649123E 01	0.3167894E 01	0.2778190E 01	0.2313791E 01
1.10	0.3877655E 01	0.3155219E 01	0.2776351E 01	0.2457904E 01	0.2066418E 01
1.15	0.3334329E 01	0.2775452E 01	0.2465143E 01	0.2197099E 01	0.1860067E 01
1.20	0.2930169E 01	0.2473874E 01	0.2211259E 01	0.1980317E 01	0.1685379E 01

Fig. 5—Sample output showing group delay of inverse Chebychev filters.

(3) Elliptic Response

The nth order elliptic function filter has the response[1]

$$|Z_{12}(j\omega)|^2 = \frac{1}{1+\epsilon^2 K_n^2(\omega)}, \tag{18}$$

where, for n odd and $m = (n-1)/2$,

$$K_n(\omega) = \frac{F(\omega)}{P(\omega)} = \frac{\omega(a_2^2-\omega^2)(a_4^2-\omega^2)\ldots(a_m^2-\omega^2)}{(1-a_2^2\omega^2)(1-a_4^2\omega^2)\ldots(1-a_m^2\omega^2)};$$

for n even and $m = n/2$,

$$K_n(\omega) = \frac{F(\omega)}{P(\omega)} = \frac{(a_2^2 - \omega^2)(a_4^2 - \omega^2)\ldots(a_m^2 - \omega^2)}{(1 - a_2^2\omega^2)(1 - a_4^2\omega^2)\ldots(1 - a_m^2\omega^2)} \quad (19)$$

The poles of this function $K_n(\omega)$ are the reciprocals of its zeros, i.e.,

$$K_n\left(\frac{1}{\omega}\right) = \frac{1}{K_n(\omega)}.$$

This implies that the value of $K_n(\omega)$ at any frequency ω_1, in the range $0 \leqslant \omega \leqslant 1$ is the reciprocal of its value at the reciprocal frequency $1/\omega_1$ in the range $1 \leqslant \omega \leqslant \infty$. Consequently, if $K_n(\omega)$ has equal ripples in the pass band, it will automatically have equal ripples in the stop band. The function that yields the critical frequencies $a_1, a_2 \ldots$ etc., such that $K_n(\omega)$ has equal ripple character in the range $0 < \omega < 1$ is the Jacobian elliptic function snU_ν, where U_ν is a new variable given by

$$U_\nu(k,\phi) = \int_0^{\phi_\nu} \frac{d\xi}{\sqrt{1 - k^2 \sin^2 \xi}}, \quad \nu = 1,2 \ldots n-1 \quad (20)$$

Equation (20) is the elliptic integral of the first kind of modulus $k = \sin\theta$. The critical frequencies are given by

$$a_\nu = snU_\nu, \quad \nu = 1, 2, \ldots n-1$$

$$a_n = \sqrt{k} = \sqrt{\sin\theta}$$

If K is the complete elliptic integral of the first kind, i.e.,

$$K = \int_0^{\pi/2} \frac{d\xi}{\sqrt{1 - k^2 \sin^2 \xi}},$$

then it can easily be shown that

$$U_\nu = \frac{\nu}{n} K, \quad \nu = 1, 2, \ldots n-1, \quad (21)$$

and

$$a_\nu = sn\left(\frac{\nu}{n}K\right)$$

$$a_n = \sqrt{\sin\theta}$$

The value of θ determines the sharpness of cutoff and is expressed by

$$\sin\theta = \frac{\Omega_c'}{\Omega_s'}.$$

It should be emphasized here that the normalization is based on the geometrical mean of the pass-band and stop-band limits instead of the usual pass-band limit (cutoff frequency). Such normalization in the case of elliptic functions yields a symmetrical form.

The maximum deviation or amplitude of $K_n(\omega)$ about zero in the pass band is

$$\Delta = \frac{1}{a_n}\prod_{\nu=1}^{m+1} a_{2\nu-1}^2, \quad \text{for } n \text{ odd, } m = (n-1)/2$$

$$= \prod_{\nu=1}^{m} a_{2\nu-1}^2, \quad \text{for } n \text{ even, } m = n/2 \tag{22}$$

Therefore, in the range $1 < \omega < \infty$, the minimum value of $K_n(\omega)$ would be $1/\Delta$, as we have shown previously that $K_n(1/\omega) = 1/K_n(\omega)$. The ripple factor ϵ can easily be shown to be related to the reflection coefficient ρ and to Δ by

$$\epsilon = \frac{1}{\Delta\sqrt{\rho^{-2}-1}} \tag{23}$$

For a given n, θ and ρ, the values of a_ν and ϵ can be computed and, hence, the elliptic function (magnitude squared)

$$|Z_{12}(j\omega)|^2 = \frac{1}{1+\epsilon^2 K_n^2(\omega)}$$

is completely determined. In terms of the insertion loss function, the elliptic response would be

$$P_t = \frac{1}{1 + \epsilon^2 K_n^2(\omega)}. \tag{24}$$

This is the low-pass prototype response (see Figure 6). The high-pass response is

$$P_{tHP} = \frac{1}{1 + \epsilon_1^2 K_n^2(\omega^{-1})}, \tag{25}$$

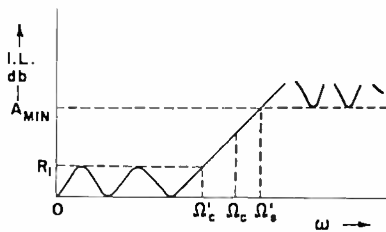

Fig. 6—Low-pass prototype response of an elliptic filter.

where ϵ_1 is a new ripple factor. The response in reflection of this high-pass filter would be

$$P_{rHP} = 1 - P_{tHP} = \frac{1}{1 + \dfrac{1}{\epsilon_1^2 K_n^2(1/\omega)}} = \frac{1}{1 + \dfrac{K_n^2(\omega)}{\epsilon_1^2}}, \tag{26}$$

since $K_n(1/\omega) = 1/K_n(\omega)$ for the elliptic function. This response would be identical to the low-pass prototype transmission response if

$$\epsilon^2 = 1/\epsilon_1^2, \tag{27}$$

that is, if

$$\frac{1}{\Delta^2(\rho^{-2} - 1)} = \Delta^2(\rho_1^{-2} - 1).$$

Here we have assumed that the Δ's are identical, i.e., n and θ are the

same in both cases. Thus,

$$-20 \log \rho_1 = 10 \log \left[1 + \frac{1}{\Delta^4(\rho^{-2} - 1)} \right], \tag{28}$$

i.e., the return loss in the pass band of the high-pass filter in dB equals the minimum attenuation in the stop band of the low-pass filter in dB. In other words, for a given n and θ, the transmission magnitude response of a low-pass prototype elliptic filter is identical to the reflection response of a high-pass elliptic filter, provided the return loss in the pass band of the high-pass filter is equal to the minimum attenuation in the stop band of the low-pass filter. Consequently, the group delays of two such arrangements would be identical.

To determine the complete elliptic low-pass prototype transfer functions, we must determine the poles of $|Z_{12}(j\omega)|^2$, or the roots of

$$1 + \epsilon^2 K_n^2(\omega) = 0,$$

$$1 + \epsilon^2 \frac{F^2(\omega)}{P^2(\omega)} = 0. \tag{29}$$

For $s = j\omega$ and by analytic continuation, we have

$$1 + \epsilon^2 K_n(s) K_n(-s) = 0$$

or

$$P(s)P(-s) + \epsilon^2 F(s)F(-s) = 0. \tag{30}$$

For the case where n is odd, $F(s)$ is an odd polynominal and therefore

$$[P(s) + \epsilon F(s)][P(s) - \epsilon F(s)] = 0. \tag{31}$$

It is easily seen the the roots of $P(s) + \epsilon F(s) = 0$ are the mirror images of the roots of $P(s) - \epsilon F(s) = 0$. Therefore, to solve Equation (30), it is sufficient to determine the roots of $P(s) + \epsilon F(s) = 0$. However, for the case where n is even, both $F(s)$ and $P(s)$ are even polynominals and Equation (30) becomes

$$P^2(s) + \epsilon^2 F^2(s) = 0. \tag{32}$$

The roots of (32) determine all the poles in the s-plane. In either case, the poles of the elliptic function filter can be represented by

$$s_\nu = \pm\,\sigma_\nu \pm j\omega_\nu, \quad \nu = 1, 2, \ldots n. \tag{33}$$

The left half plane poles would be

$$s_\nu = -\,\sigma_\nu \pm j\omega_\nu, \quad \nu = 1, 2 \ldots n. \tag{34}$$

The pole–zero configuration of a typical case is depicted in Figure 7.

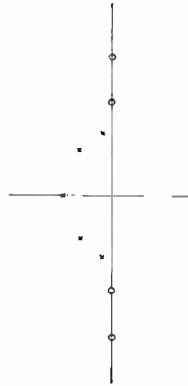

Fig. 7—Pole-zero configuration of an elliptic filter.

The zeros are given by $P(s) = 0$ and lie symmetrically on the $j\omega$ axis. In the all-pole configuration, the complete transfer function is

$$Z_{12}(s) = \frac{H_o}{\prod_{\nu=1}^{n} (s - s_\nu)}, \tag{35}$$

where H_o is an arbitrary constant and s_ν represents the left-half-plane poles given by Equation (34). The phase angle θ is then

$$\theta = -\sum_{\nu=1}^{n} \tan^{-1} \frac{\omega - \omega_\nu}{\sigma_\nu} \tag{36}$$

and the group delay is

$$\tau = -\frac{d\theta}{d\omega} = \sum_{\nu=1}^{n} \frac{|\sigma_\nu|}{\sigma_\nu^2 + (\omega - \omega_\nu)^2}. \tag{37}$$

GROUP DELAY OF LOWPASS PROTOTYPE ELLIPTIC FILTERS

NUMBER OF SECTIONS = 5

REFLECTION COEFFICIENT = 0.0500

TIME DELAY IN SECONDS

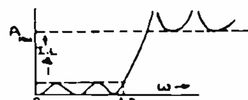

ω RAD/SEC	θ° / A MIN DB	55.00 / 20.0	49.00 / 26.0	45.00 / 30.2	41.00 / 34.7	36.00 / 40.8
0.00	•	0.1625783E 01 •	0.1880616E 01 •	0.2034553E 01 •	0.2175665E 01 •	0.2333970E 01
0.05	•	0.1628377E 01 •	0.1883238E 01 •	0.2037114E 01 •	0.2178113E 01 •	0.2336221E 01
0.10	•	0.1636262E 01 •	0.1891220E 01 •	0.2044921E 01 •	0.2185568E 01 •	0.2343115E 01
0.15	•	0.1649750E 01 •	0.1904909E 01 •	0.2058340E 01 •	0.2198475E 01 •	0.2355064E 01
0.20	•	0.1669375E 01 •	0.1924879E 01 •	0.2077968E 01 •	0.2217399E 01 •	0.2372719E 01
0.25	•	0.1695893E 01 •	0.1951927E 01 •	0.2104626E 01 •	0.2243189E 01 •	0.2396926E 01
0.30	•	0.1730304E 01 •	0.1987076E 01 •	0.2139325E 01 •	0.2276846E 01 •	0.2428664E 01
0.35	•	0.1773875E 01 •	0.2031557E 01 •	0.2183252E 01 •	0.2319498E 01 •	0.2466979E 01
0.40	•	0.1828176E 01 •	0.2086823E 01 •	0.2237745E 01 •	0.2372348E 01 •	0.2518909E 01
0.45	•	0.1895120E 01 •	0.2154544E 01 •	0.2304265E 01 •	0.2436643E 01 •	0.2579428E 01
0.50	•	0.1977053E 01 •	0.2236636E 01 •	0.2384405E 01 •	0.2513651E 01 •	0.2651422E 01
0.55	•	0.2076858E 01 •	0.2335324E 01 •	0.2479930E 01 •	0.2604692E 01 •	0.2735729E 01
0.60	•	0.2198189E 01 •	0.2453304E 01 •	0.2592916E 01 •	0.2711293E 01 •	0.2833398E 01
0.65	•	0.2345865E 01 •	0.2594084E 01 •	0.2726094E 01 •	0.2835543E 01 •	0.2945627E 01
0.70	•	0.2526715E 01 •	0.2762724E 01 •	0.2883580E 01 •	0.2980813E 01 •	0.3075400E 01
0.75	•	0.2751324E 01 •	0.2967393E 01 •	0.3072312E 01 •	0.3153111E 01 •	0.3227826E 01
0.80	•	0.3037848E 01 •	0.3222457E 01 •	0.3304752E 01 •	0.3363433E 01 •	0.3412556E 01
0.85	•	0.3420570E 01 •	0.3554674E 01 •	0.3603822E 01 •	0.3631666E 01 •	0.3646577E 01
0.90	•	0.3969741E 01 •	0.4015336E 01 •	0.4011543E 01 •	0.3992681E 01 •	0.3958011E 01
0.95	•	0.4838619E 01 •	0.4703098E 01 •	0.4602831E 01 •	0.4504420E 01 •	0.4390359E 01
1.00	•	0.6368243E 01 •	0.5797812E 01 •	0.5499673E 01 •	0.5252136E 01 •	0.5000150E 01
1.05	•	0.9181502E 01 •	0.7543637E 01 •	0.6840861E 01 •	0.6317461E 01 •	0.5830907E 01
1.10	•	0.1295529E 02 •	0.9800415E 01 •	0.8520756E 01 •	0.7614845E 01 •	0.6813865E 01
1.15	•	0.1281694E 02 •	0.1084242E 02 •	0.9578134E 01 •	0.8557364E 01 •	0.7594417E 01
1.20	•	0.8910248E 01 •	0.9203760E 01 •	0.8835242E 01 •	0.8299410E 01 •	0.7618500E 01

Fig. 8—Sample output showing group delay of low-pass prototype elliptic filters.

The group delay, therefore, can be computed at any frequency.* A sample output is shown in Figure 8.

Comparison of Transmission and Reflection Group Delays of Butterworth, Chebychev, and Elliptic Filters

Figures 9(a) and 9(b) show the transmission group delay and insertion loss response respectively of the low-pass prototype filters; Figures 10(a) and 10(b) depict the corresponding reflection response

* Normalized tables of group delay for $n = 3$ to 11 and reflection coefficients of 1, 2, 5, 10 and 50% are available from the authors on request.

of the high-pass prototype filters. Figure 11 depicts the group delays on an expanded frequency scale. Since any filtering network is distinguished by the amount of distortion it introduces owing to its imperfect pass band and the minimum isolation it can provide at a desired frequency outside the pass band, the criteria chosen for the comparison of group delays are a minimum value of isolation at and beyond a fixed frequency outside the pass band, a maximum value of return loss (or VSWR) in the pass band, and an identical number of sections.

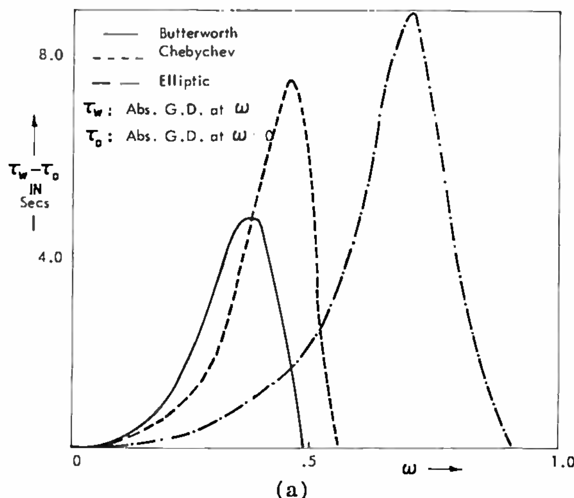

(a)

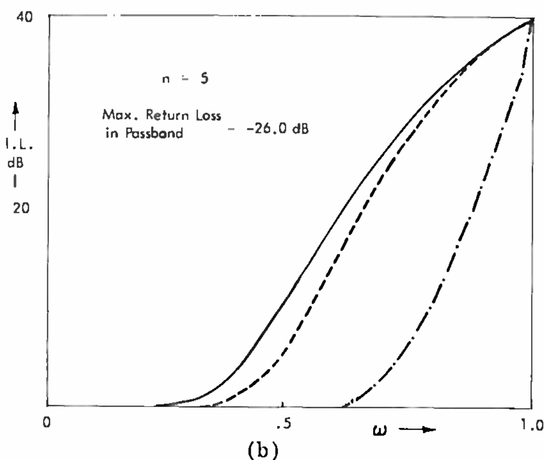

(b)

Fig. 9—(a) Normalized relative transmission group delay of low-pass prototype filters and (b) insertion loss response of low-pass prototype filters.

As discussed in the previous section, the transmission characteristics of low-pass prototypes would be identical to those of reflection characteristics of high-pass prototypes for Butterworth and elliptic responses under these conditions.

In the case of Chebychev filters, however, an improvement in the group delay is effected by utilizing the reflection response of the high-pass Chebychev filter (same as transmission response of inverse Chebychev). This improvement is effected at the expense of the monotonic increase in attenuation beyond the fixed isolation frequency

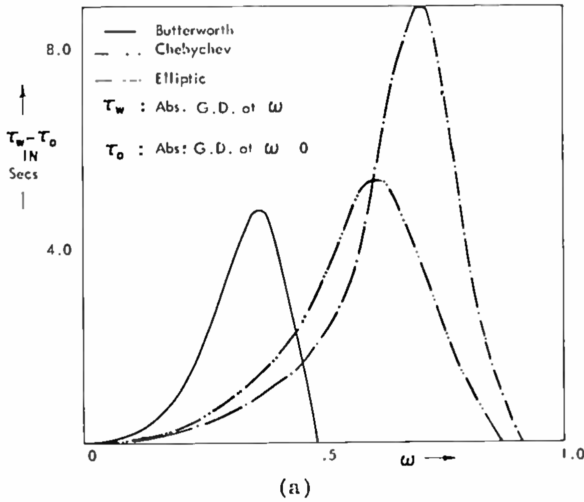

(a)

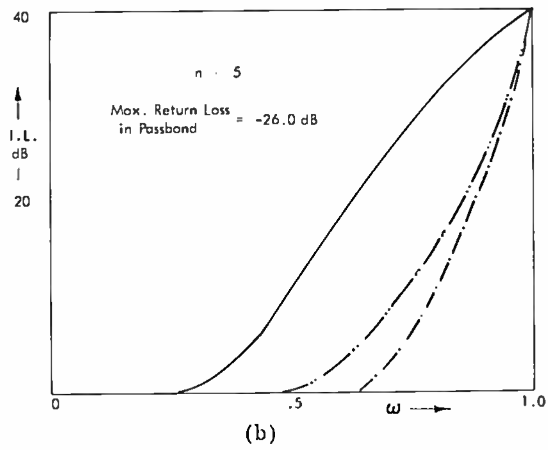

(b)

Fig. 10—(a) Normalized relative reflection group delay of high-pass prototype filters and (b) reflected magnitude response of high-pass prototype.

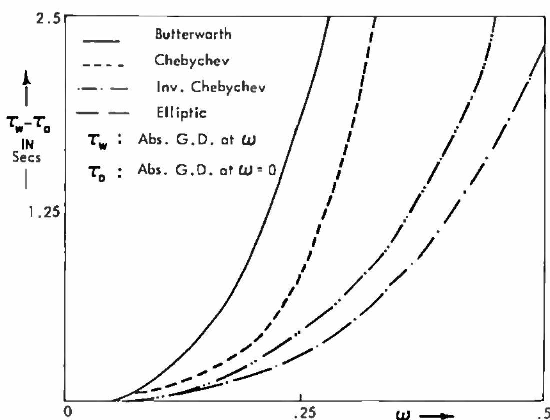

Fig. 11—Normalized relative group delays on an expanded frequency scale.

(Figure 12) of the low-pass prototype filter. It can be seen, then, that for the inverse Chebychev filter, there is an improvement in the pass band both with respect to the group delay and to the return loss.

Comparing the group delays of different filters in Figures 9-11, we see that, for a given design, the elliptic filter gives the best group delay followed by inverse Chebychev, Chebychev, and Butterworth, in that order. Also, if approximately the same Q_0 (unloaded Q) can be realized in each of the above configurations, then the elliptic filter would yield the best pass-band flatness characteristics, followed by inverse Chebychev, Chebychev, and maximally flat filters. Realization of these filters in different frequency ranges, however, imposes limitations.

At low frequencies (below 300 MHz), any of the above filter configurations can be realized in a lumped circuit with little difficulty, but realization of elliptic filters above 300 MHz (especially at microwave frequencies) is more difficult; however, wide-band (≥ 30%) elliptic

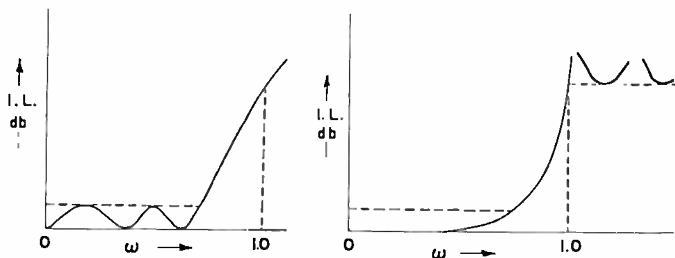

Fig. 12—Comparison of Chebychev and inverse Chebychev prototype filters.

band-pass filters have been realized.[8] Levy and Whitley[9] describe elliptic band-stop filters in coupled structures with smaller bandwidths. A circulator–band-stop elliptic filter could be an attractive arrangement provided a Q_u, of the order of 1000 (comparable to band-pass Chebychev interdigital filters), can be obtained. Otherwise, a trade-off will exist between loss and group delay.

The design of Butterworth and Chebychev filters is well established from low frequencies to well into the microwave region for a very wide range of bandwidths. Consequently, a circulator–band-stop Chebychev filter arrangement is worth consideration compared to a simple Chebychev band-pass filter. In the former case, group delay and pass-band flatness would be better, although the absolute insertion loss could be greater owing to the contribution of nearly constant loss of the circulator. The minimum isolation required in the stop band may, however, impose a practical limitation on the design of Chebychev band-stop filters. The design of an inverse Chebychev filter, which would yield the same performance as circulator–band-stop Chebychev filter design, is worthy of consideration.

It may be emphasized here that the elliptic function gives optimum performance. Papoulis[10] has shown that an elliptic response has the smallest possible 'cutoff-interval' $\omega_c - 1$ for a given variation in the pass band (0, 1) and stop band (ω_c, ∞). This implies that equal ripple property exists both in the pass band and stop band for optimum filters. Further, if monotonic increase in attenuation is desired, Papoulis[10] has shown that the Chebychev function yields the highest rate of cutoff for a given variation in the pass band. Consequently, for a given n, a maximum value of return loss in the pass band, and a minimum value of attenuation in the stop band at a specified frequency, Chebychev and elliptic functions yield optimum performance. The inverse relationship between group delay and cutoff frequency implies that group-delay characteristics available from Chebychev, inverse Chebychev, and elliptic functions are also optimum characteristics, i.e., no other function can give better group-delay characteristics for the design criterion as stated above. This also implies that, for a given average Q_u (unloaded Q of resonators), these functions will also give the optimum pass-band

[8] M. C. Horton and R. J. Wenzel, "The Digital Elliptic Filter—A Compact Sharp-Cutoff Design for Wide Bandstop or Bandpass Requirements", *IEEE Trans. on Microwave Theory and Techniques*, Vol. MTT-15, No. 5, p 307, May 1967.

[9] R. Levy and I. Whitley, "Synthesis of Distributed Elliptic Function Filters from Lumped Constant Prototype," *IEEE Trans. on Microwave Theory and Techniques*, Vol. MTT-14, p 506, Nov. 1966.

[10] A. Papoulis, "On the Approximation in Filter Design", *1957 IRE National Convention Record*, pt. 2, pp 175-185.

flatness characteristic. However, if, in the physical realization of these functions, the value of average Q_o is different for different functions, then a trade-off will exist between group delay and pass band flatness.

CONCLUSIONS

The design of filters on the basis of magnitude function tends to ignore the associated phase function. However, for the design criterion of a minimum value of isolation at a fixed frequency in the stop band and a maximum value of return loss in the pass band, the elliptic function yields the optimum group—delay and pass-band flatness characteristic for a given number of sections. If monotonic increase in attenuation is desired beyond the fixed isolation frequency, the Chebychev function yields optimum characteristics. Further, it has been shown in this paper that under the design criterion stated above, the low-pass prototype transmission response is identical to the high-pass prototype reflection response for the cases of Butterworth and elliptic filters. This relationship is particularly useful for realizing band-pass elliptic responses for bandwidths $< 30\%$. Levy and Whitley[9] have shown that band-stop elliptic filters can be realized in coupled structures with bandwidths from 0.1% to nearly 100%. Such filters when used in reflection-type arrangements would yield elliptic band-pass responses. It may be mentioned here that Horton and Wenzel[8] have indicated that it is extremely difficult to realize a band-pass filter (in transmission) for bandwidths $\leqslant 30\%$.

The reflection response of Chebychev band-stop filters is not identical to the transmission response of Chebychev band-pass filters. However, if the monotonic increase in attenuation beyond the fixed minimum isolation frequency can be sacrificed, then the reflection response of Chebychev band-stop filters offers the advantage of better group-delay and pass-band flatness characteristics.

ACKNOWLEDGMENTS

The authors are very grateful to P. Pfeiffer who carried out all the computations on an RCA Spectra 70 computer. Thanks are extended to RCA Victor Company, Ltd., for their generous support of this work and for their kind permission to publish this paper.

APPENDIX

The poles of the inverse Chebychev function are given by

$$T_n\left(-\frac{1}{js}\right) = \pm\frac{j}{\epsilon}.$$

This represents poles that are the reciprocals of the poles of the Chebychev function, viz,

$$T_n(-js) = \pm \frac{j}{\epsilon}.$$

The poles of the Chebychev function are given by[7]

$$s_\nu = \sinh\left(\frac{1}{n}\sinh^{-1}\frac{1}{\epsilon}\right)\sin\frac{(2\nu-1)\pi}{2n} + j\cosh\left(\frac{1}{n}\sinh^{-1}\frac{1}{\epsilon}\right)\cos\frac{(2\nu-1)\pi}{2n}$$

$$= \sigma_\nu + j\omega_\nu, \quad \nu = 1, 2, 3, \ldots 2n.$$

Therefore, the poles of the inverse Chebychev function would be given by

$$s_\nu' = \frac{1}{\sigma_\nu + j\omega_\nu} = \sigma_\nu' - j\omega_\nu'$$

where

$$\sigma_\nu' = \frac{\sigma_\nu}{\sigma_\nu^2 + \omega_\nu^2}$$

$$\omega_\nu' = \frac{\omega_\nu}{\sigma_\nu^2 + \omega_\nu^2}$$

$$\sigma_\nu = \sinh\left(\frac{1}{n}\sinh^{-1}1/\epsilon\right)\sin\frac{(2\nu-1)\pi}{2n}$$

$$\omega_\nu = \cosh\left(\frac{1}{n}\sinh^{-1}1/\epsilon\right)\cos\frac{(2\nu-1)\pi}{2n}$$

It is to be noted that for the inverse Chebychev case, there would be zeros on the $j\omega$ axis.

HIGH-FREQUENCY BEHAVIOR OF MICROSTRIP TRANSMISSION LINES*

By

L. S. Napoli and J. J. Hughes

RCA Laboratories
Princeton, N. J.

Summary—The properties of microstrip transmission lines at frequencies from 1 to 18 GHz were measured on alumina substrates. The phase velocity and characteristic impedance deviates from the TEM-like behavior described by Wheeler.[1] The velocity and impedance deviation is shown to be dependent on the frequency and the substrate thickness.

Introduction

Recent advances in microwave integrated circuits have led to widespread use of the microstrip transmission line as a basic building block for microwave integrated circuits. The early analytic work on microstrip lines[1] has been based on a proposed TEM mode of propagation which is, in essence, a static approximation to a dynamic system. Measurements on microstrip transmission lines have been reported by Caulton, Hughes, and Sobol[2] at frequencies up to 4 GHz. The results indicate very good agreement with the low-frequency theoretical results of Wheeler.[1]

The low-frequency analysis is quite good when the wavelength is very much longer than the dielectric thickness. However, as one can see from Figure 1, the microstrip transmission system has electric field lines that cross the dielectric–air interface. The discontinuity in electric field at the interface implies a surface charge. Under dynamic

---

* This work was supported by the United States Army Electronics Command, Fort Monmouth, New Jersey, under Contract No. DAAB07-68-C-0296.

[1] H. A. Wheeler, "Transmission-Line Properties of Parallel Wide Strips by a Conformal-Mapping Approximation," *IEEE Trans. MTT*, Vol. MTT-12, p. 280, May 1964.

[2] M. Caulton, J. J. Hughes, and H. Sobol, "Measurements on the Properties of Microstrip Transmission Lines for Microwave Integrated Circuits," *RCA Review*, Vol. 27, No. 3, p. 377, Sept. 1966.

conditions, the electric and magnetic fields are modified so that both the electric and magnetic fields are discontinuous at the dielectric–air interface. The propagating mode, therefore, is not a pure TEM mode. In fact, there are components of both electric and magnetic fields in the direction of propagation. The dynamic solution for the electric and magnetic fields associated with the microstrip transmission lines is much more difficult than the static solution, since an infinite number

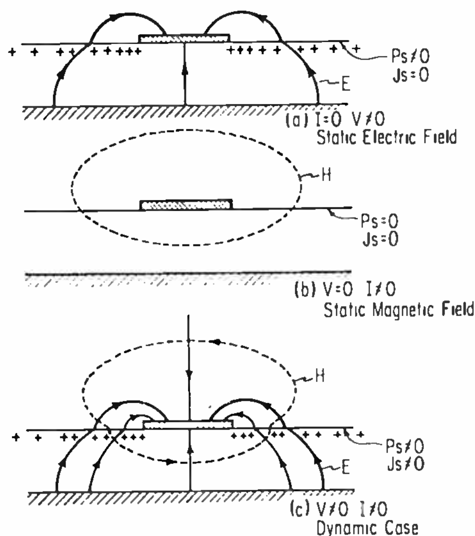

Fig. 1—Electric and magnetic fields in the vicinity of a microstrip transmission line.

of higher-order modes must be considered. At the present time, it is not clear whether the solution for a nonradiating open microstrip line is possible, since some of the higher-order modes may be radiative and therefore not evanescent.

Neither the theoretical model nor the measurements referred to above indicate a frequency dependence of characteristic impedance or phase velocity for microstrip lines. Recently, however, workers[3,4] have reported measurements that show a dispersive nature to microstrip lines.

---

[3] C. P. Hartwig, D. Masse, R. A. Pucel, "Frequency Dependent Behavior of Microstrips," International Microwave Symposium, 1968 G-MTT, Detroit, Michigan.

[4] P. Troughton, "Measurement Techniques in Microstrip," *Electronics Letters*, Vol. 5, No. 2, p. 25, Jan. 23, 1969.

The work reported in this paper is the result of measurements of phase velocity and characteristic impedance at frequencies higher than reported earlier.[2]

Dispersion Measurements

All of the measurements were made on one-inch-long microstrip lines on substrates of polished (to 1×10^{-6} inch) alumina (Alsimag 772, $\epsilon_R = 9.6$).* Two substrate thicknesses were used, 0.050 and 0.025 inch. The line widths were chosen so that the low-frequency characteristic impedance is 50 ohms. Measurements were made in the frequency range 1 to 18 GHz.

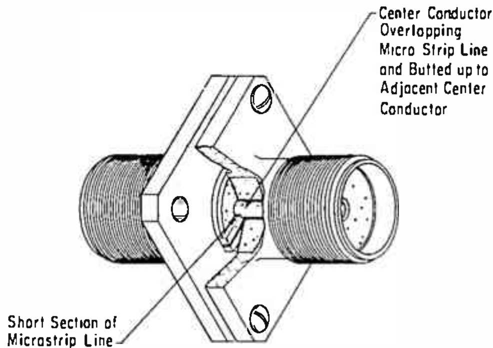

Fig. 2—Coax-microstrip adapter test configuration.

The coax-to-microstrip transition was made from a modified OSM** type flange mount (VSWR = 1.06 up to 12 GHz). Two of these transitions are shown in Figure 2. The transitions are butted against each other, and a 0.025-inch length of substrate is inserted between them to simulate the discontinuity. A very short section is used because the microstrip line has a frequency-dependent impedance that tends to obscure the coaxial-line-microstrip discontinuity at high frequencies.

If the VSWR of the coax-to-microstrip connector is large, it will obscure the small deviations in impedance and phase velocity. VSWR versus frequency of a pair of these connectors is shown in Figure 3(a). These measurements were made on a GR-900 slotted line

---

* Trade name of American Lava for Al_2O_3. Dielectric constant reported on their data sheet measured at 1 MHz.

** Trademark of Omni Spectra.

from 1 GHz to 6 GHz, and on an OSM slotted line up to 18 GHz. A GR-900 load was used to 15 GHz and an OSM load used above 15 GHz.

Phase velocity measurements were made using the transmission test unit of a Hewlett Packard network analyzer. The microstrip line was placed in one leg of the unit and compared to a pair of butted

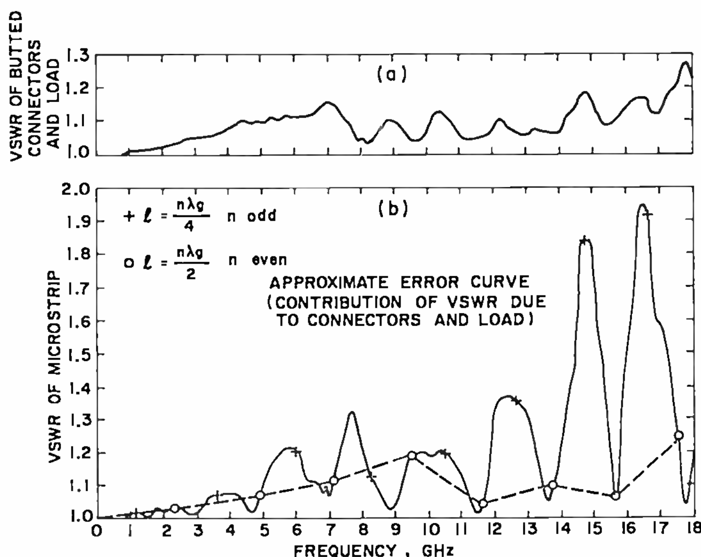

Fig. 3—(a) VSWR of butted microstrip–coax adapters and (b) VSWR of microstrip transmission line.

connectors. An equivalent electrical length of dispersionless line was inserted in the other leg. (This dispersionless line is a line stretcher built into the transmission test unit, Figure 4.)

The array of photographs in Figure 5 shows the relative attenuation and phase shift between the butted connectors plus line stretcher, and the 0.025-inch-thick microstrip line. Notice that the relative loss between the two arms is negligible (less than 0.2 dB), yet the phase difference is quite nonlinear.

The deviation in phase angle between a length, L_M, of microstrip line and a length, L_C, of dispersionless coaxial air line is

$$\Delta\theta^\circ = \frac{360}{2\pi}\,\beta_a\left[L_M - \frac{L_C}{\sqrt{\epsilon_W}} + \frac{\omega^2}{\omega_\beta{}^2}L_M + \ldots\right], \qquad (1)$$

where β_o is the low-frequency wave number of Wheeler,[1] and ω_β is the coefficient of the first nonlinear term. The linear portion $L_M - (L_C/\sqrt{\epsilon_W})$, is made as close to zero as possible, assuming the low-frequency effective dielectric constant, ϵ_W, is known . The linear portion of phase angle shown in the photographs is due to the uncertainty of effective dielectric constant.

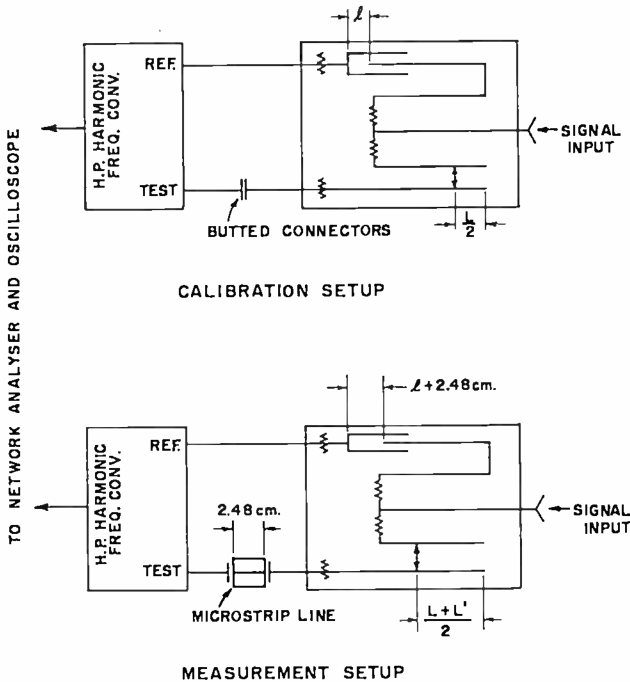

Fig. 4—Microstrip-line dispersion test configuration.

The normalized wave-number deviation from Wheeler's solution is plotted in Figure 6. From Equation (1).

$$\frac{\beta - \beta_o}{\beta_o} = \frac{\omega^2}{\omega_\beta{}^2} + \ldots = \frac{2\pi\Delta\theta}{360\beta_o L_M} \left(1 - \frac{L_C}{L_M\sqrt{\epsilon_W}}\right). \quad (2)$$

The abscissa is the inverse wavelength in the dielectric normalized to dielectric thickness.

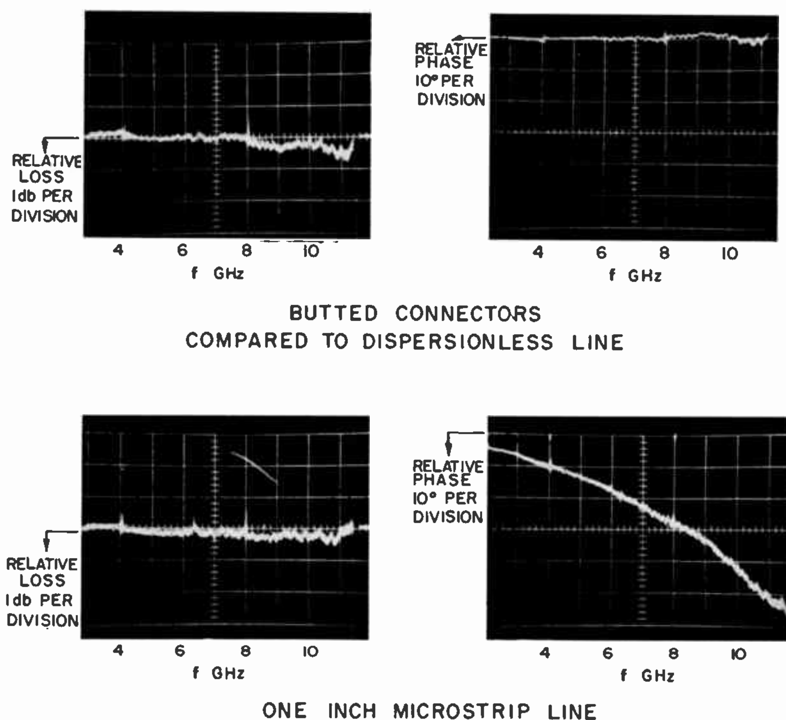

Fig. 5—(a) Difference in phase angle between butted microstrip adapters and dispersionless line; (b) difference in phase angle between microstrip transmission line and dispersionless line.

Impedance Measurements

The characteristic impedance of the microstrip line was deduced from VSWR measurements shown in Figure 3(b). (Figure 3(b) gives the data for the 0.025-inch-thick substrate.) The transmission-line VSWR measurements were made under the same conditions as the connector VSWR measurements, except that the 0.025-inch length of alumina was replaced by a 1.00-inch length of microstrip line.

The OSM connectors overhang the microstrip line by 0.012 inch on each side, and hence, the line length was assumed to be 0.98 inch long.

The low-frequency wave number was assumed to be[2] $\beta_o = k_o/0.399$, where $k_o = 2\pi f\sqrt{\mu\epsilon_o}$. The microstrip line is an integral number of quarter wavelengths when

$$\frac{n\pi}{2} = \frac{2\pi f l}{0.399c}\left[1+\left(\frac{f}{f_\beta}\right)^2\right], \qquad (6)$$

where

$n =$ integer,

$l =$ length of line,

$(\mu\epsilon_o)^{-1/2} = c =$ velocity of light in vacuum,

$f_\beta = 59$ GHz (for the 0.025-inch-thick line).

When n is an even integer, the line is an integral number of half

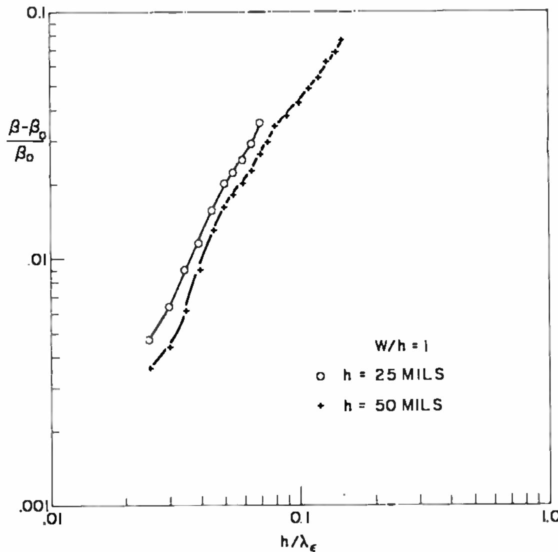

Fig. 6—Normalized wave number deviation as a function of normalized wavelength in dielectric.

wavelengths long and the observed VSWR is that due to the load and connectors. These points are shown as open circles in Figure 3(b). A dashed line is shown connecting these points to arrive at an approximate error due to connector mismatch.

When n is an odd integer, the line is an odd number of quarter wavelengths and the VSWR is due to the combined line mismatch and connector mismatch. These points are shown as crosses in Figure 3(b).

The deviation in characteristic admittance from the low-frequency value of 50 ohms is shown plotted in Figure 7 for both the 0.050- and 0.025-inch substrates. The abscissa is the same as for the previous curve. The straight line drawn through these points is a best fit to the expected square-law behavior of the function.

DISCUSSION

For a transmission line, the normalized wave number, β, and characteristic admittance, y, behave as

$$\frac{\beta}{\beta_o} = \sqrt{\frac{XY}{X_oY_o}}. \tag{3}$$

$$\frac{y}{y_o} = \sqrt{\frac{X_oY}{Y_oX}}, \tag{4}$$

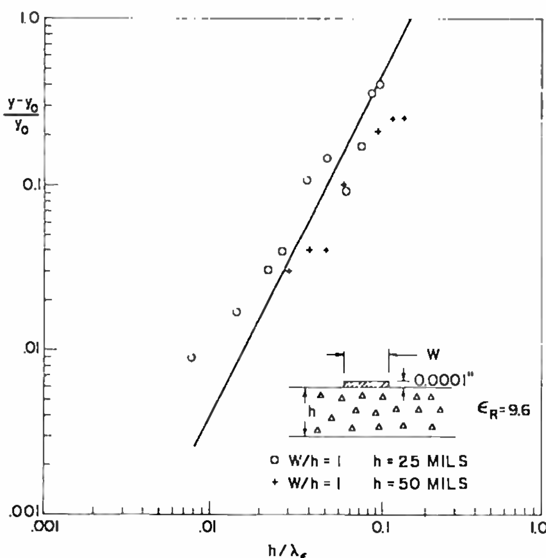

Fig. 7—Normalized characteristic admittance deviation as a function of normalized wavelength in dielectric.

where X and Y are the series reactance and shunt susceptance of the line. The subscript zero denotes the low-frequency limit, or the TEM mode, where

$$X = X_o = \omega L_o \tag{5}$$

$$Y = Y_o = \omega C_o \tag{6}$$

as $\omega \to 0$

The apparent shunt capacitance and series inductance, therefore, are

$$\frac{C}{C_o} = \frac{\beta y}{\beta_o y_o}, \tag{7}$$

$$\frac{L}{L_o} = \frac{y_o}{\beta_o}\frac{\beta}{y}. \tag{8}$$

It is apparent from Figures 6 and 7 that both the wave number and the characteristic admittance are increasing functions of frequency. The capacitance, from Equation (7), is also an increasing function of frequency. Since the characteristic admittance increases with frequency at a greater rate than does the wave number (Figures 6 and 7), the inductance (from Equation 8) decreases with frequency. This implies that the magnetic flux lines do not all encircle the microstrip line, but rather that there is a component of magnetic field in the direction of propagation. At high frequencies, therefore, the fields tend to be confined within the dielectric space. That is, evanescent higher-order modes such as a surface-wave mode on a dielectric-clad metal[5] tend to store more of the energy at higher frequencies.

Conclusions

The microstrip transmission line exhibits measurable dispersion and frequency-dependent admittance. The degree of dispersion and admittance variation is a function of the substrate thickness compared to wavelength. The principle significance of these results is that modification must be made to Wheeler's low-frequency values for phase velocity and impedances if thick dielectrics are needed for low-loss circuits at high frequency.

Acknowledgments

The authors wish to acknowledge B. Hershenov for his encouragement and for technical discussions.

---

[5] S. S. Attwood, "Surface Wave Propagation Over a Coated Plane Conductor", *Jour. Appl. Phys.*, Vol. 22, p. 504 (1951).

SINGLE-FREQUENCY ARGON LASER

I. Gorog and F. W. Spong

RCA Laboratories
Princeton, N. J

Summary—The characteristics of the output spectrum of the argon ion laser are briefly described. Techniques that result in single-frequency operation are reviewed. Performance data of a 4880 Å single-frequency argon laser utilizing a Fox—Smith interferometer are presented. With this laser, holograms having a maximum path difference between object and reference beams of ~ 4 meters were made.

Introduction

THE SPECTRUM of a continuous-bore argon ion laser operating in a two-mirror cavity is characterized by extraordinary stability near threshold and by violent fluctuations in amplitude at high power levels. If the laser is operating without an axial magnetic field, the stable spectrum consists of a number of simultaneously operating modes separated by gaps of several longitudinal mode spacings.[1] In the presence of an axial magnetic field, the stable spectrum is characterized by oscillations at only two longitudinal modes. The frequency separation between the two modes is determined primarily by the axial magnetic field and the g-values of the states involved.[2] The width of the high-power unstable spectrum at high magnetic fields ($H > 1$ kilogauss) is approximately equal to the splitting of the stable spectrum.

Figure 1 shown the unstable spectrum at constant-discharge current and constant loss for four different field values for the 4880 Å transition. The laser employed in these experiments consisted of a 3-mm-diameter, 46-cm-long continuous-bore dc discharge, internal mode-controlling apertures, and a two-mirror cavity. The output coupling was ~ 5%. It is well known that the maximum power output as a function of magnetic field occurs at approximately one kilogauss.

[1] T. J. Bridges and W. W. Rigrod, "Output Spectra of the Argon Ion Laser," *IEEE J. of Quantum Electronics*, Vol. QE-1, No. 7, p. 303, Oct. 1965.

[2] I. Gorog and F. W. Spong, "An Approximate Linewidth Determination Method and the Magnetic-Field Tunable Stable Spectrum of the Argon Laser," *IEEE J. of Quantum Electronics*, Vol. QE-3, No. 12, p. 691, Dec. 1967.

Note, however, from Figure 1, that the effect of a low magnetic field (0–500 gauss) is both a broadening of the gain curve and an increase in oscillation amplitude. At higher fields (500 gauss to 1 kilogauss), the oscillation bandwidth increases, but the amplitude stays constant. At still higher fields, the bandwidth increases and the amplitude decreases.

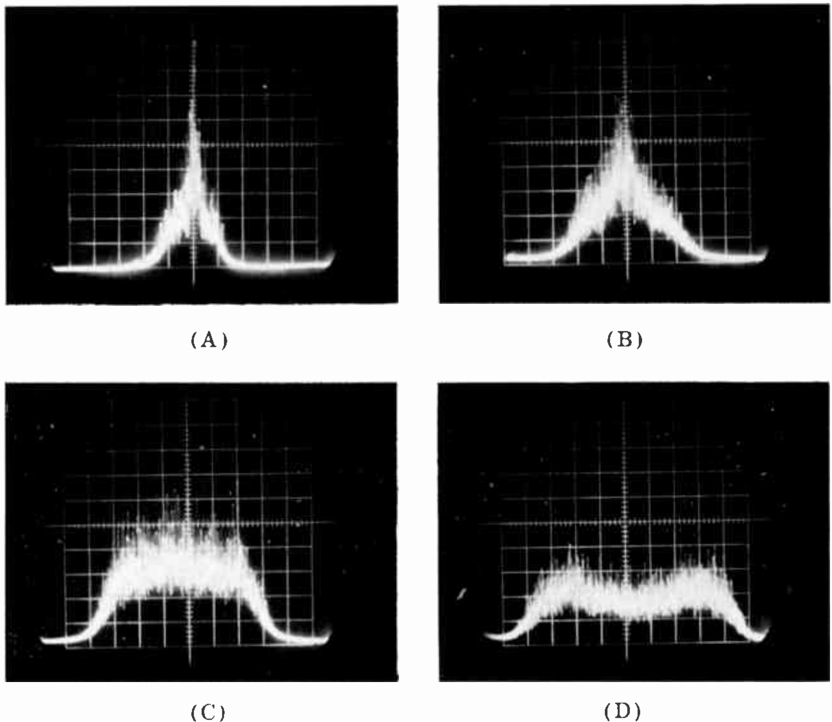

Fig. 1—The unstable spectrum of an argon laser. $I = 15$ A, $p = 0.4$ Torr, $\lambda = 4880$ Å. Vertical scale: arbitrary calibration, constant for (B) through (D), five times expanded for (A). Horizontal scale: 480 MHz per major division. Axial magnetic field: (A) zero; (B) 0.5 kilogauss; (C) 1.0 kilogauss; (D) 1.25 kilogauss.

Argon lasers are currently available with single-line cw power outputs in excess of 10 watts.[3] The high available power output and the convenient blue-green wave lengths make this laser an ideal source for a number of experiments. For some applications, e.g., communications and large-object holography, it is desirable to operate the laser in a stable high-power single-frequency mode.

[3] J. R. Fendley, Jr., and K. G. Hernqvist, private communication.

Review of Single-Frequency Technique

The techniques thus far employed to achieve single-frequency operation can be classified as follows: (1) those based on internal mechanisms,[4,5] (2) those based on external demodulation of an FM laser,[6,7] and (3) those based on interferometric techniques.[8-12]

The first group includes single frequency operation, both that which results from the competition of the dominant 4880 Å and 5145 Å lines and that which results from the use of segmented discharge tubes. The details of these two modes of operation are not clearly understood; however, they are important from the practical point of view, since they involve very few additional components beyond those required to achieve single-line operation.

It has been found that single-frequency oscillation at 5145 Å can be achieved by providing two separate cavities of unequal lengths for the 4880 Å and 5145 Å lines, using an axial magnetic field in the range of 600–650 gauss, and allowing both lines to operate stimultaneously.[4] (Under these conditions the 4880 Å line operates on two frequencies separated by approximately 1.5 GHz. This separation is approximately equal to the splitting of the low-power stable spectrum.[2]) If oscillation is blocked at either one of the two dominant lines, the other switches to the unstable multimode type of operation. Since the 4880 Å and 5145 Å transitions are coupled by their common terminal state, the single-frequency operation is probably the result of line and mode competition. The roles of the unequal cavity lengths and the magnetic field, however, are not clear. The single-frequency laser described above used a continuous-bore rf-excited discharge tube.

---

[4] J. M. Forsyth, "Single Frequency Operation of the Argon Ion Laser at 5145 Å," *Appl. Phys. Letters*, Vol. 11, No. 12, p. 391, 15 Dec. 1967.

[5] J. M. Yarborough and J. L. Hobart, "New High Power Stable Modes of Operation of the Argon Laser," *Appl. Phys. Letters*, Vol. 13, No. 9, p. 305, 1 Nov. 1968.

[6] L. M. Osterink and R. Targ, "Single-Frequency Light from an Argon FM Laser," *Appl. Phys. Letters*, Vol. 10, No. 4, p. 115, 15 Feb. 1967.

[7] A. Yariv, *Quantum Electronics*, pp. 318-320, John Wiley and Sons, Inc., New York, 1968.

[8] P. Zory, "Measurement of Argon Single-Frequency Laser Power and the 6328 Å Neon Isotope Shift Using an Interferometer Laser," *J. of Appl. Phys.*, Vol. 37, No. 9, p. 3643, Aug. 1966.

[9] P. Zory, "Single Frequency Operation of Argon Ion Lasers," *IEEE J. of Quantum Electronics*, Vol. QE-3, No. 10, p. 390, Oct. 1967.

[10] W. W. Rigrod and A. M. Johnson, "Resonant Mode Selector for Gas Lasers," *IEEE J. of Quantum Electronics*, Vol. QE-3, No. 11, p. 644, Nov. 1967.

[11] I. Gorog and F. W. Spong, "A High Power Single Frequency Laser and Its Application to Large Object Holograph," Post Deadline Paper No. EG7, presented at the A. P. S. Fall Meeting, Nov. 18, 1967, New York City.

[12] D. C. Sinclair, "A Confocal Longitudinal Mode Selector for Single-Frequency Operation of Gas Lasers," *Appl. Phys. Letters*, Vol. 13, No. 3, p. 98, 1 Aug. 1968.

A different high-power stable spectrum was observed in a dc-excited argon laser employing segmented graphite bore.[5] Simultaneous operation of the 4880 Å and 5145 Å lines in a single cavity results in stable multifrequency operation. When the laser is oscillating only at 4880 Å, with an axial magnetic field of approximately 1000 gauss, and at high excitation levels, three stable modes are present with more than 90% of power in the strongest central one. The behavior of the 5145 Å line is similar in the intermediate power range; however, at high-power levels it tends to switch to multifrequency. Again, the frequency-selection mechanisms are not understood. In addition to the mode competition and Zeeman splitting, the nature of the discharge bore is important. Such inherent stable single-frequency operation has not been observed with continuous-bore tubes.

Reliable high-power single-frequency output has also been obtained from a demodulated FM laser.[6] It is well known that if the optical length of a laser cavity is modulated at a rate slightly different from the longitudinal mode spacing, the output spectrum of a multimode laser corresponds to that of a frequency-modulated carrier.[7] Single-frequency light can be obtained from this FM wave by passing the FM laser output through an external phase modulator at the same frequency as, but out of phase with, the internal modulator.

Interferometric stabilization of the argon-laser spectrum has been studied by a number of workers and is probably the most developed of the various single-frequency techniques known.[8-12] Using an argon laser that incorporates an interferometric frequency selector, we have demonstrated that, in holography, the size of the object is no longer limited by laser coherence length.[11]

4880 Å Single-Frequency Argon Laser

An interferometer suitable for efficient internal single-frequency selection must be highly reflective in the vicinity of its resonance and highly transmissive at all other frequencies. The Fox–Smith interferometer satisfies these criteria well.[13] It is similar to the Michelson three-mirror arrangement, except that the beam splitter is rotated by 90°. The wave reflected by it in the direction of the incident wave is an exact analog of the wave transmitted through a Fabry–Perot interferometer.

The Fox–Smith interferometer we employed had a free spectral range of 7.5 GHz. Tuning is achieved by a piezoelectric driver. To

[13] P. W. Smith, "Stabilized Single Frequency Output from a Long Laser Cavity," *IEEE J. of Quantum Electronics*, Vol. QE-1, No. 8, p. 343, Nov. 1965.

minimize front-surface reflection losses the beam splitter was set at Brewster's angle. The beam splitter reflectivity was ~ 50% for waves incident at Brewster's angle; the other two mirrors were coated for maximum reflectivity at 4880 Å. As a result of the low beam-splitter reflectivity the finesse was low; strong mode competition, however, assured single-frequency operation throughout the entire excitation range investigated.

Using this interferometer in place of an end mirror, we achieved excellent longitudinal mode selection. Figure 2 shows the laser spectrum observed with a scanning spherical interferometer. The oscillo-

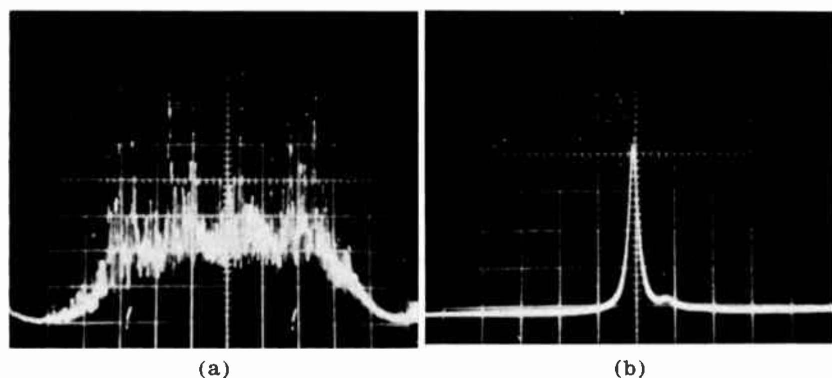

(a) (b)

Fig. 2—Argon 4880 Å output spectrum, 11 A dc, 750 gauss axial magnetic field. Horizontal scale is 320 MHz per major division; vertical scales is arbitrary. (a) Two-mirror cavity; (b) interferometer in place of one of the end mirrors.

gram in Figure 2(a) was taken with the laser operating in a two-mirror cavity; for Figure 2(b), one of the end mirrors was replaced by the interferometer. The cavity losses and geometry were adjusted to be the same in both cases. Power measurements showed that, as expected, at high currents (~ 25 amperes), i.e., at a high degree of saturation, the single-frequency and multifrequency power outputs are essentially the same.

Figure 3 shows the 4880 Å single-frequency argon-laser output as a function of excitation current at zero and at 1100-gauss axial magnetic field. The interferometer insertion loss, as determined from threshold measurements, was ~ 9%. The output coupling was 10%. Again a 3-mm-diameter 46-cm-long continuous bore dc discharge was employed. Each datum point was taken with the laser frequency

carefully adjusted to correspond to the frequency of maximum emission, as determined by the degree of excitation and by the losses.

The effect of transverse mode competition was also observed during these measurements. When the internal-mode-controlling aperture was opened sufficiently to allow simultaneous operation of a number of transverse modes, the output spectrum fluctuated strongly and the peak

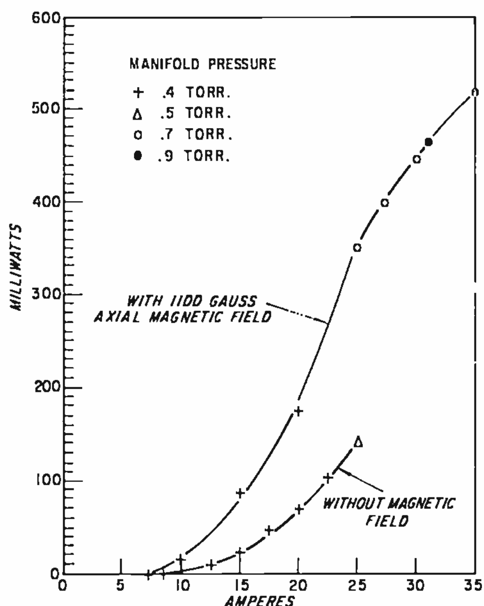

Fig. 3—Power output the single-frequency laser at 4880 Å. Manifold pressure adjusted to correspond to approximate optimum.

amplitude of the fundamental mode was reduced (~ 25 to 50%) with respect to the stable, single-frequency, single-transverse-mode operation.

The single-frequency output power with zero axial magnetic field was also computed theoretically. The saturation characteristics were obtained from the curves shown on Figure 4. The current dependence of the gain was determined from threshold measurements. Uncertainties associated with the effective volume were eliminated by normalizing the theoretically computed power values to the 25-ampere datum point. Good agreement between theory and experiment was found.

In Figure 4, the fraction of the total available power that is coupled into the oscillating single-frequency mode is plotted as a function of

gain saturation. P is the power emitted into the single oscillating mode. P_{∞} is the total available power in the laser transition, i.e., the effective pumping rate times the quantum energy. The gain satura-

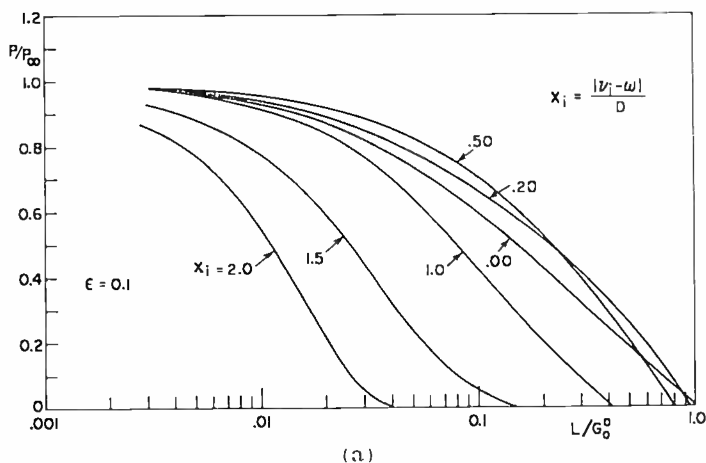

(a)

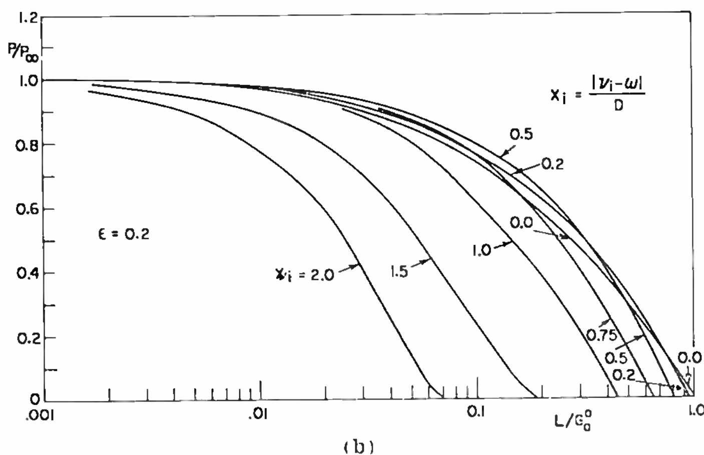

(b)

Fig. 4—Power versus saturation for inhomogeneously broadened gaussian lines.

tion $L/G_o^0 = \log_e(1 + l)/\log_e(1 + g)$, where l is the total loss (coupling plus internal) and g is the unsaturated round-trip gain at line center. The oscillator detuning from line center normalized against the doppler-width parameter (i.e., the $1/e$ point half-width of the doppler profile) is denoted by x_i; ϵ is the ratio of one half of the homogeneous line width to the doppler parameter. The curves in Figure 4 were obtained from self-consistent numerical solutions of the integral equation that relates

the induced emission rate to the cavity losses. This integral equation was based on a rate-equation formulation similar to that suggested by Lamb.[14]

The published line-width data[2,9] indicate that for the ionized argon 4880 Å transition, $\epsilon \simeq 0.1 - 0.2$. Recent experiments indicate that the lower laser level is depopulated via nonradiative transitions.[15] Therefore, the Lorentzian width should depend on all experimental variables determining the state of the discharge. Measured values for the full Lorentzian width of the 4880 Å transition under typical laser conditions range from 360 to 700 MHz.[9] The purpose of our calculations was to obtain quantitative estimates of the efficiency of single-frequency operation. From Figure 4, with proper tuning, $P/P_x = 0.52$ for $\epsilon = 0.1$ and $P/P_x = 0.66$ for $\epsilon = 0.2$ at the practical value of $L/G_0{}^o = 0.2$. Therefore, we conclude that regardless of the uncertainty of the Lorentzian width in high-power argon lasers, more than half of the total available power can be coupled into a single oscillating mode.

Experimental determination of the total available power is difficult. However, at high excitation levels and under identical loss and excitation conditions, the multifrequency (two-mirror cavity) and single-frequency power outputs were found to be the same.

In standard holographic setups, the coherence length of the laser limits the permissible object size to a few centimeters. Furthermore, even if the object size is sufficiently small, great care must be exercised in balancing the path lengths of the object and reference beams. These limitations do not apply if a single-frequency laser is used.

We have photographed Michelson interference fringes with good visibility at a path length difference of 11 meters. We have also made high-quality holograms of two-dimensional objects with the path lengths intentionally unbalanced. Path-length differences in excess of 3 meters did not have any apparent effect on the quality of the holograms. Finally, we have made holograms with object depths ranging up to two meters. Because the object was illuminated from behind the film plate, the maximum path length difference in this arrangement was ~ 4 meters.

ACKNOWLEDGMENT

We offer our thanks to John A. van Raalte and Richard A. Simonelli for their contributions during various phases of this work.

---

[14] W. E. Lamb, Jr., "Theory of an Optical Maser," *Phys. Rev.*, Vol. 134, No. 6A, p. 2602, Sept. 1963.

[15] H. Merkelo, R. M. Wright, J. P. Kaplafka, and E. P. Bialecke, "Vacuum Ultraviolet Perturbation Spectroscopy of the Argon Ion Laser," *Appl. Phys. Letters*, Vol. 13, No. 12, p. 401, 15 Dec. 1968.

VAPOR PRESSURE DATA FOR THE SOLID AND LIQUID ELEMENTS

By

Richard E. Honig and Dean A. Kramer

RCA Laboratories
Princeton, N. J

Summary—Vapor pressures, melting and boiling points, and their associated energies have been selected, evaluated, tabulated, and plotted for 81 elements that are solid or liquid at room temperature. Vapor pressures have been plotted as log p (Torr) versus log T (°K). This collection contains data available before the end of 1968.

Introduction

Since the 1962 edition of vapor pressure data for 79 elements that are solid or liquid at room temperature (**26**), a large volume of new information has become available that warrants publication of a third edition. The present paper presents information, published as well as unpublished, for 81 solid or liquid elements and covers the period up to the end of 1968.

Data and Computations

The vapor pressure data utilized in this paper come from the following major sources: "Selected Values for the Thermodynamic Properties of Metals and Alloys," by Hultgren and collaborators (**27**); "JANAF Thermochemical Tables," by Stull and collaborators (**28**); a thorough literature search covering articles, reports, and abstracts available before July 1, 1968; and a number of private communications concerning unpublished work. In addition, it was possible to include a few articles that came to our attention before December 1968.

To keep the list of references short, the two major collections mentioned above (**27,28**), rather than the original articles, have been quoted wherever feasible. In all those cases where the data had not changed from the previous edition (**26**), it has been given as reference. During the course of the literature search, a total of some 130 per-

tinent articles, reports, and abstracts were consulted, out of which about 60 were selected and quoted. In addition, there are in existence several general collections of heats of sublimation by Brewer (**14**), Feber (**19**), Rosenblatt (**45**), and Wagman et al (**50**). Extensive vapor pressure measurements were made by Habermann and Daane (**21**) on most of the rare earth elements. They were recomputed by Gschneidner (**20**) and by Hultgren (**27**), whose values have been given here. Since Nesmeyanov's book, entitled *Vapor Pressure of the Chemical Elements* (**38**), contains no data beyond 1962, it will be quoted only where it presents new information.

References presenting results that appear seriously out of line with other work have been omitted. Since this compilation is based on the data of many workers who measured vapor pressures by different techniques under widely differing experimental conditions, it is often very difficult to choose between two apparently equivalent sets of results, and at times the preference expressed here may be subjective and arbitrary.

To compare vapor pressure data from various sources, they were plotted on log p versus log T graphs, where p is in Torr (mm Hg) or atm, and T in °K. To facilitate the eventual switch-over to the MKS International System, recommended by NBS, a pressure scale in newtons/meter^2 (N/m^2) has been added to the graphs (1 atm = 760 Torr = 1.0133×10^5 N/m^2). Hultgren's data (**27**) for many metals, tabulated as temperatures at given pressures, could be plotted directly. The JANAF data (**28**), tabulated as log p (atm) at given temperatures, could be put directly on the log p versus log T plots with the help of a special scale. Many of the individual references present experimental results in terms of the general equation

$$\log_{10} p = AT^{-1} + B \log_{10} T + CT + DT^2 + E, \qquad (1)$$

where

p = pressure, expressed in this paper in Torr (mm Hg)
T = absolute temperature, in °K
A,B,C,D,E = coefficients characteristic of the element (in most cases, only A and E are used).

A computer was employed to determine from Equation (1) the temperatures corresponding to fixed pressures, starting at 10^3 and going in decade steps down to 10^{-13} Torr. The data were checked for accuracy and correctness of transcription by comparing the computed boiling point for each element with the known value and by checking to see if

the pressures obtained from the solid and liquid equations matched at the melting point. The tabulated results were then plotted over the range 10^3 to 10^{-11} Torr.

For the elements whose gas phase is made up of two or more species of known concentrations, total vapor pressures were obtained by adding the individual curves graphically. These cases are identified by a Σ preceding the chemical symbol. For those elements that are made up predominantly of atomic species, contributions from molecular species have been neglected, and the symbol is given without a subscript. For the few elements that consist predominantly of one molecular species, the appropriate subscript has been added.

In a number of cases, the vapor pressure equation is known for the solid, but not for the liquid phase, and in a few instances the reverse is true. To obtain data from the missing temperature range, the following approximation was employed. Assuming coefficients B, C, and D of Equation (1) to be zero, the vapor pressure at the melting point can be expressed by

$$\log_{10} p_{MP} = -\frac{A_s}{T_{MP}} + E_s = -\frac{A_l}{T_{MP}} + E_l \tag{2}$$

where subscripts "s" and "l" refer to the solid and liquid states, respectively. From the well-known Clausius–Clapeyron equation it follows that

$$A_s = \frac{1000\Delta H_{S,T}}{4.576}, \quad A_l = \frac{1000\Delta H_{V,T}}{4.576} \tag{3}$$

where

$\Delta H_{S,T}$ = heat of sublimation at temperature T, in kcal/mol.

$\Delta H_{V,T}$ = heat of evaporation at temperature T, in kcal/mol.

Finally,

$$\Delta H_{S,T} = \Delta H_{V,T} + \Delta H_M \tag{4}$$

where

ΔH_M = heat of melting, in kcal/mol.

Thus, Equations (2), (3), and (4) permit computation of approximate vapor pressures for the liquid from solid-phase data and the heat of melting, and vice-versa.

As seen below, for a substantial number of elements the gas phase contains two or more species, each having its individual heat of sublimitation, ΔH_S. Where feasible, these energies have been determined by mass spectrometric means, but in some cases the value for the dimer, $\Delta H_S(X_2)$, is obtained from the cycle

$$\Delta H_S(X_2) = 2\Delta H_S(X_1) - D_0(X_2) \tag{5}$$

where

$\Delta H_S(X_1)$ = heat of sublimation of monomer, in kcal/mol

$D_0(X_2)$ = dissociation energy of dimer, in kcal/mol, determined from spectral band data.

RESULTS

Table I presents the desired vapor pressure data over the range 10^{-11} to 10^3 Torr, together with literature references and the temperature range of the original data. To simplify the tabulation, temperatures have been quoted to ± 1° below 500°K; to ± 2° between 500 and 1000°K; to ± 5° between 1000 and 2000°K; and to ± 10° above 2000°K. These values reflect the accuracy with which the curves in Figures 1A through 1C can be read. However, it is rare for pressure measurements to be made to better than ± 20%, which corresponds to a temperature uncertainty of between one and two percent. Thus, the last figure quoted in Table I may not be significant. The symbol ◉, inserted between the appropriate columns, indicates the melting point, thus defining at a glance the solid and liquid ranges.

Figure 1 presents the vapor pressure data in graphical form on three separate sheets.* To locate a given element, the column marked "Curve Sheet" in Table I should be consulted. Sheet A contains mostly elements from the first half of the alphabet, Sheet B those from the second half, and Sheet C the lanthanides and actinides. Estimated curves are shown dashed. However, placement of some of the elements was determined by the need to minimize excessive overlapping of curves. The circled point ◉ shown on most curves is again the melting

* Reproductions are available in two sizes, 20 × 25 and 8½ × 11 inches; requests for copies should be addressed to Technical Publications, RCA Laboratories, David Sarnoff Research Center, Princeton, N. J. 08540.

point. The letters "s" (solid) or "l" (liquid) have been appended to the chemical symbol if the melting point falls outside the range of the graph. In cases where vapor pressures had to be extrapolated without the help of adequate thermochemical data, the solid portion of the curve represents the measured range, while extrapolations are indicated by dashes. For some elements, there exist several different, but apparently equivalent, sets of vapor pressure data as determined by different workers. Where these measurements appear equally reliable, the set nearest the mean has been selected.

Table II summarizes temperatures (°K) and energies (kcal/mol) for the melting and vaporization processes of the elements, as well as the references selected. The significant figures shown and errors quoted are usually those of the original articles and may, in many instances, give an over-optimistic impression of the accuracy of the data. Three different vaporization energies are quoted whenever available: ΔH_V, the heat of vaporization at the boiling point; $\Delta H_{S,0}$, the heat of sublimation at 0°K; and $\Delta H_{S,298}$, the heat of sublimation at 298°K. If the gas phase contains several species, they are arranged in the order of relative abundance at the boiling point, and energies are quoted for each. Estimated values are shown in parentheses. Different, but equivalent, values obtained by different workers have been listed with their corresponding references. Although heats of transformation and their corresponding temperatures can be found in Hultgren's collection (27) for a number of elements, these data were not included in Table II because of space limitations.

Discussion

The present edition contains information on most elements that are solid or liquid at room temperature. In some instances, however, the data are only rough estimates, or there is not yet satisfactory agreement between different sets. These cases are discussed briefly below.

Ac: The vapor pressure data were obtained by plotting an estimated curve through the experimentally determined boiling point (26).

Am: The present values are based on earlier data (26) available in the temperature range 1043 to 1453°K, slightly modified by Hultgren (27). Graphical extrapolation ranges are shown dashed in Figure 1C.

As: The recent detailed vaporization study by Herrick and Feber (24) has yielded for As_4, the predominant species, a heat of sub-

limation that is significantly higher than the value selected by Hultgren (**27**), as shown in Table II. This is due to the fact that Herrick and Feber went to great lengths to eliminate the considerable concentration of As_2O_3 known to be generally present even in the purest arsenic samples commercially available. Their vapor pressure values, which lie substantially below those previously accepted (**26**), have been plotted in Figure 1A and are presented in Table I.

At: The data used (**26**) are only a rough estimate, obtained by extrapolation from other halogens.

Au: While the vapor pressure of gold has been known accurately for some time (**26**), the recent detailed study by Ward (**52**) deserves attention. This author showed that there exists a small, but significant dependence of ΔH_S on the physical shape of the sample.

B: The experimental difficulties encountered in handling this element have not been resolved to date, and the reported range of ΔH_S values is still as wide as previously indicated (**26**). The vapor pressure curve presented here is based on data selected by Hultgren (**27**).

Ba: Until recently, the few data available for this technically important element were over 30 years old and could not be reconciled. They were reviewed and evaluated by Hultgren (**27**) and Nesmeyanov (**38**). Fortunately, two new studies by Bohdansky and Schins (**10**) and Zavitsanos (**55**) appear to have resolved all problems and are quoted in Table I and plotted in Figure 1C.

Bi: The vapor pressure data available for this element were reviewed in 1968 by Hultgren and collaborators (**27**), who selected heats of vaporization for the two major species Bi_2 and Bi_1 and summed up the two partial pressures to obtain the total. Two recent mass spectrometric studies, published by Kohl et al (**30A**) and Rovner and collaborators (**45A**) confirm these results. In addition, both groups found small concentrations (at the percent level) of Bi_4 and perhaps also Bi_3 and could compute heats of vaporization for one or both of these species.

Fr: The estimated values (**26**) are based on a comparison with other alkali metals.

Gd: The values of ΔH_S listed (**27,33**) in Table II are probably representative of pure samples of this element. The much lower value previously reported (**53**) can be explained (**33**) by the presence of a volatile impurity in the sample studied.

In: In spite of a number of detailed studies recently reported in the literature (**3,22,27,34**), the heat of sublimation for this element is not as well defined as might be expected. Following the suggestion made by Macur et al (**34**), a weighted average of 57.5 ± 1.0 kcal/mol was chosen for $\Delta H_{S,298}$.

Pm: An estimated vapor pressure curve was drawn through the boiling point proposed by Gschneidner (**20**).

Po: The previously reported (**26**) vapor pressure data have been retained.

S: Vapor pressure data for this element were reviewed in 1965 by Stull and collaborators (**28**) who quote ΔH_S values for the species S_8, S_2, and S_1. However, Berkowitz and Marquart (**6A**) have shown in a mass spectrometric study that, at lower temperatures, S_8 and S_6 predominate in the saturated vapor, while at the well-defined boiling point of 717.75°K, the three major species are S_8, S_7, and S_6, with S_5, S_4, and S_2 contributing between three and ten mole percent.

Se: This is one of the more complex elements in terms of the number of different species found in the vapor phase. For many years, it was assumed (**6,26,50**) that the major species were Se_2, Se_6, and Se_1. Recent mass spectrometric studies (**6B,6C,19A,54**) on the composition of selenium vapor have clearly shown, however, that the molecular species include, in descending order of concentration, Se_5, Se_2, Se_6, Se_7, Se_3, and Se_8. The heats of sublimation derived by Berkowitz and Chupka (**6B**), presented in Table II, lie some three kcal/mol above those quoted by Fujisaki et al (**19A**). The total vapor pressure curve shown is a composite, based on Yamdagni and Porter's (**54**) data in the low temperature region, and References (**6,12,54**) at the high end.

U: The recent study by Ackermann and Rauh (**2**) leads to a heat of sublimation $\Delta H_{S,298} = 126.3 \pm 1.0$ kcal/mol that is in good agreement with the value measured earlier by Drowart et al (**17A**) and selected by Hultgren and collaborators (**27**). This puts an end to a controversy that has lasted well over a decade.

ACKNOWLEDGMENT

This review has benefited greatly from advance information kindly made available to the authors by many research workers in the field. Their reports and publications have been quoted in the Reference Section, but, owing to the large number involved, it is not feasible to list their names here individually. Their generous assistance is hereby gratefully acknowledged.

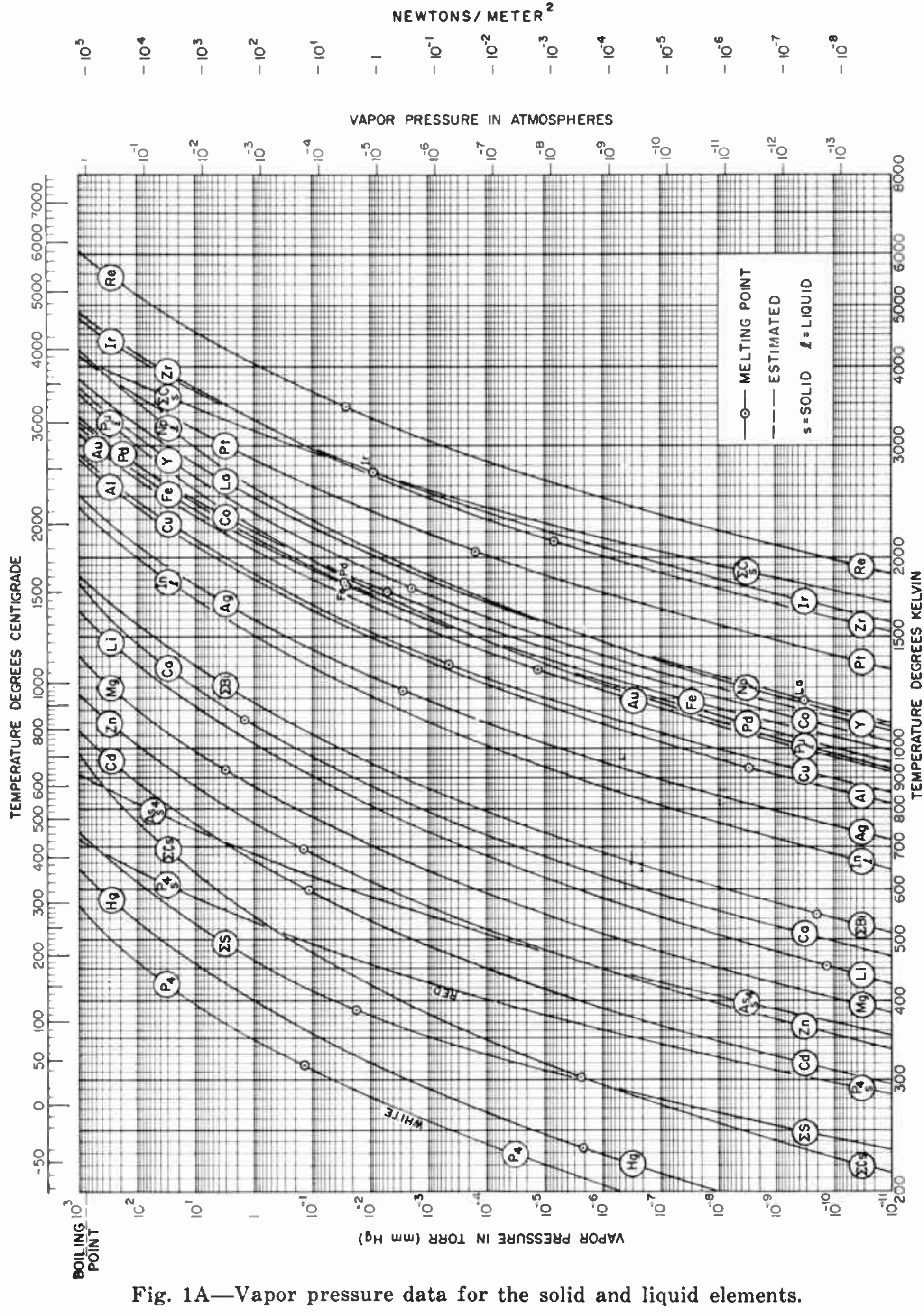

Fig. 1A—Vapor pressure data for the solid and liquid elements.

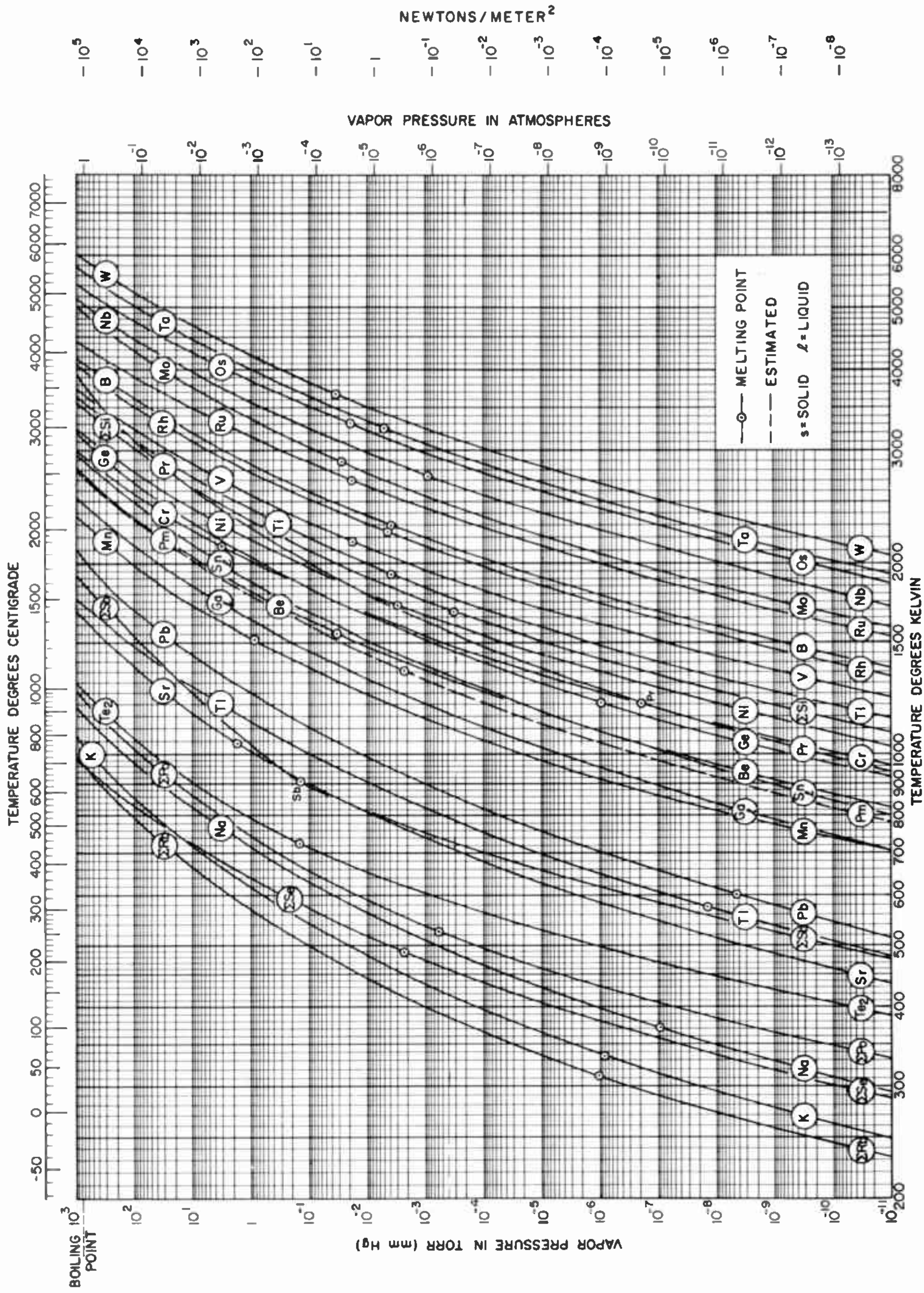

Fig. 1B—Vapor pressure data for the solid and liquid elements.

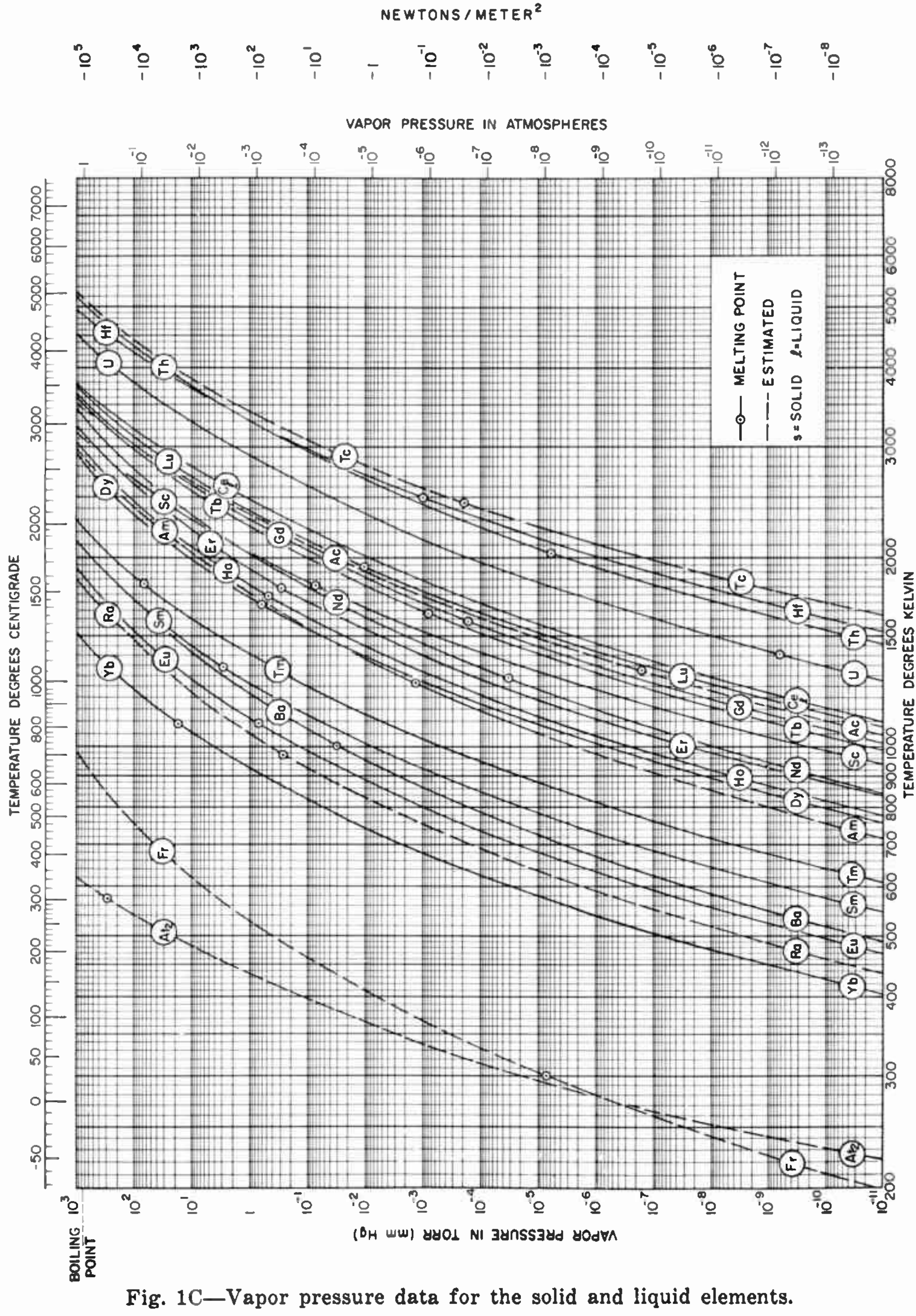

Fig. 1C—Vapor pressure data for the solid and liquid elements.

Table I—Vapor Pressure Data for the Solid and Liquid Elements (1 of 3)

SYMBOL	ELEMENT	CURVE SHEET	REFERENCES	DATA TEMP. RANGE, °K	TEMPERATURES (°K) FOR VAPOR PRESSURES (TORR)														
					10^{-11}	10^{-10}	10^{-9}	10^{-8}	10^{-7}	10^{-6}	10^{-5}	10^{-4}	10^{-3}	10^{-2}	10^{-1}	1	10^{1}	10^{2}	10^{3}
Ac	ACTINIUM	C	26	1873, EST	1045	1100	1160	1230	1305 ⊙	1390	1490	1605	1740	1905	2100	2350	2660	3030	3510
Ag	SILVER	A	27	994–2425	720	758	798	844	898	954	1020	1100	1190 ⊙	1300	1430	1600	1810	2090	2500
Al	ALUMINUM	A	27,28	1313–1723	820	862	910 ⊙	960	1020	1090	1175	1265	1370	1495	1650	1845	2090	2410	2850
Am	AMERICIUM	C	27	1043–1453, EST.	718	756	802	854	912	978	1055	1145	1255 ⊙	1385	1545	1760	2040	2420	2970
As_4	ARSENIC (s)	A	24	522– 714	354	370	388	408	428	452	480	508	544	584	630	680	742	820	912
At_2	ASTATINE	C	26	EST.	221	231	241	252	265	280	296	316	338	364	398	434	480	540 ⊙	620
Au	GOLD	A	26,42,52	1400–2142	920	972	1025	1085	1160	1235	1325 ⊙	1425	1545	1685	1850	2060	2330	2670	3140
B	BORON	B	27	1822–2152	1370	1440	1515	1600	1690	1795	1910	2040	2200 ⊙	2380	2600	2660	3200	3610	4150
Ba	BARIUM	C	10,55	1102–2024	490	518	550	586	626	672	726	788	862	952 ⊙	1070	1220	1420	1705	2130
Be	BERYLLIUM	B	27,28	1174–2331	824	866	914	964	1025	1090	1170	1255	1360	1480 ⊙	1630	1820	2050	2370	2810
ΣBi	BISMUTH	A	10,27,49	770–2082	512	540 ⊙	570	606	644	688	738	796	868	950	1055	1180	1350	1575	1875
ΣC	CARBON (s)	A	27	1800–3050	1700	1775	1855	1940	2040	2150	2270	2400	2570	2740	2940	3170	3440	3770	4150
Ca	CALCIUM	A	27	640–1546	471	497	526	556	592	630	678	732	796	876	966	1080 ⊙	1250	1470	1820
Cd	CADMIUM	A	27,35	411–1040	295	312	328	346	367	390	418	450	490	536	592 ⊙	664	760	884	1070
Ce	CERIUM (ℓ)	C	27	1715–2252	1100	1155	1220	1290	1370	1465	1575	1695	1845	2010	2220	2490	2800	3210	3770
Co	COBALT	A	27,28	1363–1522	1025	1080	1140	1205	1275	1355	1450	1550	1670 ⊙	1815	1990	2200	2460	2810	3250
Cr	CHROMIUM	B	27	1162–1805	960	1010	1065	1120	1180	1255	1335	1430	1545	1670	1830	2010 ⊙	2260	2580	3000
ΣCs	CESIUM	A	1,10,28	303–1558	213	226	241	256	273	294 ⊙	319	348	382	424	476	542	638	772	980
Cu	COPPER	A	27,28,44	987–1879	856	898	944	998	1060	1125	1205	1290 ⊙	1400	1530	1690	1890	2130	2460	2920
Dy	DYSPROSIUM	C	27	1123–1666	760	798	844	892	948	1015	1085	1170	1270	1395	1545 ⊙	1730	1985	2360	2920
Er	ERBIUM	C	27	1192–1859	840	880	928	980	1040	1110	1190	1280	1400	1530	1700 ⊙	1920	2210	2610	3240
Eu	EUROPIUM	C	27	650– 900	470	495	524	556	594	634	682	739	802	886	984 ⊙	1110	1280	1540	1930
Fe	IRON	A	27,28	1389–1889	996	1045	1100	1160	1225	1305	1385	1485	1605	1745 ⊙	1920	2120	2390	2720	3220
Fr	FRANCIUM	C	26	EST.	198	210	225	242	260	280 ⊙	306	334	368	410	462	528	620	760	980
Ga	GALLIUM (ℓ)	B	37	1174–1603	708	746	790	838	892	954	1025	1105	1205	1320	1460	1630	1850	2140	2530
Gd	GADOLINIUM	C	27	1574–2070	1015	1070	1130	1195	1265	1350	1450	1565 ⊙	1700	1860	2060	2300	2610	3020	3650
Ge	GERMANIUM	B	27	1418–2070	922	966	1015	1070	1130 ⊙	1215	1300	1400	1520	1665	1840	2050	2320	2630	3200
Hf	HAFNIUM	C	27	2035–2363	1525	1605	1695	1785	1900	2010	2150	2310	2500 ⊙	2710	2980	3310	3720	4260	4970

Table I—Vapor Pressure Data for the Solid and Liquid Elements (2 of 3)

SYMBOL	ELEMENT	CURVE SHEET	REFERENCES	DATA TEMP. RANGE, °K	TEMPERATURES (°K) FOR VAPOR PRESSURES (TORR)														
					10^{-11}	10^{-10}	10^{-9}	10^{-8}	10^{-7}	10^{-6}	10^{-5}	10^{-4}	10^{-3}	10^{-2}	10^{-1}	1	10^{1}	10^{2}	10^{3}
Hg	MERCURY	A	25,27,28	193– 707	170	180	190	200	214	229 ⊙	246	266	289	320	353	400	458	534	642
Ho	HOLMIUM	C	27,51	928–2023	780	822	870	920	980	1045	1120	1215	1320	1450	1605 ⊙	1805	2080	2460	3050
In	INDIUM (ℓ)	A	3,22,27,34	648–2273	644	680	720	766	812	870	936	1015	1105	1215	1345	1505	1720	2000	2400
Ir	IRIDIUM	A	27,41	1986–2630	1580	1670	1760	1850	1950	2070	2210	2360	2540 ⊙	2750	2990	3290	3670	4130	4750
K	POTASSIUM	B	13,25,28,48	725–1037	248	261	277	294	315 ⊙	337	364	395	434	482	540	618	718	852	1070
La	LANTHANUM	A	27	1655–2167	1100	1165 ⊙	1230	1305	1385	1475	1580	1710	1850	2020	2230	2490	2810	3230	3820
Li	LITHIUM	A	10,25,28	734–1881	426	452 ⊙	478	508	544	580	624	678	738	810	906	1020	1165	1360	1650
Lu	LUTETIUM	C	27	1651–1930	1075	1130	1195	1260	1340	1420	1515	1635	1775	1935 ⊙	2130	2370	2700	3130	3760
Mg	MAGNESIUM	A	27,28	495–1370	383	403	427	451	480	512	550	592	642	702	780	868 ⊙	984	1150	1410
Mn	MANGANESE	B	27,46	1043–1987	708	740	778	818	864	918	980	1055	1140	1245	1370 ⊙	1520	1720	2000	2370
Mo	MOLYBDENUM	B	27,28	1200–2533	1590	1670	1755	1845	1950	2070	2210	2370	2560	2780 ⊙	3030	3360	3770	4300	5000
Na	SODIUM	B	10,25,28,48	864–1390	293	311	328	349 ⊙	372	397	430	467	508	562	632	716	824	968	1180
Nb	NIOBIUM	B	27	2304–2596	1720	1810	1905	2010	2130	2250	2390	2560 ⊙	2750	2970	3250	3570	3970	4470	5120
Nd	NEODYMIUM	C	27	1170–1923	846	894	948	1010	1075	1150	1240 ⊙	1345	1465	1610	1800	2020	2340	2790	3440
Ni	NICKEL	B	27	1252–1895	1030	1085	1145	1205	1275	1350	1440	1545	1660 ⊙	1800	1970	2180	2450	2790	3240
Np	NEPTUNIUM (ℓ)	A	18	1700–1950	1085	1145	1215	1290	1375	1475	1590	1720	1875	2070	2300	2580	2980	3530	4250
Os	OSMIUM	B	16,40	2157–2800	1865	1960	2060	2170	2300	2440	2600	2780	2980	3230 ⊙	3510	3850	4260	4770	5420
P_4	PHOSPHORUS, RED (s)	A	26		283	297	312	327	342	361	381	402	430	458	493	534	582	642	716
P_4	PHOSPHORUS, WHITE	A	38		146	156	166	178	191	205	220	238	259	282	311 ⊙	348	396	463	564
Pb	LEAD	B	27,29	875–1597	515	546	580 ⊙	614	656	702	758	822	900	990	1105	1250	1440	1700	2100
Pd	PALLADIUM	A	27,47	1253–1841	952	1005	1065	1125	1200	1275	1370	1475	1600	1750 ⊙	1925	2150	2430	2800	3330
Pm	PROMETHIUM	B	20	EST.	782	826	872	920	980	1045	1120	1210	1315 ⊙	1445	1600	1790	2020	2330	2800
ΣPo	POLONIUM	B	26	711–1286	332	348	365	384	408	432	460	494 ⊙	538	588	656	744	862	1025	1250
Pr	PRASEODYMIUM	B	27	1210–2120	940	990	1050	1110	1180 ⊙	1265	1365	1480	1625	1795	2000	2270	2620	3100	3920
Pt	PLATINUM	A	26	1697–2042	1335	1405	1480	1565	1655	1765	1885	2020 ⊙	2180	2370	2590	2860	3190	3610	4170
Pu	PLUTONIUM (ℓ)	A	27,36	1100–1800	928	980	1035	1105	1180	1265	1360	1475	1615	1780	1980	2230	2560	3000	3600
Ra	RADIUM	C	26	EST.	436	460	488	520	552	590	638	690	756	830	920 ⊙	1060	1225	1490	1840

Table I—Vapor Pressure Data for the Solid and Liquid Elements (3 of 3)

SYMBOL	ELEMENT	CURVE SHEET	REFERENCES	DATA TEMP. RANGE, °K	TEMPERATURES (°K) FOR VAPOR PRESSURES (TORR)														
					10^{-11}	10^{-10}	10^{-9}	10^{-8}	10^{-7}	10^{-6}	10^{-5}	10^{-4}	10^{-3}	10^{-2}	10^{-1}	1	10^{1}	10^{2}	10^{3}
ΣRb	RUBIDIUM	B	10,27	523– 969	232	244	257	272	290	312 ⊙	335	364	400	443	498	570	660	794	990
Re	RHENIUM	A	7,26,43,47	2350–3191	1890	1985	2090	2210	2340	2490	2650	2850	3070	3330 ⊙	3650	4040	4550	5200	6050
Rh	RHODIUM	B	26,47	1709–2205	1330	1395	1470	1550	1640	1745	1855	1980	2130 ⊙	2310	2520	2780	3110	3520	4070
Ru	RUTHENIUM	B	16,40	1940–2377	1535	1610	1690	1785	1885	2000	2130	2280	2450	2650 ⊙	2880	3160	3490	3900	4410
ΣS	SULFUR	A	28		232	242	253	266	279	294	311	328	352	380 ⊙	415	465	532	620	732
ΣSb	ANTIMONY	B	27	618– 861	476	500	526	554	584	620	658	702	754	818	888 ⊙	1030	1250	1535	1920
Sc	SCANDIUM	C	27	1200–1812	940	986	1035	1095	1160	1230	1320	1420	1530	1660 ⊙	1830	2030	2300	2680	3190
ΣSe	SELENIUM	B	6,12,54	432– 979	286	301	317	336	357	380	407	438	474 ⊙	518	572	638	722	832	980
ΣSi	SILICON	B	28	1399–2054	1085	1140	1200	1260	1335	1415	1505	1620 ⊙	1750	1905	2100	2330	2630	3020	3550
Sm	SAMARIUM	C	23,28	928–1160	548	576	608	644	686	732	784	850	922	1015	1120	1260 ⊙	1450	1720	2120
Sn	TIN (ℓ)	B	27,39	1371–1753	800	846	898	952	1020	1090	1170	1270	1380	1510	1680	1885	2150	2500	2940
Sr	STRONTIUM	B	8,10,27	673–1979	436	459	485	512	548	584	628	680	740	810	900	1010 ⊙	1160	1380	1695
Ta	TANTALUM	B	27	2000–3269	1925	2010	2120	2230	2370	2510	2680	2870	3070 ⊙	3330	3630	4000	4460	5020	5780
Tb	TERBIUM	C	27	1598–1918	990	1040	1100	1165	1230	1315	1410	1515 ⊙	1645	1805	2000	2240	2560	2980	3600
Tc	TECHNETIUM	C	31	1927–2273,EST.	1620	1700	1785	1875	1980	2110	2240	2400 ⊙	2580	2810	3080	3420	3850	4430	5250
Te_2	TELLURIUM	B	5,27,32	481–1780	369	406	426	447	472	498	528	564	606	652	712 ⊙	790	932	1065	1295
Th	THORIUM	C	27	1757–1956	1460	1530	1615	1705	1815	1930 ⊙	2070	2240	2440	2670	2960	3300	3750	4350	5200
Ti	TITANIUM	B	27,28,47	1373–1820	1140	1195	1260	1325	1405	1490	1590	1710	1845 ⊙	2000	2200	2440	2730	3120	3640
Tl	THALLIUM	B	10	1312–1892	481	508	538	570 ⊙	608	650	700	758	824	904	1000	1125	1280	1485	1765
Tm	THULIUM	C	27	809–1219	608	640	678	718	764	818	878	948	1035	1125	1250	1405	1600 ⊙	1875	2300
U	URANIUM	C	2,27	1775–2174	1275	1345 ⊙	1425	1500	1600	1710	1835	1975	2150	2350	2600	2900	3300	3800	4500
V	VANADIUM	B	27	1666–1882	1230	1290	1360	1430	1510	1605	1705	1825	1960	2120 ⊙	2320	2560	2860	3230	3740
W	TUNGSTEN	B	27,28	2389–3137	2060	2160	2280	2390	2520	2680	2840	3020	3260	3500 ⊙	3830	4220	4700	5280	6010
Y	YTTRIUM	A	27	1331–2178	1070	1120	1180	1245	1320	1405	1500	1620	1750 ⊙	1905	2100	2360	2690	3110	3700
Yb	YTTERBIUM	C	11,20,27,33	623–1760	404	426	450	477	504	540	580	624	680	744	824	922	1065 ⊙	1230	1520
Zn	ZINC	A	4,17,26	422–1089	336	354	374	396	421	450	482	520	566	618	682 ⊙	760	870	1010	1210
Zr	ZIRCONIUM	A	27,28	1949–2274	1525	1605	1690	1780	1890	2010 ⊙	2150	2300	2490	2710	2980	3300	3700	4200	4870

Table II—Melting and Vaporization Data for the Solid and Liquid Elements (1 of 5)

SYMBOL	MELTING MP °K	ΔH_M kcal/mol	REF	VAPORIZATION BP °K	SPECIES	ΔH_V @ BP kcal/mol	$\Delta H_{S,0}$ @ 0°K kcal/mol	$\Delta H_{S,298}$ @ 298°K kcal/mol	REF.
Ac	1320 ±50	(3.4)	26	(3470) ±300	Ac_1	(95)			26
Ag	1234	2.7 ±.1	27	2436	Ag_1		67.8 ±.2	67.9 ±.2	27
					Ag_2		98		26
Al	933.25	2.58 ±.03	27,28	2793	Al_1	69.5 ±.9	78.1 ±.5	78.7 ±.5	27,28
					Al_2		109		26
Am	1268 ±4	2.9	27	(2880)	Am_1	57		66	26
As	1090	6.62	26	900	As_4			38.54 ±.10	24
					As_4			34.4 ±.4	27,50
					As_2		53.3	53.1	27,50
					As_1		72.0	72.3	27,50
At	(575)	(5.7)	26	(610)	At_2	21.6			26
Au	1336	2.955	26	3080	Au_1		88.0 ±1.0	88.0 ±1.0	26,42
					Au_1			88.3 – 89.7	52
					Au_2		126		26
B	2300 ±50	(5.3)	27	4075	B_1	(121.3) ±4	127.8 – 137.9	129.0 – 139.1	15,27,28
	(2450) ±20	(5.4)	28	(3930)	B_2		195.0 ±6.4		28
Ba	1002 ±2	(2.3)	27	(2400)	Ba_1	40.5 @ 900°K			27
				2063	Ba_1	39.3			10
				2100 ±100	Ba_1			43.9 ±.4	55
Be	1560 ±5	(2.0)	27	2745	Be_1	71.1	76.5 ±1.5	77.5 ±1.5	27,28
Bi	544.52	2.7 ±.1	27	1837	Bi_1		50.2 ±.5	50.1 ±.5	27,30
					Bi_2		53.2 ±1.0	52.6 ±1.0	27,30
					Bi_4			57.6	30A
					Bi_4		59.0 ±3.4		45
					Bi_3		64.1 ±4.3		45
C				4100	C_3		188.1 ±6.0	189.6 ±6.0	27
					C_1		169.98 ±.5	171.29 ±.5	27
					C_2		195.0 ±2.0	197.0 ±2.0	27
					C_4		230 ±6	242 ±6	26
					C_5		233 ±6	242 ±6	26
Ca	1112 ±2	2.04 ±.1	27	1757	Ca_1		42.5 ±.4	42.6 ±.4	27
					Ca_2			79	26

Table II—Melting and Vaporization Data for the Solid and Liquid Elements (2 of 5)

SYMBOL	MELTING			VAPORIZATION					
	MP °K	ΔH_M kcal/mol	REF	BP °K	SPECIES	ΔH_V @ BP kcal/mol	$\Delta H_{S,0}$ @ 0°K kcal/mol	$\Delta H_{S,298}$ @ 298°K kcal/mol	REF.
Cd	594.18	1.48 ±.02	27	1040	Cd_1		26.73 ±.15	26.72 ±.15	27,35
					Cd_2			50.8	26
Ce	1071 ±3	1.305 ±.05	27	3700	Ce_1		101 ±3	101 ±3	27
Co	1768 ±1	3.87 ±.06	27,28	3200	Co_1	89.2	102.0 ±1.0	102.4 ±1.0	27,28
Cr	2130 ±20	(4.0)	27	2945	Cr_1		94.5 ±1.0	95.0 ±1.0	27
Cs	301.55 ±.01	0.499 ±.001	1,28	951.6	Cs_1	16.108	18.68 ±.5	18.32 ±.5	28
					Cs_2		26.45 ±1.0	25.40 ±1.0	
Cu	1356.55 ±.2	3.14 ±.2	27,28	2840	Cu_1	72.7	80.2 ±.3	80.5 ±.3	27,28,44
					Cu_2		116 ±3	116 ±3	28
Dy	1682	2.64 ±.2	27	2835	Dy_1		70.0 ±1.0	69.4 ±1.0	27
Er	1795	4.757	27	3135	Er_1		76.1 ±1.0	75.8 ±1.0	27
Eu	1090	2.202 ±.05	27	1870	Eu_1		42.0 ±.2	41.9 ±.2	27
Fe	1809	3.3 ±.1	27	3135	Fe_1	83.7	98.7 ±.3	99.3 ±.3	27,28
Fr	(300)	(0.5)	26	(950)	Fr_1	(15.2)		16.50	26,38
Ga	302.9	1.336	26	2480	Ga_1		64.0 ±.5	65.0 ±.5	3,34,37
					Ga_2			105	50
Gd	1585 ±2	2.40 ±.1	27	3540	Gd_1		95.3 ±.5	95.0 ±.5	27
					Gd_1			92.1 ±3.2	33
Ge	1210.4	8.83	27	3107	Ge_1		88.8 ±.5	89.5 ±.5	27
					Ge_2			115	26
Hf	2500 ±20	(5.8)	27	4875	Hf_1		147.9 ±1.0	148.0 ±1.0	27
Hg	234.29 ±.02	0.5486 ±.005	25,27,28	629.7	Hg_1	14.133 ±.020	15.404 ±.015	14.652 ±.015	25,27,28
					Hg_2			27.4	26
Ho	1743	(2.9)	27,51	2968	Ho_1		72.3 ±.3	71.9 ±.3	27,51
In	429.3	0.780	27	2343	In_1		57.6 ±1.0	57.5 ±1.0	3,22,27,34
					In_2			94	26
Ir	2727	(6.3)	27	4600	Ir_1		159.8 ±1.0	160.0 ±1.0	27,41
K	336.35	0.550	1,28	1037	K_1	18.30	21.52 ±.20	21.31 ±.20	25,28
					K_2		31.19 ±.5	30.37 ±.5	28

Table II—Melting and Vaporization Data for the Solid and Liquid Elements (3 of 5)

SYMBOL	MELTING: MP °K	MELTING: ΔH_M kcal/mol	MELTING: REF.	VAPORIZATION: BP °K	SPECIES	ΔH_V @ BP kcal/mol	$\Delta H_{S,0}$ @ 0°K kcal/mol	$\Delta H_{S,298}$ @ 298°K kcal/mol	REF.
La	1193 ±1	1.48 ±.05	27	3730	La_1		103.1 ±1.0	103.0 ±1.0	27
Li	453.69	0.7171 ±.0037	1,28	1620	Li_1	35.16	38.03 ±.40	38.41 ±.40	10,25,28
					Li_2		50.3 ±.9	50.4 ±.9	27
Lu	1936	4.6	27	3670	Lu_1		102.2 ±.4	102.2 ±.4	27
Mg	922.0 ±.5	2.14 ±.05	27	1363	Mg_1		34.7 ±.3	35.0 ±.3	27
Mn	1515 ±5	(2.9)	27	2335	Mn_1		67.4 ±1.0	66.7 ±1.0	27,46
Mo	2890	(6.7)	27,28	4885	Mo_1	140.8	156.9 ±.5	157.3 ±.5	27,28
Na	370.98 ±.02	0.622	1,28	1156	Na_1		25.815	25.755	10,28
					Na_2		33.47	32.87	28
Nb	2740	(6.3)	27	5015	Nb_1		171.7 ±1.0	172.4 ±1.0	27
Nd	1289 ±5	1.71 ±.1	27	3340	Nd_1		78.5 ±.5	78.3 ±.5	27
Ni	1726 ±4	4.176	27	3185	Ni_1		102.3 ±.5	102.8 ±.5	27
Np	910 ±2		27	(4175)	Np_1	94 ±6 @ 1800°K			18
Os	3300 ±20	(7.6)	27	5300 ±100	Os_1			189.0 ±1.4	16,40
P (red)	870	4.5 ±.2	26	704	P_4		30.84 ±.5	30.77 ±.5	
					P_2			42.68 ±.5	28
					P_1		79.2 ±.5	79.8 ±.5	
P (white)	317.30 ±.05	0.1574 ±.0005	26	550 ±3	P_4			14.08 ±.2	28
Pb	600.6	1.147	27,28	2023	Pb_1	42.53	46.78 ±.3	46.62 ±.3	9,27,28,29,30
					Pb_2			70	26
Pd	1825	(4.2)	27	3237	Pd_1		89.8 ±.5	90.0 ±.5	27,47
Pm	1353 ±10	(3.0)	20,38	(2730)	Pm_1		(64)	(64)	20
Po	527	(3.0)	26	1220	Po_2			32.9	26
					Po_1			34.5	
Pr	1204 ±4	1.65 ±.1	27	3785	Pr_1		85.3 ±.5	85.0 ±.5	27
Pt	2043	(4.7)	26,30	4065	Pt_1		134.8 ±1.0	135.0 ±1.0	26
Pu	913 ±1	0.68 ±1	27,36	3505	Pu_1		84.2 ±4.0	84.1 ±4.0	27
Ra	973	(2.0)	26	(1800)	Ra_1	32.7		38.7	26,38

Table II—Melting and Vaporization Data for the Solid and Liquid Elements (4 of 5)

SYMBOL	MELTING			VAPORIZATION					
	MP °K	ΔH_M kcal/mol	REF.	BP °K	SPECIES	ΔH_V @ BP kcal/mol	$\Delta H_{S,0}$ @ 0°K kcal/mol	$\Delta H_{S,298}$ @ 298°K kcal/mol	REF.
Rb	312	0.540 ±.02	27	967	Rb_1		19.90 ±.1	19.[illegible] ±.1	27
					Rb_2		28.50 ±.2	28.64 ±.2	
Re	3453 ±20	(7.9)	26	5960	Re_1		185.9 ±2.0	186.1 ±2.0	7,26,43,47
Rh	2239	(5.2)	26	4000 ±100	Rh_1		132.8 ±.5	133.1 ±.5	26,47
Ru	(2700)	(6.2)	26	4350	Ru_1		154.5 ±1.3	154.9 ±1.3	16,40
S	388.36	0.41052 ±.0005	28	717.75	S_8		25.14 ±.15	24.20 ±.15	28
					S_2		30.80 ±.2	30.84 ±.2	
					S_1		66.14 ±.5	66.68 ±.5	
Sb	904 ±1	4.75 ±.15	27	1860	Sb_2		55.70 ±.6	55.26 ±.6	27
					Sb_4		50.57 ±.2	49.36 ±.2	
					Sb_1		63.15 ±.6	63.23 ±.6	
Sc	1812	3.37	27	3105	Sc_1		89.9 ±1.0	90.3 ±1.0	27
Se	490	1.3	26	958	Se_5			40.5 ±1.5	68,6C
		2.30	68		Se_2			34.2 ±.8	6
		1.9 ±.2	54		Se_6			37.6 ±1.5	68,6C
					Se_7			41.5 ±1.5	68,6C
					Se_3			38.4 ±1.5	68,6C
					Se_8			44.5 ±1.5	68,6C
					Se_1		54.11	54.27	50
Si	1685 ±3	12.0 ±1.0	27	3490	Si_1		106.7 ±1.0	107.7 ±1.0	28
					Si_2		140 ±3	141 ±3	
					Si_3		151 ±10	152 ±10	
Sm	1345	2.06 ±.1	27	2064	Sm_1		49.3 ±.5	49.4 ±.5	23,27,33,53
Sn	505	1.67	27	2896	Sn_1		72.2 ±.5	72.2 ±.5	27,39
					Sn_2			98	26
Sr	1043	(2.4)	27	1648	Sr_1	33.7		39.3 ±.5	10,27
Ta	3250	(7.5)	27	5640	Ta_1		186.8 ±.6	186.9 ±.6	27
Tb	1630 ±6	2.58 ±.1	27	3495	Tb_1		93.4 ±.5	92.9 ±.5	27
Tc	2445	(5.5)	26,31	(5150)	Tc_1			158 ±4	31
Te	722.6 ±.3	4.18	26,27	1261	Te_2		40.8 ±.2	40.2 ±.2	5,27
					Te_1		46.9 ±.1	46.9 ±.1	

Table II—Melting and Vaporization Data for the Solid and Liquid Elements (5 of 5)

SYMBOL	MELTING			VAPORIZATION					
	MP °K	ΔH_M kcal/mol	REF	BP °K	SPECIES	ΔH_V @ BP kcal/mol	$\Delta H_{S,0}$ @ 0°K kcal/mol	$\Delta H_{S,298}$ @ 298°K kcal/mol	REF.
Th	2028 ±10	(3.9)	27	5000	Th_1		137.6 ±.5	137.5 ±.5	27
Ti	1933 ±10	(3.7)	27,28	3560	Ti_1		111.6 ±.5	112.3 ±.5	27,28,47
Tl	577	0.975 ±.05	26	1726	Tl_1	42.4	43.00 ±.2	42.85 ±.2	4,10,50
Tm	1818	4.03 ±.05	27	2220	Tm_1		55.8 ±1.0	55.5 ±1.0	27
U	1405 ±2	2.04	27	4405	U_1			126.3 ±1.0	2,27
V	2175 ±15	(5.0)	27	3690	V_1		122.12 ±.25	122.90 ±.25	27
W	3680 ±20	(8.5) ±2.5	27,28	5935	W_1	192.8	203.1 ±1.5	203.4 ±1.5	27,28
Y	1799 ±5	2.72 ±.03	27	3610	Y_1		101.3 ±.5	101.5 ±.5	27,33
Yb	1097	1.83 ±.04	27	1467	Yb_1	33.6	36.5 ±.2	30.3 ±.2	11,27
Zn	692.7 ±.1	1.77 ±.08	26	1184	Zn_1		31.11 ±.05	31.25 ±.05	4,17,26,35
Zr	2125 ±5	(4.0)	27,28	4775	Zr_1	141.1	145.2 ±1.0	145.5 ±1.0	27,28

References

[1] P. Y. Achener, W. V. Mackewicz, D. L. Fisher, and D. C. Camp, "Thermophysical and Heat Transfer Properties of Alkali Metals," Report No. AGN-8195, Vol. I, Nuclear Div. Aerojet-General Corp., San Ramon, Calif., April (1968).

[2] R. J. Ackermann and E. G. Rauh, "Vapor Pressure of Liquid Uranium; Effects of Dissolved Tantalum, Phosphorus, Sulfur, Carbon, and Oxygen," *Jour. Phys. Chem.*, Vol. 73, p. 769, April (1969).

[3] C. B. Alcock, J. B. Cornish, and P. Grieveson, "Knudsen Effusion Studies of Compounds of Uranium and Thorium with Elements of Groups IIIb and IVb," *IAEA Symposium on Thermodynamics with Emphasis on Nuclear Materials and Atomic Transport in Solids*, Vienna, 1965, No. SM-66/34.

[4] A. T. Aldred and J. N. Pratt, "Vapor Pressures of Zinc, Cadmium, Antimony, and Thallium," *Jour. Chem. Eng. Data*, Vol. 8, p. 429, July (1963).

[5] E. H. Baker, "The Boiling Point Relation for Tellurium at Elevated Pressures," *Jour. Chem. Soc.* (A), Vol. 1967, p. 1558, Sept. (1967).

[6] E. H. Baker, "The Vapor Pressure and Resistivity of Selenium at High Temperatures," *Jour. Chem. Soc.* (A), Vol. 1968, p. 1089, May (1968).

[6A] J. Berkowitz and J. R. Marquart, "Equilibrium Composition of Sulfur Vapor," *Jour. Chem. Phys.*, Vol. 39, p. 275, July 15 (1963).

[6B] J. Berkowitz and W. A. Chupka, "Equilibrium Composition of Selenium Vapor; the Thermodynamics of the Vaporization of HgSe, CdSe, and SrSe," *Jour. Chem. Phys.*, Vol. 45, p. 4289, Dec. 1 (1966).

[6C] J. Berkowitz and W. A. Chupka, "Comment on the Composition of Selenium Vapor," *Jour. Chem. Phys.*, Vol. 48, p. 5743, June 15 (1968).

[7] P. E. Blackburn, "The Vapor Pressure of Rhenium," *Jour. Phys. Chem.*, Vol. 70, p. 311, Jan. (1966).

[8] A. J. H. Boerboom, H. W. Reyn, and J. Kistemaker, "Heat of Sublimation and Vapor Pressure of Strontium," *Physica*, Vol. 30, p. 254, (1964).

[9] J. Bohdansky and H. E. J. Schins, "New Method for Vapor-Pressure Measurements at High Temperature and High Pressure," *Jour. Applied Phys.*, Vol. 36, p. 3683, Nov. (1965).

[10] J. Bohdansky and H. E. J. Schins, "Vapor Pressure of Different Metals in the Pressure Range of 50 to 4000 torr," *Jour. Phys. Chem.*, Vol. 71, p. 215, Jan. 16 (1967).

[11] J. Bohdansky and H. E. J. Schins, "The Vapor Pressure of Ytterbium in the Pressure Range of 40-4000 torr," *Jour. Less Common Metals*, Vol. 13, p. 248 (1967).

[12] C. F. Bonilla and G. Shulman, "Selenium: Possible Rankine-Cycle Fluid," *Nucleonics*, Vol. 22, p. 58, March (1964).

[13] K. J. Bowles, "Vapor Pressure of Potassium to 2170°K," NASA Technical Note D-4535, May (1968).

[14] L. Brewer, private communication, (1968).

[15] R. P. Burns, A. J. Jason, and M. G. Inghram, "Evaporation Coefficient of Boron," *Jour. Chem. Phys.*, Vol. 46, p. 394, Jan. 1 (1967).

[16] N. J. Carrera, R. F. Walker, and E. R. Plante, "Vapor Pressures of Ruthenium and Osmium," *Jour. Res. NBS*, Vol. 68A, p. 325, May-June (1964).

[17] H. Cordes and H. Cammenga, "Vapor Pressure and Enthalpy of Sublimation of Zinc," *Z. Phys. Chemie*, Vol. 45, p. 196, May (1965).

[17A] J. Drowart, A. Pattoret, and S. Smoes, "Concerning the Influence of Oxygen on the Vapor Pressure of Uranium," *Jour. Chem. Phys.*, Vol. 42, p. 2629, April 1 (1965).

[18] H. A. Eick and R. N. R. Mulford, "Vapor Pressure of Neptunium," *Jour. Chem. Phys.*, Vol. 41, p. 1475, Sept. (1964).

[19] R. C. Feber, "Heats of Dissociation of Gaseous Halides," Report No. LA-3164, Los Alamos Scientific Lab., University of Calif., Los Alamos, N. M., May 24 (1965).

[19A] H. Fujisaki, J. B. Westmore, and A. W. Tickner, "Mass Spectrometric Study of Subliming Selenium," *Can. Jour. Chem.*, Vol. 44, p. 3063 (1966).

[20] K. A. Gschneidner, Jr., "The Application of Vacuum Metallurgy in the Purification of Rare-Earth Metals," *Trans. Vacuum Metallurgy Conference*, 1965 (L. M. Bianchi, Ed.), Am. Vac. Soc., Boston, Mass. (1966).

[21] C. E. Habermann and A. H. Daane, "Vapor Pressures of the Rare Earth Metals," *Jour. Chem. Phys.*, Vol. 41, p. 2818, Nov. (1964).

[22] C. C. Herrick, "Vapor Pressure of Liquid Indium," *Trans. Met. Soc. AIME*, Vol. 230, p. 1439, Oct. (1964).

[23] C. C. Herrick, "The Vapor Pressure and Heat of Sublimation of Samarium," *Jour. Less Common Metals*, Vol. 7, p. 330, (1964).

[24] C. C. Herrick and R. C. Feber, "Vaporization Studies on Arsenic," *Jour. Phys. Chem.*, Vol. 72, p. 1102, April (1968).

[25] W. T. Hicks, "Evaluation of Vapor-Pressure Data for Mercury, Lithium, Sodium, and Potassium," *Jour. Chem. Phys.*, Vol. 38, p. 1873, Apr. (1963).

[26] R. E. Honig, "Vapor Pressure Data for the Solid and Liquid Elements," *RCA Review*, Vol. XXIII, p. 567, Dec. (1962).

[27] R. R. Hultgren et al, "Selected Values for the Thermodynamic Properties of Metals and Alloys," Report of the Minerals Research Laboratory, University of California, Berkeley, Calif. (1962-1968).

[28] JANAF Thermochemical Tables, The Dow Chemical Company, Midland, Mich. (1962-1968).

[29] J. H. Kim and A. Cosgarea, Jr., "Study of the Vapors of Liquid Lead and Bismuth," *Jour. Chem. Phys.*, Vol. 44, p. 806, Jan. (1966).

[30] A. D. Kirshenbaum and J. A. Cahill, "The Direct Determination of the Boiling Point of Tin," *Jour. Inorg. Nucl. Chem.*, Vol. 25, p. 232, March (1963).

[30A] Fred J. Kohl, O. Manuel Uy, and K. Douglas Carlson, "Cross Sections for Electron Impact Fragmentation and Dissociation Energies of the Dimer and Tetramer of Bismuth," *Jour. Chem. Phys.*, Vol. 47, p. 2667, 15 Oct. (1967).

[31] O. H. Krikorian, J. H. Carpenter, and R. S. Newbury, "A Mass Spectrometric Study of the Enthalpy of Sublimation of Technetium," UCRL-71573 (Feb. 1969); *Jour. High Temp. Sci.* (to be published).

[32] A. A. Kudryatsev and G. P. Ustyugov, "Determination of the Pressure of the Saturated Vapors of Selenium and Tellurium," *Tr. Mosk. Khim.-Tekhnol. Inst.*, Vol. 38, p. 42, (1962).

[33] C. E. Lundin and A. S. Yamamoto, "A Fundamental Investigation of the Alloying Behavior of the Rare Earths and Related Metals," University of Denver, Denver Research Institute Report No. DRI-2437, Sept. (1967).

[34] G. J. Macur, R. K. Edwards, and P. G. Wahlbeck, "Multiple Knudsen Cell Effusion. Enthalpies of Vaporization of Indium and Gallium," *Jour. Phys. Chem.*, Vol. 70, p. 2956, Sept. (1966).

[35] J. R. McCreary and R. J. Thorn, "Enthalpy and Entropy of Sublimation of Zinc and Cadmium; Comparison of Torsional and Effusional Vapor Pressures," *Jour. Chem. Phys.* (to be published).

[36] R. N. R. Mulford, "The Vapor Pressure of Plutonium," in *Thermodynamics*, Vol. I, p. 231, International Atomic Energy Agency, Vienna (1966).

[37] Z. A. Munir and A. W. Searcy, "Torsion Effusion Study of the Vapor Pressure and Heat of Sublimation of Gallium," *Jour. Electrochem. Soc.*, Vol. 111, p. 1170, Oct. (1964).

[38] A. N. Nesmeyanov, *Vapor Pressure of the Chemical Elements*, R. Gary, Ed., Elsevier Publ. Co., Amsterdam and New York, (1963).

[39] M. Onillon and M. Olette, "Determination of the Vapor Pressure of Tin by a Vacuum Evaporation Method," *C. R. Acad. Sci. Paris C*, Vol 266, p. 517, Feb. 19 (1968).

[40] M. B. Panish and L. Reif, "Vaporization of Ruthenium and Osmium," *Jour. Chem. Phys.*, Vol. 37, p. 128, July (1962).

[41] R. C. Paule and J. L. Margrave, "Vapor Pressures of Platinum Metals, III. Iridium and Ruthenium," *Jour. Phys. Chem.*, Vol. 67, p. 1896, Sept. (1963).

[42] B. A. Phillips and M. H. Rand, "A Transpiration Apparatus for Measuring Vapor Pressures; The Vapor Pressure of Gold," AERE-R5352, Chemistry Div., Atomic Energy Research Establishment, Harwell, Berkshire, England, Feb. (1967).

[43] E. R. Plante and R. Szwarc, "Vapor Pressure and Heat of Sublimation of Rhenium," *Jour. Res. NBS*, Vol. 70A, p. 175, March-April (1966).

[44] A. Ponslet and D. Bariaux, "Evaporation Rate and Vapor Pressure of Copper," *Bull. Acad. Roy. Belgique, Cl. Sci.*, Vol. 52, p. 248, Feb. (1966).

[45] G. M. Rosenblatt, private communication, (1968).

[45A] L. Rovner, A. Drowart, and J. Drowart, "Mass Spectrometric Determination of Dissociation Energies of Molecules Bi_2, Bi_3, Bi_4, and BiPb," *Trans. Faraday Soc.*, Vol. 63, p. 2906, (1967).

[46] P. J. Spencer and J. N. Pratt, "A Study of the Vapor Pressure of Manganese Using a New High-Temperature Torsion-Effusion Apparatus," *Brit. Jour. Appl. Phys.*, Vol. 18, p. 1473, Sept. (1967).

[47] H. Strassmair and D. Stark, "Rate of Vaporization, Vapor Pressure, and Heat of Sublimation for Rhenium, Rhodium, Palladium, and Titanium." *Z. Angew. Phys.*, Vol. 23, p. 40, June (1967).

[48] Yu. K. Vinogradov and L. D. Volyak, "Experimental Determination of the Pressure of Sodium and Potassium Saturated Vapor," *Teplofiz. Vysokikh Temperatur*, Akad. Nauk SSSR, Vol. 4(1), p. 50, (1966).

[49] G. F. Voronin, A. M. Evseev, and V. L. Goryacheva, "Determination of the Thermodynamic Properties and Molecular Composition of Vapors by the Effusion Method. VI. Thermodynamic Properties of Bismuth Vapor," *Russ. Jour. Phys. Chem.*, Vol. 41, p. 1637, Dec. (1967).

[50] D. D. Wagman, W. H. Evans, V. B. Parker, I. Halow, S. M. Bailey, and R. M. Schumm. "Selected Values of Chemical Thermodynamic Properties," NBS Technical Note 270-3, Jan. (1968).

[51] G. F. Wakefield, A. H. Daane, and F. H. Spedding, "Vapor Pressure of Holmium," *Jour. Chem. Phys.*, Vol. 47, p. 4994, Dec. (1967).

[52] J. W. Ward, "Study of Some of the Parameters Affecting Knudsen Effusion. III. The Vapor Pressure of Gold," *Jour. Chem. Phys.*, Vol. 47, p. 4030, Nov. (1967).

[53] A. S. Yamamoto, C. E. Lundin, and J. F. Nachman, "Vapor Pressures of Samarium and Gadolinium," *Proceedings of the Fourth Conference on Rare Earth Research* (LeRoy Eyring, Ed.), Gordon and Breach, New York (1964).

[54] R. Yamdagni and R. F. Porter, "Mass Spectrometric and Torsion Effusion Studies of the Evaporation of Liquid Selenium," *Jour. Electrochem. Soc.*, Vol. 115, p. 601, June (1968).

[55] P. D. Zavitsanos, "The Vapor Pressure of Barium," G. E. Technical Report 68SD331 (Nov. 1968).

THE EFFECT OF BARRIER RECOMBINATION ON PRODUCTION OF HOT ELECTRONS IN A METAL BY FORWARD BIAS INJECTION IN A SCHOTTKY DIODE

By

Richard Williams

RCA Laboratories
Princeton, New Jersey

Introduction

Summary—Devices such as the Schottky barrier cold cathode depend on the efficient production of hot electrons in a metal by forward-bias injection in a metal–semiconductor diode. Under certain conditions, minority carriers are injected from the metal into the semiconductor. These recombine with the electrons in the barrier and lower the efficiency of production of hot electrons. An analysis of this effect has been made on the basis of a simple model. In general, recombination of carriers in the barrier leads to a forward current–voltage relation having the factor $\exp\{eV/(\beta kT)\}$. The present work shows that β is related to the barrier height and to the bandgap of the semiconductor. For the kind of recombination considered here, β can assume values between 1 and 2. Results are illustrated by a sample calculation of a current–voltage curve.

SEVERAL devices have been proposed that are based on the transport through thin metal layers of hot electrons injected from a Schottky barrier. These include the metal-base triode[1] and a cold cathode.[2] We consider the case of injection of electrons into a metal from a high Schottky barrier formed by the metal on an n-type semiconductor. If the barrier height, ϕ, is greater than half of the bandgap energy, E_g, there may be, at the same time, significant injection of holes

[1] A. Rose, U. S. Patent #3,250,967; D. V. Geppert, "A Metal-Base Transistor," *Proc. IRE*, Vol. 50, p. 1527, June 1962; C. R. Crowell and S. M. Sze, "Electron-Optical-Phonon Scattering in the Emitter and Collector Barriers of Semiconductor-Metal-Semiconductor Structures," *Solid-State Electronics*, Vol. 8, p. 979, Dec. 1965.

[2] R. Williams and C. R. Wronski, "Electron Emission from the Schottky Barrier Structure ZnS:Pt:Cs," *Appl. Phys. Letters*, Vol. 13, p. 231, Oct. 1, 1968.

from the metal into the semiconductor. These may recombine with electrons in the barrier region. The recombination current does not produce hot electrons in the metal and is an undesirable source of power dissipation in the above devices. We consider here the quantitative consequences of a simple model for this system.

The current–voltage relation for forward bias in a Schottky barrier diode with no recombination is given,[3] using the approximations of the diffusion theory, by

$$j_{\mathrm{diff}} = j_{o,\mathrm{diff}} \exp\{eV/(kT)\} - 1 \tag{1}$$

where

$$j_o = e\mu E_s N_c \exp\{-e\phi/(kT)\}$$

and

μ = electron mobility,

ϕ = barrier height,

E_s = surface electric field in the semiconductor,

$N_c = 2.5 \times 10^{19}(m^*/m)^{3/2}(T/300°)^{3/2}\mathrm{cm}^{-3}$ = effective density of the states in the conduction band,

e = electron charge,

V = forward bias voltage.

Equation (1) gives the current over the top of the barrier, which gives the desired hot electrons in the metal. We have neglected the current due to injection of holes that do not recombine in the barrier. This current is usually much smaller than the corresponding electron current, and is significant only when $E_g - \phi \leq E_c - E_{fn}$, where E_c is the energy of the conductive level and E_{fn} is the Fermi level energy. When there is a recombination, the current–voltage relation for the recombination current has the form

$$j_{\mathrm{rec}} = j_{o,\mathrm{rec}} \exp\{eV/(\beta kT)\} - 1. \tag{2}$$

It can be seen from Figure 1 that β will have values between 1 and 2. The figure shows the barrier at equilibrium with no applied voltage. Recombination is important[4] only in a narrow zone around the point

---

[3] E. Spenke, *Electronic Semiconductors*, p. 84, McGraw-Hill, New York, 1958.

[4] R. L. Pritchard, *Electrical Characteristics of Transistors*, p. 76, McGraw-Hill, New York, 1967.

where hole and electron concentrations are equal.* Assuming equal densities of states in valence and conduction bands, this zone is where the Fermi level lies in the middle of the energy gap. At this point, the bottom of the conduction band always lies above the Fermi level by the energy $E_g/2$. To reach this point, the electrons have to acquire only a fraction of the energy required to go over the barrier. The fraction is $E_g/(2\phi)$. Furthermore, when voltage, V, is applied to the diode, the fraction $E_g/(2\phi)$ will fall across the region that the electrons must cross to reach the recombination zone. The applied voltage, V, en-

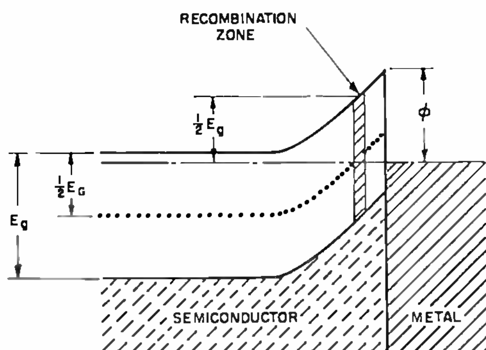

Fig. 1—Metal-semiconductor Schottky barrier showing recombination zone where electron and hole concentrations are equal.

hances the current to the recombination zone, not by the factor exp $\{eV/(kT)\}$, but by the factor exp $\{(e/kT)(E_g/2\phi)V\}$. Thus, β in Equation 2 is given by

$$\beta = 2\phi/E_g . \tag{3}$$

Examination of the figure shows that β will be between 1 and 2. When the metal Fermi level makes contact at the middle of the gap the value is 1 and when it makes contact at the valence band the value is 2. At intermediate points, β lies between 1 and 2. When the metal makes contact above the middle of the gap there is no point within the crystal at which hole and electron concentrations are equal. Under these conditions, recombination is unimportant and β is 1.

The quantity, $j_{o,rec}$, of Equation (2) has the form[4]

$$j_{o,rec} = e[\beta kT/E_s e][N_c \exp\{-e\phi/(\beta kT)\}][1/\tau] \tag{4}$$

* A specific model for recombination is analyzed in the Appendix.

τ is the recombination lifetime, assumed to be the same for both carriers. Equations (1) and (2) have been put into a convenient approximate form by inserting the values $\mu = 100$ cm^2/V-sec, $E_s = 1 \times 10^5 V/$cm, $m^* = m$:

$$j_{\text{diff}} = 4 \times 10^7 \times 10^{-17\phi} \times 10^{17V} \text{amp/cm}^2 \tag{5}$$

$$j_{\text{rec}} = \frac{2 \times 10^{-6}}{\tau} \times 10^{-17\phi/\beta} \times 10^{17V/\beta} \text{amp/cm}^2 \tag{6}$$

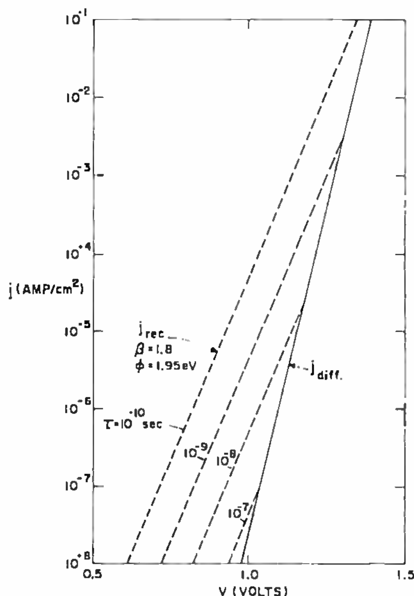

Fig. 2—Comparison of diffusion current and recombination current for the model used for the case $\beta = 1.8$ and $\phi = 1.95$ eV. The recombination current is shown for several values of the lifetime, τ. For GaP $E_g = 2.2$ eV.

The second term in the brackets of Equations (1) and (2) has been dropped.

Figure 2 shows a plot of these equations for the case $\beta = 1.8$ and $\phi = 1.95$ eV (similar values have been found in preliminary studies of GaP:Pt diodes made by C. Wronski[5]). The recombination current has been plotted for several values of τ. If τ is approximately 10^{-9} second in this system, as it is in many p-n junction diodes, then one can expect the diffusion current to dominate for current levels above 10^{-2}A/cm^2.

[5] Private Communications.

This is hopeful for device applications[2] if the model is realistic, since it indicates that the production of hot electrons in the metal can be quite efficient at modest levels of total current.

The special feature of this model is that, for a given material, β depends on the barrier height, as shown by Equation (3). This seems to be borne out by the data reported for barriers of gold on n-type GaP. White and Logan[6] found barriers in the range $\phi = 1.4$ eV to 2.0 eV. Their experimental values of β ranged from 1.4 to 1.6. The values of β according to the present model should range from 1.3 to 1.8, in reasonable agreement with the experiments. Cowley and Hefner[7] found $\phi = 1.30$ eV and values of β ranging from 1.15 to 1.25. For this case, Equation (3) gives $\beta = 1.2$, again in agreement with the experiments. It seems likely that the model will be successful for materials such as GaP that have indirect bandgaps and fairly small carrier lifetimes. It clearly does not apply for barriers on Ge, Si and GaAs[8] where one or both of these conditions does not hold true.

ACKNOWLEDGMENTS

The author is indebted to A. M. Goodman and C. R. Wronski for valuable discussions of this problem.

APPENDIX

To obtain Equation (3), it was assumed that recombination takes place in a narrow zone at that point in the barrier where the thermal equilibrium concentrations of holes and electrons are equal. In addition, it was assumed that the recombination rate can be described by a lifetime. It is shown here that a simple model for recombination through discrete centers in the forbidden zone gives these properties to a sufficiently close approximation.

The model is one of discrete centers in the forbidden zone that capture electrons and then holes. The net result is recombination. There is no restriction on the energy of the centers, except that it must be far enough from the band edges so that recombination takes place before the trapped carrier is re-emitted into the conduction band or the valence band. At room temperature this means, in practice, that

---

[6] H. G. White and R. A. Logan, "GaP Surface-Barrier Diodes," *Jour. Appl. Phys.*, Vol. 34, p. 1990, July 1963.

[7] M. Cowley and H. Heffner, "Gallium Phosphide-Gold Surface Barrier," *Jour. Appl. Phys.*, Vol. 35, p. 255, Jan. 1964.

[8] C. R. Crowell, J. C. Sarace, and S. M. Sze, "Tungsten-Semiconductor Shottky-Barrier Diodes," *Trans. Met. Soc. AIME*, Vol. 233, p. 478, March 1965.

the depth must be at least 0.2 eV from the edge of the nearest band. For simplicity a set of centers, all having the same energy, will be discussed, but the results obtained apply equally to a set of centers distributed over a range of energies.

Consider centers near the middle of the forbidden zone. These may be represented by the dots in Figure 1. Suppose that the center is electrically neutral when empty and negatively charged when occupied by an electron. Under a forward bias larger than a few times kT/e, the concentrations of electrons and holes in the barrier will depart substantially from their thermal equilibrium values, and the occupation of the centers by holes and electrons will be determined by recombination kinetics rather than thermal equilibrium considerations. The problem of recombination under these conditions has been analyzed by Rose[9], and his ideas and notation will be used here. It can be seen qualitatively that the occupation of the centers will be different in different parts of the barrier region. At the right, near the metal, there are few electrons and many holes, so the centers will be almost empty of electrons. At the left, near the inner edge of the barrier, the centers will be almost entirely filled with electrons.

The concentrations of free carriers, n and p, vary greatly with position in the barrier. Similarly, the number of recombination centers filled with electrons, n_r, and the number of empty recombination centers, p_r, vary with position. The total number, N, of recombination centers, empty plus full, is independent of position, as are the capture cross sections of empty centers for electrons, S_n, and of full centers for holes. The hole and electron lifetimes, τ_n and τ_p are also functions of position. In the steady state, at any given position, the number of holes recombining per unit time is equal to the number of electrons recombining per unit time:

$$\frac{n}{\tau_n} = \frac{p}{\tau_p}. \tag{7}$$

It is understood that all quantities are functions of position and that the equation must hold for any given position. In general, $\tau_n = 1/(vp_rS_n)$ and $\tau_p = 1/(vn_r/S_p)$, where we have assumed that the thermal velocities, v, are the same for holes and electrons. This, together with the relation, $n_r + p_r = N$, gives

$$np_rS_n = pn_rS_p \tag{8}$$

[9] A. Rose, *Concepts in Photoconductivity and Allied Problems*, pp. 13-16 and 118-128, Interscience Publishers, New York, 1963.

and

$$n_r = \frac{N}{1 + \dfrac{pS_p}{nS_n}}, \quad p_r = \frac{N}{1 + \dfrac{nS_n}{pS_p}}. \tag{9}$$

Consider the quantity n_r as a function of position within the barrier (Figure 1). Wherever $pS_p \ll nS_n$, nearly all centers are occupied by electrons and the occupation is nearly independent of position. In this region, the recombination rate varies with position in the same way as does the hole concentration (right hand term of Equation 9.) As one moves from left to right within the left side of the barrier the recombination rate increases continuously until the point is reached where n_r begins to decrease. A similar examination of the right-hand side of the barrier shows that p_r is constant in this region and that the rate of recombination increases continuously as one moves toward the left until the point is reached where p_r begins to decrease. The maximum rate of recombination is at the point where $pS_p/(nS_n) = 1$. Our original assumption was that the maximum recombination rate is at that part of the zone where $p = n$ at equilibrium. The factor S_p/S_n is likely to be about 100. In the particular case we have discussed, S_n for capture of an electron by a neutral center is[9] typically of order 10^{-15} cm^2, while S_p for capture of a hole by a negatively charged center is typically of order 10^{-13} cm^2. Alternatively, for the case where the center filled by an electron is neutral, S_n will be greater than S_p by a factor of about 100. In either case the energy, $E_g/2$, of Equation (3) must be replaced by an energy larger or smaller by about 0.06 eV. Since we are interested mainly in high-bandgap materials, with E_g around 2 eV, there is no serious error introduced by neglecting this contribution due to difference in capture cross sections. The model involving recombination through deep centers, then, has the general properties that have been assumed.

There is another property of this system that causes small deviations from the assumed behavior. When $\beta = 2$, the applied voltage increases the concentrations of holes and electrons by the same factor. For cases where β is between 1 and 2, the zone of maximum recombination is nearer to the metal–semiconductor interface. As a result, any increment of applied voltage increases the concentration of electrons more than that of holes. The zone of maximum recombination moves continuously to the right as the current level increases, and there is a corresponding decrease in β. Analysis of this effect shows that the

value $\beta(V)$ of β for applied voltage V is related to the value $\beta(0)$, for low applied voltages, by

$$\beta(V) = \beta(0) \frac{1}{1 + \left(1 - \frac{\beta(0)}{2}\right) \frac{V}{\phi}}. \tag{10}$$

For the data shown in Figure 2, this correction changes β from 1.8 at low current levels to 1.7 at the highest current levels. A correction of this magnitude lies within the experimental scatter of the data that have been reported and is not included in the plot. (It should be noted that in the extreme case, this effect reduces β to 1, and at higher current levels, the equation no longer holds.)

CURRENT-VOLTAGE CHARACTERISTICS OF SILVER-n-TYPE GaP SCHOTTKY BARRIERS

BY

C. R. WRONSKI

RCA Laboratories
Princeton, New Jersey

Summary—Schottky barriers of silver on n-type GaP were prepared and the forward bias current characteristics investigated. Current-voltage relationships $j \propto \exp\{eV/(\beta kT)\}$ were obtained where $\beta = 1.5$ to 2 at low forward bias, and $\beta \simeq .1$ at sufficiently high forward bias. The currents in the second region were in good agreement with diffusion currents corresponding to barrier heights determined by differential-capacitance measurements. The current characteristics can be explained by the electron currents flowing over the top of the barrier and becoming dominant and much larger than electron-hole recombination currents in the barrier. Hole-electron lifetimes of the order 10^{-10} second were indicated in the barrier regions of the GaP used.

INTRODUCTION

FOR AN EFFICIENT Schottky-barrier cold cathode,[1,2] it is necessary to have a semiconductor-metal barrier greater than the metal-vacuum work function of the activated metal layer (~1.5 eV). An efficient diode is one in which the majority of electrons go over the top of the barrier rather than through the barrier by recombination. Usually the injection efficiency of the forward current into the metal in such a barrier is represented by a factor β, where the current $j \propto \exp\{eV/(\beta kT)\}$, where e is the electronic charge, V is the forward bias, k is Boltzmann's constant, and T is temperature in degrees Kelvin. A value of β close to unity means that nearly all the electrons go over the barrier, a condition that is essential for an efficient Schottky-barrier cold cathode.

---

[1] R. Williams and C. R. Wronski, *Appl. Phys. Letters*, Oct. 1, 1968.

[2] R. Williams, "The Effect of Barrier Recombination on Production of Hot Electrons in a Metal by Forward Bias Injection in a Schottky Diode," *RCA Review*, Vol. 30, p. 306, June 1969.

Although metal n-type GaP Schottky barriers of approximately 1.5 eV or greater and values of $\beta > 1.4$ have been reported,[3,4] no regions of $\beta \simeq 1$ have been observed and no detailed investigation carried out. Values of $\beta \simeq 1$ have been reported for lower barrier heights on n-type GaP.[4] The current–voltage characteristics of silver-n-type GaP Schottky barriers greater than 1.5 eV are described here. Their forward-bias currents showed regions where the current $j \propto \exp\{eV/(\beta kT)\}$ with $\beta = 1.5$ to 2, and a region where $\beta \simeq 1$. The first region is in agreement with the electron–hole recombination model of Williams[2] and the second region is in good agreement with diffusion currents corresponding to barrier heights as determined by differential-capacitance measurements. This indicates the importance of the effect of recombination centers in the barrier region on the efficiency of hot electron injection into the metal and makes possible an estimate of hole–electron lifetime.

Sample Preparation

Vapor-grown n-type crystals of GaP approximately 10 × 5 × 0.5 mm were used in these experiments. The GaP was grown on the (100) crystal face of n-type GaAs (<1 ohm-cm), which served as a good injecting contact. Ohmic contacts were made to the GaAs either by evaporating a film of AuSn with the crystal at 500°C or by melting indium dots into the crystal at 300°C in a hydrogen atmosphere. The GaP (100) face was polished in a bromine–methanol solution with alumina abrasive and then etched in warm H_2SO_4:HNO_3:HF (30:60:10), with a few drops of bromine, for several minutes. The crystals were then thoroughly washed in acetone and mounted in a vac-ion system, where a series of 10^{-3} cm^2 silver dots approximately 5000 Å thick were evaporated onto the GaP (100) face through thin metal foil masks. The evaporation was carried out at a residual pressure of $\sim 10^{-8}$ Torr at the rate of 40-50 Å/sec. After the diode preparation, contact was made to the silver with a platinum probe and to the ohmic contact on GaAs with copper wire. The crystals were mounted in a holder that was evacuated to $<10^{-3}$ Torr during the measurements. The experimental configuration is shown schematically in Figure 1. The barrier heights and current–voltage characteristics were then determined.

---

[3] H. G. White and R. A. Logan, "GaP Surface-Barrier Diodes," *Jour. Appl. Phys.*, Vol. 34, p. 1990, July 1963.

[4] A. M. Cowley, "Depletion Capacitance and Diffusion Potential of Gallium Phosphide Schottky-Barrier Diodes," *Jour. Appl. Phys.*, Vol. 37, p. 3024, July 1966.

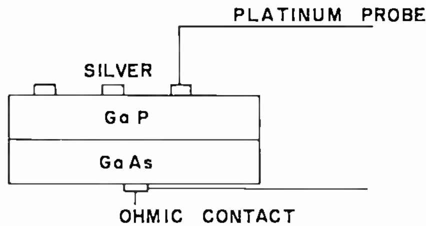

Fig. 1—Schematic representation of the configuration used in the experiments.

Experiments

A. Current–Voltage Measurements

The forward and reverse currents of the diodes were measured by applying voltages and measuring the current with an electrometer whose output was connected to an x-y recorder. Several forward-bias equilibrium current density characteristics are shown in Figures 2 and 3. The reverse-current characteristics were less reproducible than forward-bias ones and were considered to be leakage currents as encoun-

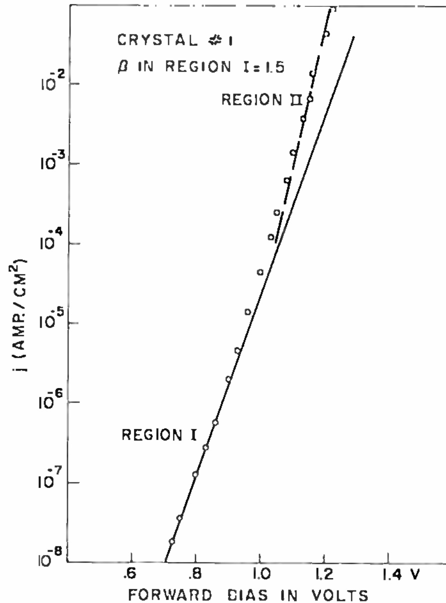

Fig. 2—Current as a function of forward-bias voltage for a diode on Crystal #1.

tered by White and Logan.[3] Typically, the reverse currents were of the order of 10^{-11} ampere (10^{-8}A/cm^{-2}) at 1 volt reverse bias.

Figures 2 and 3 show semilogarthmic plots of current density versus voltage V. The two linear regions I and II correspond to current–voltage relationships $j \propto \exp\{eV/(\beta kT)\}$ where β is a constant. The line in region II is obtained by subtracting the extrapolated values of Region I in the transition region.

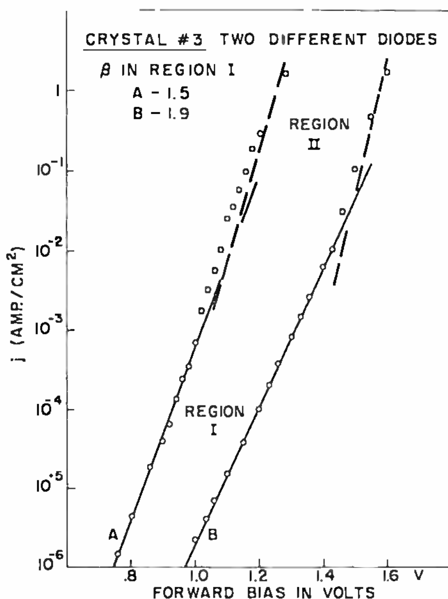

Fig. 3—Current as function of forward-bias voltage for two different diodes on Crystal #3.

B. Differential Capacitance Measurements

The differential capacitance, C, of the diodes was determined as a function of bias voltage on a capacitance bridge with an oscillator frequency of 100 kHz. Bias was supplied externally and the ac signal used across the junction was less than 20 mV. Several measurements were made at a frequency of 1 kHz, and the results were found to be the same as at the higher frequency.

Figures 4 and 5 are plots of $1/C^2$ versus bias voltage V for the diodes whose current characteristics are shown in Figures 2 and 3.

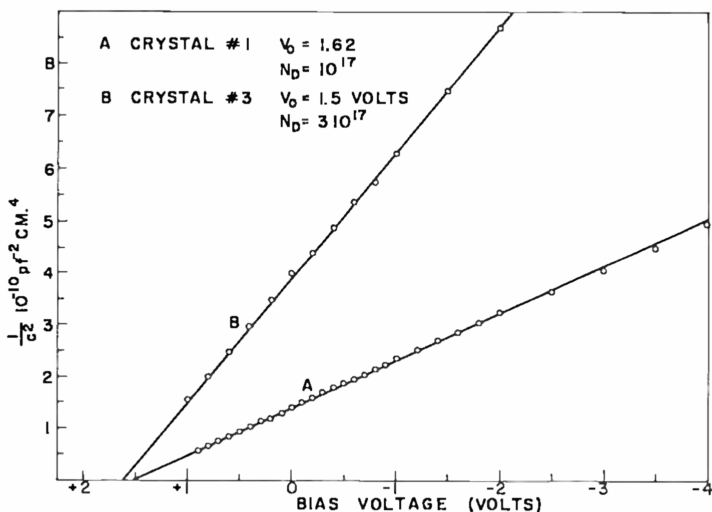

Fig. 4—$1/C^2$ versus V for diodes on Crystals #1 and 3 [currents versus voltage shown in Figures 2 and 3].

The intercept on the voltage axis, V_o, and the slopes of the lines can be used to determine the barrier height, provided there is no excessive intermediate layer between the GaP and the metal.

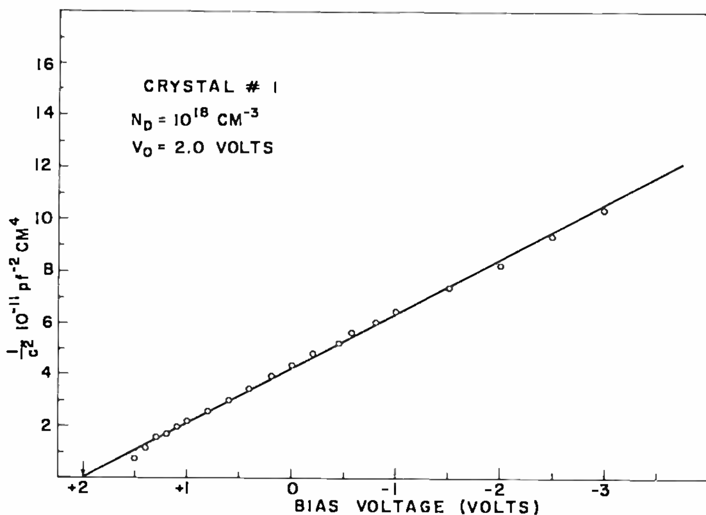

Fig. 5—$1/C^2$ versus V for diode on Crystal #3 [current versus voltage shown in Figure 3].

Results

Capacitance measurements on various crystals gave values of V_0 between 1.5 and 2.0 volts, and of ionized donor concentrations, N_d, from 6×10^{16} to 10^{18} cm^{-3}. Different values of V_0 and N_d could be obtained on different regions of the same crystal. This was also reported in References (3) and (4) and was attributed to inhomogeneities in the crystal and dependence of barrier height on surface states. The barrier heights, as determined by the capacitance method, were taken to be[5]

$$\phi_c = V_0 + \zeta\,, \tag{1}$$

where ζ = distance of the Fermi level from the conduction band and is given by $N_d = N_c \exp\{-e\zeta/(kT)\}$,

N_c = effective density of states in the conduction band, $N_c = 2.5 \times 10^{19}(m^*/m)^{3/2}(T/300)^{3/2}$

m^* = effective mass of electrons in conduction band[6] = 0.4 m.

The experimental values of β in region I of the current–voltage characteristics were from 1.5 to 2.0. The current densities at the cross-over region where $\beta \simeq 1$ were from 10^{-3} to 10^{-1}A/cm^{-2} depending on the barrier height. The barrier height could be estimated if region II in the current–voltage characteristics was assumed to be due to diffusion currents given by[7]

$$j = e\mu E_s N_c \exp\{-\frac{e}{kT}(\phi_j - V)\}$$

where

μ = mobility of electrons.

ϕ_j = value of barrier height determined from I-V data,

E_s = surface field in barrier $= 4.8 \times 10^{-4} N_d^{1/2}(\phi_j - \zeta)^{1/2}$ for GaP.

Values of N_d were obtained from the capacitance measurements, and the values of the barrier height, which is independent of V_0, could be

[5] A. M. Goodman, "Evaporated Metallic Contacts to Conducting Cadmium Sulfide Single Crystals," *Jour. Appl. Phys.*, Vol. 35, p. 573, Mar. 1964.

[6] O. Madelung, *Physics of III-V Compounds*, John Wiley and Sons, New York, N. Y. (1964).

[7] E. Spenke, *Electronic Semiconductors*, McGraw Hill Book Co., New York, N. Y. (1958).

obtained by fitting Equation (2) to Region II of the current–voltage curves. Good agreement between ϕ_j and ϕ_c was obtained, indicating that the diffusion potentials are within ~0.05 volt of V_o. This indicates that interfacial layers[4] are not important here.

The currents in Region I can be explained by the recombination model discussed by Williams.[2] As the forward bias is increased, the hole–electron recombination current observed initially is superseded by the diffusion current, the transition current level depending on the lifetime of the carriers and the barrier height. From the analysis,[2] Region I is represented, to a good approximation, by

Table I

Crystal	V_o	N_D (cm^{-3})	ϕ_c (eV)	$j_{cross\text{-}over}$	ϕ_j (eV)	β_{exp}	β_{cal}	τ (sec)
#1	1.62	10^{17}	1.71	10^{-3}	1.7	1.5	1.54	8×10^{-11}
#2	1.65	6×10^{16}	1.76	10^{-2}	1.75	1.6	1.56	9×10^{-11}
#3	1.5	3×10^{17}	1.57	10^{-3}	1.55	1.5	1.42	2×10^{-11}
	2.0	10^{18}	2.04	10^{-1}	2.0	1.9	1.84	3×10^{-11}
	2.0	6×10^{17}	2.05	10^{-1}	2.0	2.0	1.84	5×10^{-11}
	1.6	5×10^{17}	1.65	10^{-3}	1.65	2.0	1.48	—

$$\beta = \frac{2\phi}{E_g} \tag{3}$$

where E_g is the bandgap of GaP (2.24 eV[6]), ϕ is the barrier height, and

$$j = \frac{1}{\tau}\left(\beta\frac{kT}{E_g}\right) N_c \exp\left\{-\frac{e\phi}{\beta kT}\right\} \exp\left\{\frac{ev}{\beta kT} - 1\right\}, \tag{4}$$

where τ is the recombination lifetime in the barrier. The values of β obtained using Equation (3) were in general agreement with the observed values for the different barrier heights. The lifetimes, τ, obtained using Equation (4) were 10^{-11} to 10^{-10} second. The results are shown in Table I.

Discussion

The barrier heights measured by the capacitance method and those determined from the current–voltage measurements were in good agreement. (No photoemission measurements were carried out on the diodes because of the geometry and the GaAs substrate.)

This indicates that if there was an intermediate layer between the GaP and the metal,[4] it was sufficiently thin to allow the tunneling of electrons. Widely different analyses have been considered[8,9] and yield values of $\beta > 1$, but these did not predict a reasonably sharp transition from the larger values to those close to unity. However, from the good fit of Equations (3) and (4) to the experimental results, it can be inferred that there is significant recombination in GaP–metal Schottky barriers greater than half the bandgap of GaP[2], and that, under forward bias, this results in recombination currents. The magnitude of this current depends on the barrier height, the recombination centers, their capture cross section, and possibly the presence of a thin intermediate layer between the GaP and the metal. This layer could enhance the surface field of the barrier at a given bias so that injection of holes from the metal into the barrier is increased. Increased injection of holes would result in an increase in the recombination current and in values of β different from the case considered in Reference (2). However, where β is in agreement with the theoretical values, an effective recombination lifetime in the barrier can be determined. The values of $\tau \sim 10^{-10}$ second compare well with observed values for hole–electron recombination lifetimes in GaP p-n junctions. An order of magnitude estimate of the recombination center concentration in the barrier can be made[10] if a capture cross section for the centers is assumed. If the centers filled by an electron are neutral, their cross section for capture of an electron is approximately 10^{-13} cm^2. A concentration of empty recombination centers of approximately 10^{16} cm^{-3} would then give electron lifetimes of approximately 10^{-10} second.

ACKNOWLEDGMENTS

The author is indebted to R. Williams and C. J. Nuese for valuable discussion of this problem and to D. Richman for the GaP crystals.

[8] C. R. Crowell and S. M. She, "Current Transport in Metal–Semiconductor Barriers," *Solid-State Electron.*, Vol. 9, p. 1035, Nov.-Dec. 1966.

[9] V. A. Johnson, R. N. Smith, and H. J. Yearian, "D.C. Characteristics of Silicon and Germanium Point-Contact Crystal Rectifiers," *Jour. Appl. Phys.*, Vol. 21, p. 283, 1950.

[10] A. Rose, *Concepts in Photoconductivity and Allied Problems*, Interscience Publishers, New York, N. Y. (1963).

DOUBLE INJECTION ELECTROLUMINESCENCE IN ANTHRACENE

By
J. Dresner

RCA Laboratories
Princeton, N. J.

Summary—Electroluminescent diodes have been constructed on monocrystalline anthracene using solid contacts. The emitted light peaks at 4300 Å and is generated with an external quantum efficiency ranging from 1 to 8% at room temperature. The diodes appear to have stable characteristics under operation at current levels as high as 10^{-1} A/cm^2, and to have a long shelf life. The magnitude of the injected current is controlled by field-assisted emission from the contacts in the high-current mode. In these cells, which are more than 30 microns thick, the operating voltage is greater than 300 volts.

In order to obtain cells operating at or below 50 volts, which is necestary to ensure compatibility with transistorized circuitry, a thickness of 2 to 4 microns is needed. This could not be obtained from single-crystal wafers. Preliminary experiments with melted and recrystallized anthracene layers show that such thin cells can be made. The principal problem, that of pinholes, does not appear to be unsolvable.

Introduction

THE FIRST reported observation of electroluminescence in anthracene that could be unambiguously ascribed to recombination of electrons and holes following double injection was made by Helfrich and Schneider in 1965.[1] Further work with electrolyte contacts followed, and these are now fairly well understood.[2,3] The kinetics of light emission following double injection has also been investigated by Helfrich and Schneider.[4] The electrolytes used in the above work are

[1] W. Helfrich and W. G. Schneider, "Recombination Radiation in Anthracene Crystals," *Phys. Rev. Letters*, Vol. 14, p. 229, 15 Feb. 1965.

[2] W. Mehl and W. Bucher, "Durch elektrochemische Doppelinjektion angeregte Elektrolumineszenz in Anthracen-Kristallen," *Z. Physikalische Chem.*, Vol. 47, p. 76, Oct. 1965.

[3] W. Mehl and J. M. Hale, *Advances in Electrochem. & Electrochem. Engrg.*, Vol. VI, p. 399, P. Delahay, Ed., Interscience, New York, 1967.

[4] W. Helfrich and W. G. Schneider, "Transients of Volume-Controlled Current and of Recombination Radiation in Anthracene," *Jour. Chem. Phys.*, Vol. 44, p. 2902, 15 April, 1966.

generally unstable or corrosive, containing solvents such as tetrahydrofuran, nitromethane, or concentrated H_2SO_4. Those that are most stable tend to be limited in use to rather low current densities, $j < 10^{-5}$ A/cm^2.

Nevertheless, the high theoretical quantum efficiency for light emission, 0.35 quantum/electron, and the blue-violet emission make anthracene an attractive material for the construction of electroluminescent diodes. The present work was directed toward making such cells using stable solid contacts.

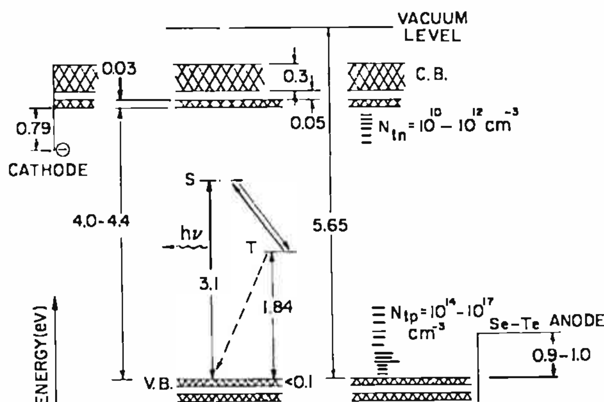

Fig. 1—Energy level structure of the anthracene crystal. The cross-hatched bands belong to the crystal; the energy levels of the molecule are those that participate in the light-emission process. N_{tn} and N_{tp} refer to the total number of electron and hole traps, whose energy distributions decrease exponentially with distance from the band edges. At the left, the potential step for an alkali metal cathode is shown; at the right that for a Se-Te anode.

General Description of the Physical Processes

We begin with a description of the processes of luminescence and double injection in anthracene. Figure 1 shows the energy-level scheme of the system. The cross-hatched bands are those belonging to the anthracene *crystal*, according to the most recent data available.[5,6] Note the narrow lowest conduction band and highest valence band. At the left is shown the potential barrier at the cathode (0.79 eV). This contact consists of negatively charged anthracene ions formed by reaction with an alkali metal (see the next section). At the right is shown

[5] R. Williams and J. Dresner, "Photoemission of Holes from Metals into Anthracene," *Jour. Chem. Phys.*, Vol. 46, p. 2133, 15 March 1967.

[6] J. Dresner, "Conduction-Band Structure in Anthracene Determined by Photoemission," *Phys. Rev. Letters*, Vol. 21, p. 356, 5 Aug. 1968.

the most commonly used anode, an Se-Te alloy with a potential barrier of 0.9 – 1.0 eV. The magnitudes of these barriers were determined from the threshold of photoemission from the contact into the crystal. While there is probably some band bending in the vicinity of the contacts, its magnitude could not be determined. However, it is not expected to play a role in these experiments. Also shown in Figure 1 are the densities of hole and electron traps, N_{tp} and N_{tn}, known to exist in crystals of the quality used. Both are distributed exponentially in energy, with maximum concentration at the band edges.

The injected electrons and holes move in the band system of the crystal. The energy of the pair can be transferred to an anthracene molecule. The most important energy levels through which recombination occurs are shown in the diagram; in particular the desired emission is that originating in the first excited singlet state S (3.1 eV). Also note the forbidden transition from the lowest excited triplet state T to the ground state and the intersystem crossing between the excited S and T states. The diagram is simplified and applies strictly only to an isolated molecule. In a crystal, both singlet and triplet excitons can be transferred through many molecules before the final recombination; the $T \rightarrow S$ transition requires the collision of two T excitons, as is clear from the energies involved and, finally, the light that can leave the crystal will consist of the singlet bands with $h\nu < 3.1$ eV. The magnitudes of the various rate constants and the details of this complex luminescence process may be found in Ref. (7). The maximum quantum efficiency to be expected may be estimated from the simplified decay scheme of Figure 2, which is adapted from the paper of Helfrich and Schneider.[4] The probabilities for decay of the electron–hole pair along the various paths are assumed to be proportional to the multiplicities of the states involved. The result of a T-T collision is an excited state that may have spin either 0 or 1; the former decays to the excited S state. This scheme yields a value for the quantum efficiency, $E_q = 0.35$; the more accurate value of 0.40 is derived in Ref. (4). This value of E_q is large compared to those commonly observed in large-bandgap semiconductors such as GaP, where $E_q < 1\%$ at room temperature.

We must also consider the electrical aspects of double injection in insulators. A complete review of the current theories may be found in the article by Lampert.[8] A basic assumption of all models is that both

[7] S. Singh, W. J. Jones, W. Siebrand, B. P. Stoicheff, and W. G. Schneider, "Laser Generation of Excitons and Fluorescence in Anthracene Crystals," *Jour. Chem. Phys.*, Vol. 42, p. 330, 1 Jan. 1965.

[8] M. A. Lampert, *Rept. Progr. Phys.*, Vol. 27, p. 329, 1964.

contacts are ohmic, and that traps play no role. The review paper by Helfrich[9] summarizes the results to date of double injection in organic crystals. These were mostly obtained with electrolytic contacts. Because of the large recombination rate constant, $K = 10^{-6}\ \text{cm}^3\ \text{sec}^{-1}$, between electrons and holes, it is concluded that the region of charge overlap (which is also the region of light emission) is limited to a

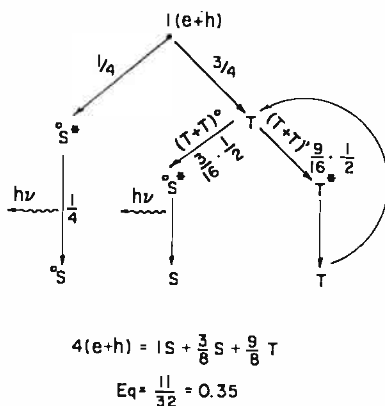

Fig. 2—Simplified decay scheme of the excitation produced by recombination of an electron–hole pair. The quantum efficiency is calculated by assuming that the probability for decay along a certain path is proportional to the multiplicity of the state involved.

fraction of the volume of the crystal. This was verified by observations on crystals approximately 5 mm thick. In such a case, one must describe the system as resembling two one-carrier space-charge-limited currents with slight overlap, rather than as an injected plasma. As we shall see, this description is not accurate at the high current levels of interest in this work. In this regime the contacts are not ohmic, and there appears to be a considerable amount of charge overlap in thinner crystals.

Construction of the Electroluminescent Diodes

Two types of cell construction were used; the first, on which most of the data reported was obtained, made use of single-crystal anthracene. The starting material was a cleaved plate, 1 to 2 mm thick. Most samples were obtained from boules of ultra-pure quality; however at

[9] W. Helfrich, article in *Physics and Chemistry of the Organic Solid State*, D. Fox, M. Labes, and F. Weisberger, Editors, Interscience Publ., Vol. III, New York, 1967.

the high current densities used in these experiments, commercially available crystals give a comparable performance. The wafer is etched lightly in benzene, following which the anode is deposited by vacuum evaporation. This normally consisted of an $Se_{50}Te_{50}$ alloy, although Au was also used. In the thinnest cells, the anode was in the form of a fine grid with 50% transmission, through which the light was observed. The anode side of the wafer was cemented on a transparent substrate with polystyrene. The thickness of the wafer was reduced by vacuum evaporation or, in a few cases, by solvent etching. The thinnest samples made in this way were about 30 microns thick, the limit being set by nonuniformities in the rates of evaporation or etching over the area of the wafer. The range of thicknesses in our experiments was 0.03 to 2 mm. The cathode consists of a bead of Na, K, or Na-K alloy applied from the melt in an inert atmosphere. All of these react with the anthracene to form layers of metal–anthracene complex, e.g., $[K^+][anth]^-$, which form the electron injecting contact and which are recognizable by their characteristic blue color. The Na-K alloy, which is liquid at room temperature, has the lowest work function of the group ($W = 2.05$ eV)[10] and is the easiest to apply in a controllable manner. However, K ($W = 2.3$ eV), which melts at 62°C, yields a more rugged cell. The alkali-metal beads are covered with a thin layer of polystyrene and then embedded in paraffin before exposing the cell to air. In cells where the wax was applied properly, no deterioration of the cathode was observed after nearly a year.

The second type of cell was made by melting ultra-pure (99.999%) anthracene powder between glass flats, one of which was coated with high-quality SnO_2 covered by a thin film of the anode material, Au or Pt, or by a grid of Te. The operation is done in an inert atmosphere to reduce contamination of the anthracene with oxygen. By proper control of the cooling, the melted layer can be made to recrystallize on the anode plate and will not adhere to the other plate. Although cells of area approaching 1 cm² and thickness < 10 microns were made by this method, measurements were possible only in cells 14-30 microns thick because of pinholes. The remainder of the construction is the same as above.

Characteristics of Diodes under Double Injection

The behavior of these anthracene diodes parallels that with electrolyte contacts. The currents are found to be from one to three orders

[10] A. Many, J. Levinson, and I. Teucher, *Phys. Rev. Letters*, Vol. 20, p. 1161, 1968.

of magnitude larger when both contacts are injecting than when one contact only is injecting. Light emission begins at fields of 10^4 V/cm rather than at fields larger than 5×10^5 V/cm, which is the case when poor contacts are used. The emitted light is also relatively free of fluctuations compared to that obtained from non-injecting contacts. The cell shown in Figure 3 is typical. In the low-current regime, $j < 10^{-4}$ A/cm^2, $j \propto V^5$. A relation $j \propto V^5/L^7$ was found for a series of cells with

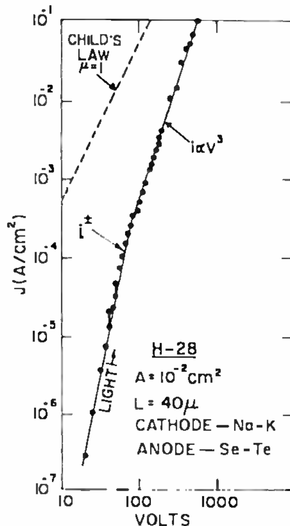

Fig. 3—Double injection current versus voltage in a diode 40 microns thick.

thickness L ranging from 0.1 to 3 mm. While the large exponents of L and V might be expected from space-charge-limited-currents controlled by an exponential trap distribution, the relation V^{l+1}/L^{2l+1} is not obeyed. Furthermore, as shown below, the contacts cannot be truly ohmic even at current levels of $j = 10^{-4}$ A/cm^2, so that the current is limited in part only by the trapped space charge. For $j > 10^{-4}$ A/cm^2, we find $j \propto V^3$. In some cells, $j \propto V^2$ or V^4 are also observed. In the cell of Figure 3, j does not exceed the value given by Child's law, i.e., the value for a one-carrier current injected in a trap-free insulator. However the Child's law value has been exceeded in a number of cells and this is then another indication that double injection is taking place. At the highest current level measured, $j = 10^{-1}$ A/cm^2, the 10^{-2} cm^2 diode dissipated 0.6 watt. It is remarkable that such a high current level can be passed continuously through such a thin insulator wafer without damage.

Light emission on this cell starts at about 35 volts. In all samples, the emitted light intensity was found to be linear with j in the high-current regime as shown in Figure 4 for two cells. Departures from linearity are found in some cells at low current levels. The linearity at the highest current levels shows that equal numbers of electrons and holes are injected, i.e., neither contact is saturated. If there were an excess of one injected carrier, this excess would be collected by the opposite electrode, and the resulting increase in current would not result in increased light emission.

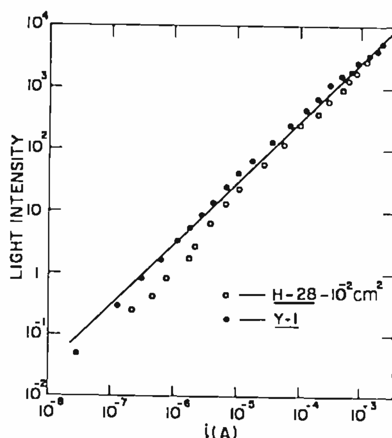

Fig. 4—Dependence of light emission on current.

The distribution of the light emission in the volume of the cell was observed microscopically through the side of a cell 1.2 mm thick. At all current levels where light could be seen ($j \geq 10^{-5}$ A/cm^2) some luminous filaments extended from anode to cathode. For $j > 10^{-4}$ A/cm^2 a broad luminous zone was superimposed, extending approximately 1 mm from the anode towards the cathode. The amount of charge overlap is then considerable, in contrast to the observations made on a crystal 5-mm-thick.[1] The location of the luminous zone spreading out from the anode is consistent with $N_{tp} \gg N_{tn}$; most of the injected holes are trapped. Note that at $j = 10^{-1}$ A/cm^2, $E \approx 10^5$ V/cm and the density of free carriers is 10^{13}/cm^3, which is small compared to the density of hole traps.

The external quantum efficiency E_q (quanta leaving the cell per injected electron) was determined by means of a photomultiplier calibrated with a thermopile. Values of E_q ranged from 1 to 8%. The emitted spectrum is a band from 4100-4800 Å, peaking at 4300 Å. The

rise and decay time of the luminescence is shorter than 5×10^{-4} sec, this value being the response time of the photomultiplier circuit used. Taking an approximate value of 3 eV for the energy of the emitted quanta, we can calculate a power efficiency $E_p = E_q\ (3/V)$ where V is the operating voltage. This quantity gives no physical information, but is an important design consideration as discussed below.

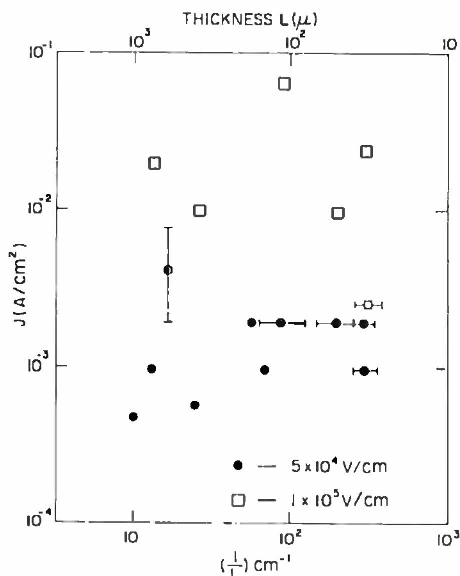

Fig. 5—Values of current density j for fixed fields of 5×10^4 and 10^5 V/cm for a number of cells.

Properties of Contacts

The observation of $j = 10^{-1}$ A/cm² implies that the contacts cannot be ohmic. We recall that photoemission measurements yield values for the potential barrier at the cathode $\Delta E = 0.79$ eV and at the anode $\Delta E = 0.9\text{-}1.0$ eV. Using the formula for thermionic emission,

$$j = 120\ T^2 \exp\left(-\frac{\Delta E}{kT}\right) \qquad \text{A/cm}^2,$$

we see that the cathode can furnish a thermionic current $j_{th} = 2 \times 10^{-7}$ A/cm² at 300°K. Even if there is a local heating of the electrode to, say, 100°C, $j_{th} = 3 \times 10^{-4}$ A/cm². However the stability of the diodes at high current levels makes the local-heating hypothesis implausible. Another possibility is that the current at high injection levels is fur-

nished by field emission from the contacts. This is suggested by the data of Figure 5, which shows the values of j obtained for a number of cells ranging in thickness from 30 to 1000 microns, for two values of the average field $V/L = 5 \times 10^4$ V/cm and $V/L = 10^5$ V/cm. At fixed field, j is essentially independent of L; the values of j vary by no more than one order of magnitude for a 30-fold change in thickness. The data of Figure 5 also include data for crystals differing widely in total trap density; this factor has no effect. We thus conclude that in the high-current regime, the current is not volume controlled.

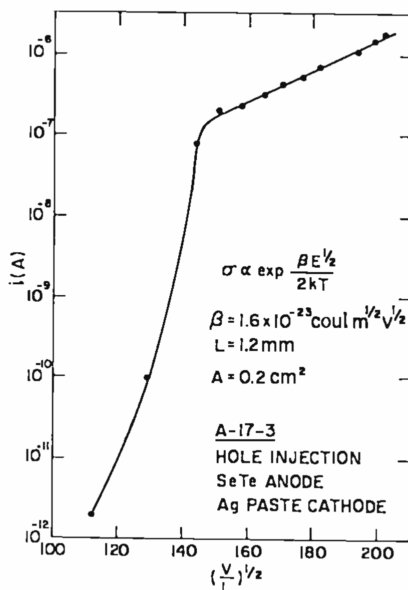

Fig. 6—Injection of holes as function of field. The cathode is non-injecting.

The field emission current is described by the Schottky equation

$$\sigma = A \exp \left\{ \frac{\beta E^{1/2}}{2kT} \right\},$$

where $\beta = [e^3/(\pi\epsilon_0\epsilon)]^{1/2}$ is the term representing the image field near a metallic contact. In the case where the carrier is extracted from a Coulomb attractive potential, $\beta = 2[e^3/(\pi\epsilon_0\epsilon)]^{1/2} = 6.6 \times 10^{-24}$ Coul $m^{1/2}$ $V^{1/2}$. With this value of β, the expression is known as the Frenkel–Poole equation. One might expect that this equation would hold at the cathode, where removal of an electron would leave behind a positively charged metal–anthracene molecule. In Figures 6 and 7, plots of one-

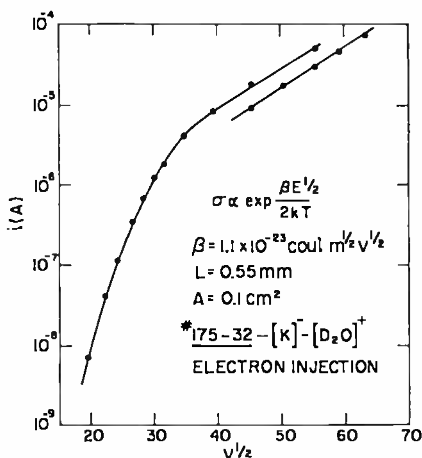

Fig. 7—Injection of electrons as function of field. The anode is non-injecting.

carrier injected current versus $V^{1/2}$ show that the field emission equation is obeyed for $V/L > 2 \times 10^4$ V/cm. The experimental values of β are larger by a factor of 2 than the values calculated by the Frenkel–Poole model. This result has also been found for field injection into vitreous Se;[11] no satisfactory explanation for it exists at the moment. In our case, it might originate in a modification of the surface field due to trap filling near the contact. Such trapping does have an effect on the current as shown by the data of Figure 8, discussed in the next section. By extrapolating the high-field portions of the curves of Figures 6 and 7 to zero field, the saturated thermionic emission current can be determined. The values of barrier height ϕ_{th} obtained in this manner are reasonably close to those determined by photoemission as shown in Table I. We conclude from these experiments that in the high-current regime, the current is contact controlled.

Table I

Sample	Carrier	$j_{V=0}$ (A/cm^2)	ϕ_{th} (eV)	ϕ/photoemission (eV)
21B	electrons	10^{-6}	0.77	0.79
A-17-3	holes	1.5×10^{-9}	0.94	0.9-1.0
175-33	holes	5×10^{-9}	0.90	

[11] M. Tabok and P. J. Warter, "Field-Controlled Photogeneration and Free-Carrier Transport in Amorphous Selenium Films," *Phys. Rev.*, Vol. 173, p. 899, 1968.

Practical Design Considerations

We note from Figure 3 that for the cell shown, $j = 10^{-1}$ A/cm^2 at 600 volts. The cell is operable at this current level continually, but the current decreases slightly with time as shown in Figure 8 for operation of this cell at 500 volts. The slow decrease to a steady level is probably due to filling of traps near the contact area; the diode recovers its original characteristics if the current is interrupted for 30 minutes.

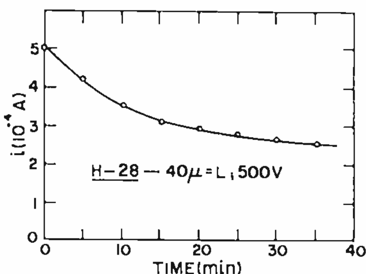

Fig. 8—Current versus time for a cell operated at constant voltage. The slow decay to a stable value is due principally to the filling of deep traps in the anode region.

These decay and recovery characteristics vary among individual cells. However, individual cells do not change their characteristics over 6 months of shelf life if the alkali metal contact has been properly passivated so that it cannot be corroded by moisture. No observations were made over longer periods of time.

The diode of Figure 3 has a quantum efficiency $E_q = 2\%$. At 600 volts, the power efficiency $E_p = 2(3/600) = 10^{-2}\%$. From an engineering standpoint it is desired to reduce the operating voltage at the highest current levels, not only to reduce the power dissipated but also to make the cell compatible with transistorized driving circuits. It is not likely that this could be achieved by different contacts. At the cathode, the photoemission measurements show that, after reaction of the metal with anthracene, the potential barrier is determined by the anthracene ions rather than by the work function of the metal. Even if this were not so, only Cs with $\phi = 1.8$ eV has a lower work function than the Na-K alloy ($\phi = 2.05$ eV). At the anode side, $\phi_{Se\text{-}Te} = 4.8$ eV, and some improvement might be expected with Au ($\phi = 5.2$ eV) and Pt ($\phi = 5.6$ eV). Experiments using evaporated Au with the present cell construction showed that Au formed a good contact only at a few points, and that the current density at those points was about the same as for Se-Te, at the same field.

Using the present contacts, it is clear that $E_p \propto 1/L$ in the high-current regime. In order to obtain operation at 50 volts for $j = 10^{-1}$ A/cm^2 in a cell of the same quality as that of Figure 3, an effective thickness of 3.5 microns is required. This is not a very thin layer according to the present state of thin-film technology.

We consider how to construct such a thin diode. Diffusion of the alkali metal into the crystal wafer was attempted. This is not feasible because of the high vapor pressure of anthracene at temperatures where diffusion is significant. Etching of the crystal wafer, either by evaporation in vacuum or by solution, was found to be limited in practice to thicknesses greater than 30 microns. This is due to local variations in the etching rate over the surface of the cell, which are found in nearly all crystal wafers. Occasionally, a crystal wafer is found of better quality, with no variations over a few mm^2; these are rare. The high initial cost of single-crystal wafers also makes this method unattractive.

A cheap and convenient method of growing single-crystal plates less than 100 microns thick and several cm^2 in area is growth from solution. Measurements were made on a number of such crystals, grown from solution in $CHCl_3$ and C_6H_6, which had been obtained through the courtesy of Prof. A. Cobas (University of Puerto Rico). The trap densities in these platelets were so large as to require an operating voltage about 10 times larger than for an equivalent cell made from melt-grown crystal. However, these platelets were grown in ordinary reagent-grade solvents under exposure to air. It is well known that oxygen as well as many organic impurities are very effective in creating traps in anthracene. It is probable that the quality of such plates could be improved significantly, but this was not attempted.

Another method used for cell fabrication was that of melted and recrystallized layers described earlier. We summarize the results obtained with such cells:

a) The highest currents were obtained with Te anodes. With Pt or Au, the anode contact was formed in only a few small spots of area $\leq 10^{-4}$ cm^2.

b) Observation of the light emission emanating from the space between the Te grid lines shows that Te a few monolayers thick makes an adequate anode.

c) Because of pinholes, observations were made only on cells with $L > 14$ microns, although layers as thin as 4 microns were grown.

d) The values of j at a fixed field for the cells measured did not show the consistency of the single-crystal cells of Figure 5. Fields of 2×10^5 V/cm were necessary in order to obtain $10^{-4} < j < 10^{-2}$. The large variation between samples and the higher fields necessary to obtain large currents are indicative of a large trap density in these cells (but much smaller than in solution-grown crystals).

The large trap densities are almost certainly the result of oxygen contamination. At the melting point of anthracene, the layers would react rapidly with oxygen. The cells were assembled in a polyethylene bag continuously flushed with N_2, a procedure that is not adequate to remove all traces of O_2 and H_2O.

The use of these polycrystalline layers appears to be the most promising method for making cells operating below 50 volts. The main problem at the moment is that of pinholes. There is little doubt that a method of reducing their number to a tolerable value could be found. Finally it should be noted that deposition of the cathode by vacuum evaporation is feasible; this would greatly simplify the construction of the device.

SWITCHING AND STORAGE CHARACTERISTICS OF MIS MEMORY TRANSISTORS

By

J. T. Wallmark* and J. H. Scott†

Summary—Memory transistors have been constructed in the form of MIS field-effect transistors in which the gate insulator consists of a double layer. Closest to the silicon is a 15 Å silicon dioxide layer covered by a layer of another insulator, which may be silicon nitride, 600 Å thick. At the interface between these two insulator layers, and at an energy level even with the silicon forbidden band, are traps in the form of disorder states. When silicon nitride is used, these traps are donor-type and each may give off an electron when the silicon is biased positively with respect to the insulator and recapture it when the silicon is biased negatively. The charge transport is by tunneling.

Switching times of 0.05 to 1 microsecond have been measured. The memory retention is longer than 2000 hours at room temperature. In contrast to ferroelectric gate structures, the memory transistor has a true threshold, allowing reading and voltage-coincident selection without disturbing the memory content. A physical model for the switching and memory retention is also presented.

Memory Effect

When MOS FIELD-EFFECT transistors were first developed, it was soon discovered that the electrical characteristics exhibited an instability in the form of a gradual shift of the threshold voltage, particularly noticeable under positive gate bias and high temperature. The causes of these phenomena were later traced to ion (particularly sodium) migration and electrochemical changes at the silicon–silicon-dioxide interface.[1] That tunneling of

* RCA Laboratories, Princton, N.J.

† Formerly RCA Laboratories, Princeton, N.J.; now Chalmers University, Göteborg, Sweden.

[1] S. R. Hofstein, "Stabilization of MOS Devices," *Solid-State Electronics*, Vol. 10, p. 657, 1967.

charges into and out of states in the oxide could be a factor in this picture was also brought out.[2] When investigation of silicon nitride revealed that it possessed a denser structure than silicon dioxide and, therefore, retarded ion migration, it was suggested that it might offer a better gate insulator in field-effect transistors. However, early attempts to construct silicon nitride field-effect transistors failed because very large instability effects showed up as hysteresis in the threshold voltage.[3-11] It was subsequently suggested that this hysteresis effect might be used in a new memory element.[12,13]

We have found that the hysteresis in the gate capacitance versus gate voltage curve is caused by the storage of charge in states located at the interface between a very thin silicon dioxide layer and the covering silicon nitride layer. The transport of charge into and out of these states takes place by tunneling as a result of a large positive or negative gate voltage. Tunneling into and out of states in the insulator also takes place in silicon dioxide, and gives rise to the so-called "slow-trapping instability" discussed by Hofstein.[1] However, the number of states in high-quality silicon dioxide is quite low ($<10^{11}/cm^2$), too low to be of interest here. As shown later, the slow-trapping instability is undesirable in memory transistors.

---

[2] F. P. Heiman and G. Warfield, "The Effects of Oxide Traps on the MOS Capacitance," *IEEE Trans. Electron Devices*, Vol. ED-12, p. 167, 1965.

[3] J. H. Scott and L. A. Murray, "Physical and Electrical Properties of Vapor-Deposited Silicon Nitride Films," Presented at the Electrochemical Society Meeting, Philadelphia, Sept. 1966.

[4] S. M. Hu, D. R. Kerr, and L. V. Gregor, "Evidence of Hole Injection and Trapping in Silicon Nitride Films Prepared by Reactive Sputtering," *Appl. Phys. Letters*, Vol. 10, 97, Feb. 1, 1967.

[5] W. E. Dahlke and S. M. Sze, "Tunneling in Metal-Oxide-Silicon Structures," *Solid-State Electronics*, Vol. 10, p. 865 (1967).

[6] T. L. Chu, J. R. Szedon, and C. H. Lee, "The Preparation and *C-V* Characteristics of Si-Si_3N_4 and Si-SiO_2-Si_3N_4 Structures," *Solid-State Electronics*, Vol. 10, p. 897 (1967).

[7] C. L. Hutchins and R. W. Lade, "Charge Storage in Metal-Silicon Nitride-Silicon Capacitors," (Letter) *Proc. IEEE*, Vol. 55, p. 1494, (1967).

[8] B. E. Deal, P. J. Fleming, and P. L. Castro, "Electrical Properties of Vapor-Deposited Silicon Nitride and Silicon Oxide Films on Silicon," *J. Electrochem. Soc.*, Vol. 115, p. 300, 1968.

[9] D. M. Brown, P. V. Gray, F. K. Heumann, H. R. Philipp, and E. A. Taft, "Properties of $Si_xO_yN_z$ Films on Si," *J. Electrochem. Soc.*, Vol. 115, p. 311, 1968.

[10] T. L. Chu, J. R. Szedon, and C. H. Lee, "Films of Silicon Nitride—Silicon Dioxide Mixtures," *J. Electrochem. Soc.*, Vol. 115, p. 318, 1968.

[11] M. J. Grieco, F. L. Worthing, and B. Schwartz, "Silicon Nitride Thin Films from $SiCl_4$ Plus NH_3: Preparation and Properties," *J. Electrochem. Soc.*, Vol. 115, p. 525, 1968.

[12] H. A. R. Wegener, A. J. Lincoln, H. C. Pao, M. R. O'Connell, and R. E. Oleksiak, "The Variable Threshold Transistor, A New Electrically-Alterable, Non-Destructive Read-Only Storage Device," International Electron Devices Meeting, Oct. 1967, Washington, D. C.

[13] H. C. Pao, M. O'Connell, "Memory Behavior of an MNS Capacitor," *Applied Phys. Letters*, Vol. 12, p. 260, April 15, 1968.

One method of making the insulator–insulator interface state density large is the introduction of a metal layer between the two insulators.[14] However, we have found that such metal layers lead to very poor memory-retention characteristics. The reason for this seems to be that conduction laterally along the metal layer to the exposed edge creates a leakage path on the surface from the metal layer to the silicon. The time constant of such surface paths, even in dry laboratory ambients, is usually only minutes to hours. For a memory device, this mechanism is much inferior to the "bulk" time constant from the traps at the insulator–insulator interface. To make the metal layer so thin that conduction laterally is negligible appears impractical and of questionable merit. Therefore, the natural disorder states between the two insulator layers are used.

Because of the success of the ferromagnetic memory element, a great many attempts have been made to invent a ferroelectric memory element. The use of ferroelectric insulators in the gate structure of MOS field-effect transistors[15] is one of the latest of these efforts. However, these attempts have not been very successful for several reasons. One important reason is that ferroelectric materials do not have a true threshold; a threshold is essential if half-select voltages are to be applied without changing the memory content. Another reason is the imperfect understanding of interface and bulk effects encountered in such structures. The present memory element is analogous to the ferroelectric memory element except that the storage is not achieved by polarization, but by tunneling of charges into and out of states in the insulator. For reasons discussed later, this gives a true threshold and a technologically simpler system.

Design of the Memory Element

The fundamental memory unit using the charge-storage effect discussed above is an MIS capacitor. As a memory element, the capacitor has two serious shortcomings. First, the use of capacitors in a cross-grid array is difficult, since stray currents through the grid network cannot be avoided unless each selected element is very strongly nonlinear (as, e.g., a diode). An attractive way to make the element nonlinear is to combine the capacitor with a diode or a transistor. Second, the magnitude of the capacitance for a small element is quite small—

[14] D. Kahng and S. M. Sze, "A Floating Gate and Its Application to Memory Devices," (Letter) *Bell Syst. Tech. J.*, p. 1288, 1967.

[15] R. P. James, "The FEFET—A Ferroelectric Adaptive Component," Stanford Electronics Laboratories, Stanford University, Tech. Rep. No. 4663-1, Oct. 1967 (6 references to earlier work).

so small that it is difficult to distinguish from the stray capacitances of the X and Y address lines. Use of a larger element with its increased capacitance is undesirable for yield reasons. Again, by combining the capacitor with a transistor the influence of the capacitive storage can be magnified sufficiently to set it apart from the capacitance of the address lines. In other words, the combination of the capacitor storage element with a transistor allows the former to be of very small size, compatible with good yield.

For these two reasons, the storage element described here is a field-effect transistor with a storage capacitor as the gate structure. The storage mechanism differs from the RC storage conventionally found in MOS transistors because the charge carriers are trapped.

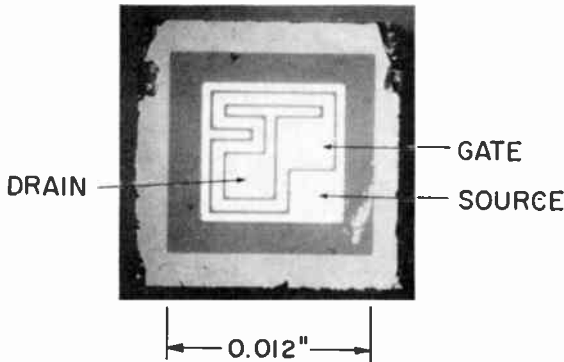

Fig. 1—Top view of memory transistor. Channel length is 0.4 mil and channel width 40 mils.

Transistor Fabrication

The fabrication of the transistors was identical to the fabrication of regular n-channel MOS field-effect transistors, except with regard to the insulator. Thus, the substrates are 10 ohm-cm, p-type, (100) oriented, chemically polished silicon wafers. The channel oxide was grown in a conventional steam oxidizing furnace at about 600°C for 30 minutes. After this step the oxide thickness is usually 15 ± 2 Å. A silicon nitride layer of 100-800 Å is then deposited by reaction of silane in ammonia, with argon as carrier gas, at 600-800°C. The nitride is defined by photoresist technique and aluminum is deposited by vacuum evaporation and again defined by photoresist technique. The geometry is shown in Figure 1.

Many of the studies presented in this paper were made on capacitors rather than complete transistors, since transistor action was often

not essential. The insulator of the capacitors was made by the same technique as the gate insulator. The silicon nitride contacts were 0.030-inch-diameter aluminum dots evaporated through a mask. The back contact was a large-area evaporated aluminum layer.

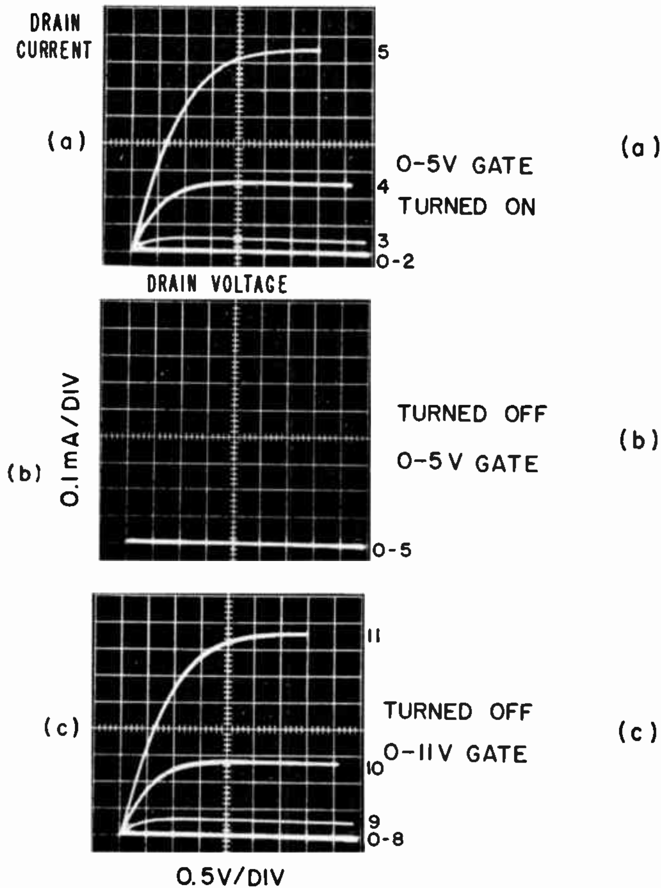

Fig. 2—Drain current versus drain voltage with gate voltage as parameter for enhancement-type unit: (a) transistor has been turned ON by 1-sec gate pulse of −25 V; (b) transistor has been turned OFF by 1-sec gate pulse of +25 V; and (c) same as b, but with larger gate-voltage range.

Memory-Transistor Characteristics

The behavior of the memory transistor is illustrated by Figures 2 and 3. Figure 2(a) shows the drain current versus drain voltage characteristics, with the gate voltage as parameter, in the ON state. After the application of a gate-voltage pulse of typically +25 V for a fraction

of a second, the characteristics change as shown in Figure 2(b), i.e., no current flows for the same applied voltages. However, when the gate voltage is varied over a larger range, the characteristics shown in Figure 2(a) reappear, but with the threshold voltage shifted. The new characteristic curves are shown in Figure 2(c) and indicate a shift of 5 V in threshold voltage.

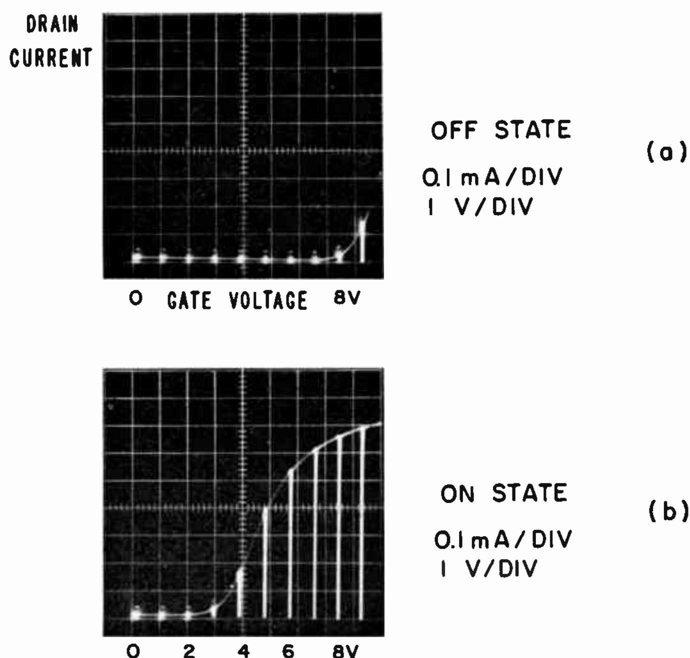

Fig. 3—Drain current sampled for $V_D = 4$ V and gate voltage stepped in 1-V steps. Threshold voltage has shifted about 6 V between ON and OFF.

After application of the +25 V pulse the transistor is in its OFF state. The transistor may be returned to the original ON state by the application of a gate voltage pulse of −25 V for a fraction of a second. The characteristic curves shown in Figure 2 result after the gate-voltage pulse has terminated.

Figure 3 shows the same sequence in terms of transfer characteristics. Figure 3(a) shows drain current versus gate voltage with the transistor in the OFF state and Figure 3(b) shows the same transistor in the ON state. The transistor will remain in its ON or OFF state as long as the gate or drain voltage does not exceed a threshold voltage discussed later.

Analog Setting of the Memory

In the previous section, only gate signals of ± 25 V were considered. However, a partial shifting of the flat-band voltage may be accomplished by the application of intermediate voltages to the gate. Figure 4 shows a typical sequence of measurements of capacitance

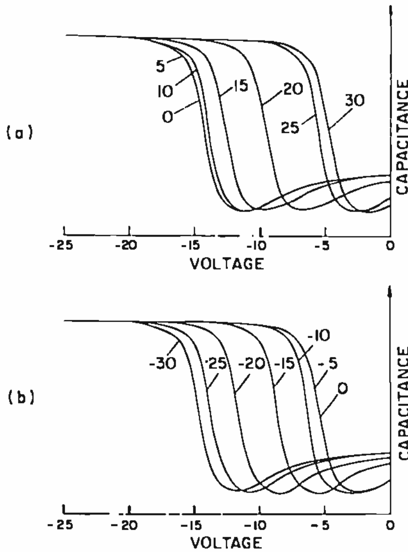

Fig. 4—Capacitance-versus-voltage curves illustrating analog behavior.

versus voltage performed on capacitors simulating the gate capacitance. Initially, the gate was made -25 V for about a second, after which the capacitance versus voltage was measured resulting in the left curve in Figure 4(a) marked "0". It has been found experimentally that if the voltage traverse during measurement is limited to less negative voltages than -25 V the stored charge does not change during measurement. Then the gate was made $+5$ V for about a second, and the capacitance-versus-voltage curve was retraced. No change was observed. When the gate was then made $+10$ V for about a second, and the curve was again traced, the curve marked "10" in Figure 4(a) resulted. The capacitance-versus-voltage curve had shifted slightly, indicating that a charge transfer had taken place. The unit was then reset, i.e., the capacitance-versus-voltage curve was returned to its initial position, by the application of -25 V for about a second. The procedure was repeated with voltage increments of 5 V until a saturation of the shift was found at 30 V.

The results shown in Figure 4(b) were obtained in a similar way by starting with the application of +25 V for about a second and then applying negative voltages with −5 V increments, measuring between each pulse.

As may be seen, the shift in flat-band voltage is fairly linear in the middle range and decreases to near zero at each end.

MEMORY PERMANENCE

For this type of memory to be useful, the memory permanence, i.e., the time it takes for the charge stored in the insulator to decay, must be long. Earlier experience with stored-charge memories using capacitor storage has, from this point of view, offered little encouragement. In the memory transistor, however, the storage appears quasi-permanent with a storage time of at least 4000 hours (i.e., six months) at room temperature with no voltage applied.

The experiments on storage permanence were performed on capacitors prepared as described earlier. The measurements were made by capacitance-versus-voltage plots, recording the midpoint (approximately the flat-band voltage) of the capacitance as it changed from its minimum value to the oxide capacitance in accumulation. A number of capacitors on the same wafer were switched ON by a negative (on the metal) voltage of typically −20 V, while a number of capacitors on the same wafer were switched OFF by a positive voltage of the same magnitude. The wafers were then stored in plastic or glass containers and the capacitances remeasured at intervals.

The results of four independent runs (each of about four capacitors) at room temperature and one run at 150°C (measurements done at room temperature) are shown in Figure 5. Because the units had different initial flat-band voltages and were set ON or OFF by varying amounts, the data cover a large spectrum of voltage levels. The conclusion is that the stored charge is permanent within the accuracy of measurement for at least 4000 hours at room temperature. At 150°C, the voltage shifts by about 2 V in 1000 hours.

A word of caution regarding the memory permanence is in order. Occasionally, a wafer has been encountered in which the permanence is below average. The performance of one such wafer, presumably processed in the same way as the others, is shown in Figure 6. This wafer was first monitored at room temperature for 115 hours, in which time a shift of about 1-2 volts was found. Then it was subjected to 150°C for 700 hours and the rate of change then increased. All the devices on the wafer behaved similarly, and the OFF devices behaved

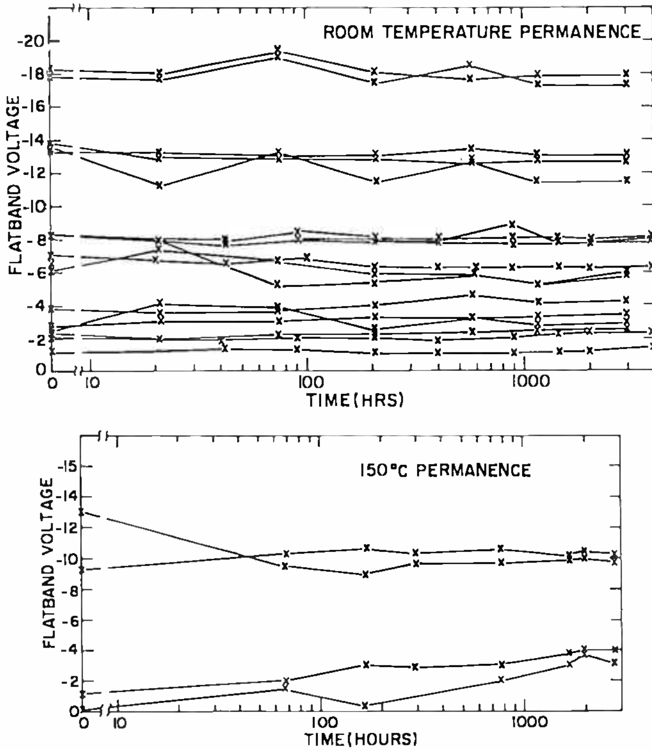

Fig. 5—Flat-band voltage versus time: (top) room-temperature shelf-life tests of units set at various degrees of ON or OFF; (bottom) 150°C shelf-life tests.

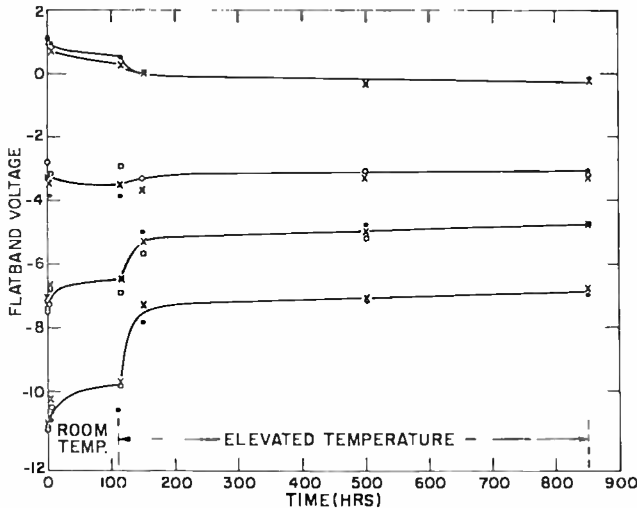

Fig. 6—Flat-band voltage versus time for wafer with poor memory retention. After 115 hours, the temperature was increased from room temperature to 150°C.

similarly to the ON devices. One might suspect that for some reason, the oxide layer may be leaky because of included impurities or defects.

DC Bias Effects

The MOS transistor has a long history of difficulties caused by the transport of ions, particularly sodium, through the insulator under temperature and bias stress.[1] In "dirty" layers this transport is readily noticeable at room temperature. As such transport would interfere

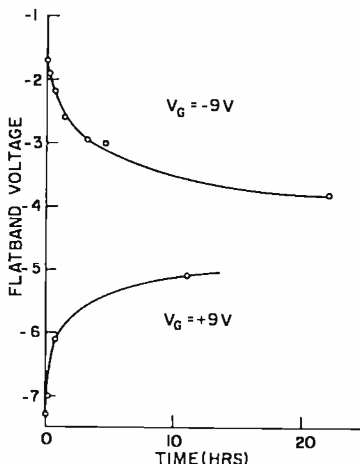

Fig. 7—Typical flat-band voltage-versus-time curves for biased samples.

with the memory action, a test was made to see how large an effect could be detected. A capacitor with the standard oxide–nitride insulator was subjected to a bias of ±5 V at 300°C for 5 minutes. The resulting shift in the capacitance-versus-voltage curve was only 0.2 V, indicating that no trouble should be expected from ion-transport instability. This result is reasonable, as the silicon nitride layer is known to resist sodium migration.

Later experiments with a number of transistors, in which the gates were biased with varying voltages at room temperature for a day or two, indicated that a bias instability exists that is similar to the "slow trapping instability" described by Hofstein.[1] Typical results are shown in Figure 7. This instability results in a positive shift of the flat-band voltage for positive bias on the gate, and vice versa. The effect saturates in a few hours. The flat-band voltage remains for at least several weeks at the value it had when the bias was removed. The shift is reversible with voltage. The magnitude varies considerably from

unit to unit; the smallest observed shift was 0.2 V in 15 hours (−9 V on the gate), and the largest was 4.4 V in 10 hours (+9 V on the gate). This type of instability was ascribed by Hofstein to trapping of electrons in traps in the oxide a few angstroms from the silicon surface. It was suggested that this kind of instability might be eliminated by helium or hydrogen annealing at 1200°C, and this is now being tried on the memory transistors.

There is some basis from the theory of the transistor to expect a small amount of bias instability as a result of the charge or discharge of the traps furthest removed from the oxide–nitride interface; this effect would have a long time constant. The fact that as small a change as 0.2 volt has been observed gives hope that ultimately all units can be made this stable, or even more stable.

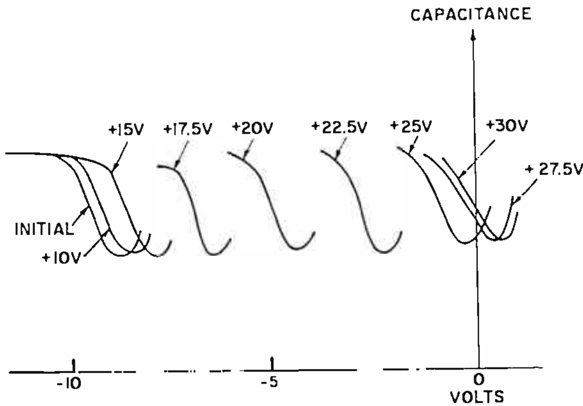

Fig. 8—Capacitance-versus-voltage curves for transistor (source, drain and substrate tied together) initially pulsed 1 sec, −25 V on the gate. Then positive single pulses ranging from 0-30 V have been applied to the gate. After each pulse the capacitance versus voltage curve has been measured and is shown here, and the gate has been returned to its initial state by the application of −25 V for 1 sec.

Switching Speed

In preparation for measurement of the switching speed, the hysteresis "window" in the capacitance-versus-voltage diagram of a memory transistor was determined, as indicated in Figure 4. Two extreme curves were then selected that correspond to the ON and the OFF condition; in this case the curves corresponded to applied voltages of −22.5 and +22.5 volts. Starting with application of −22.5 V for a second or two, followed by a positive pulse of 1 second duration and a known amplitude, the capacitance-versus-voltage curve was again measured. After each pulse the transistor was returned to the starting

condition by the application of −22.5 V. Figure 8 shows the result of this measurement. As can be seen, the window is traversed by pulses ranging from about 12.5 to 27.5 volts. Thereafter, the sequence was repeated with shorter pulses. Similarly, measurements were made of the results of negative pulses, returning each time to a starting point in the right-hand side of the window by the application of +22.5 V to the gate. Figure 9, which is a summary of the results, shows the shift of the flat-band voltage versus the pulse height with the pulse duration as parameter.

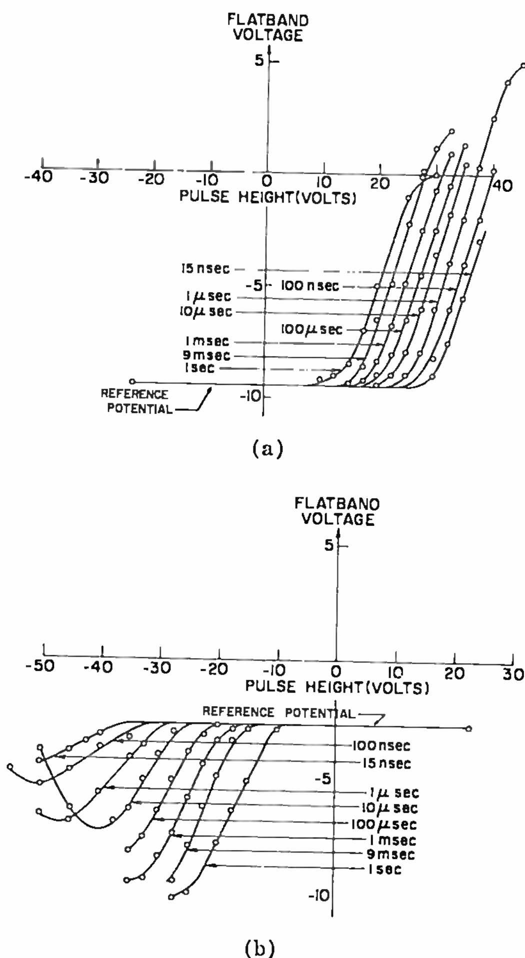

Fig. 9—Summary of switching measurements, such as those shown in Figure 8, for different pulse widths ranging from 1 sec to 15 nsec, (a) positive and (b) negative.

There are several features of Figure 9 that stand out. First, as the pulses become shorter, their amplitude must be increased to shift the flat-band voltage curves a given amount. A very short pulse does not allow enough time for tunneling to traps far from the interface. Consequently, if the pulse is short, it also must be of greater magnitude so that traps closer to the interface are brought to the conduction or valence band edge. This is illustrated in Figure 10.

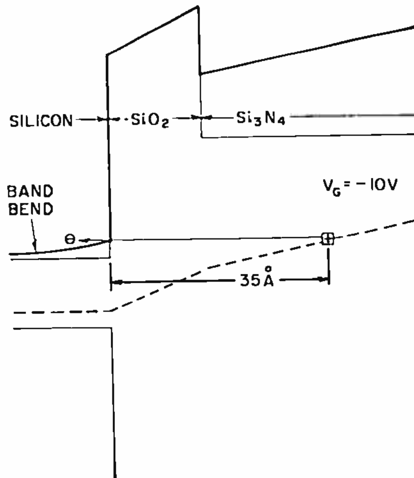

Fig. 10—Band picture of charge transport under pulsed conditions. Only traps level with, or outside, the silicon band edges can give off or take up electrons.

A second feature shown by Figure 9 is that for negative pulses (Figure 9(b)) the maximum shift in flat-band voltage increases as the pulse length increases, and for positive pulses (Figure 9(a)) the shift in flat-band voltage increases as the pulse length decreases. For positive pulses shorter than about 9 milliseconds, the voltage excursion actually brings the capacitance curve into the area of positive voltages, i.e., the transistor changes from a depletion transistor to an enhancement transistor. This cannot be a result simply of neutralizing the positive charge. In addition, a negative charge must be introduced into the insulator. It is believed that at the high fields created, electrons tunnel from the silicon into the silicon nitride conduction band as indicated in Figure 11 and, subsequently, move through the nitride. When the pulse terminates, many electrons are trapped in shallow traps giving rise to a negative space charge in the insulator.

A third feature of Figure 9 is that the switching is asymmetric, in that negative pulses must be larger than positive pulses for the same

shift. Two reasons for this are that (1) the silicon is p-type so that the band bending in the silicon during pulsing will be more extreme for negative pulses and (2) the trap level is asymmetric with respect to the silicon mid-gap energy. A third reason is that the injection of electrons from the gate contact at high electric fields results in what may be called anomalous hysteresis, as described below.

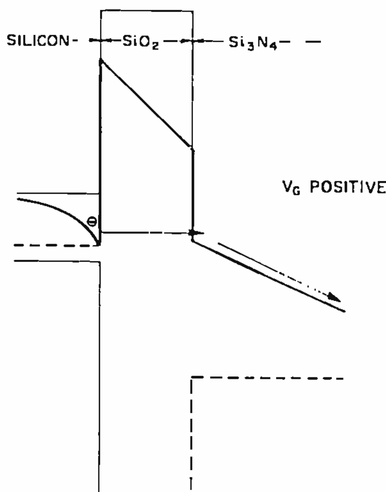

Fig. 11—Injection of electrons from the silicon inversion layer into the conduction band of the silicon nitride at high voltages.

Normal and Anomalous Hysteresis

One of the initially puzzling features of the hysteresis effect in silicon nitride devices was that some investigators reported a shift of the flat-band voltage to more negative values under an applied negative voltage, while other investigators reported the opposite, i.e., a shift of the flat-band voltage in the positive direction under applied negative voltages. It is now clear that the direction of shift depends on the interface at which the major charge transport takes place.

Consider Figure 12, which shows the band picture for an insulator-on-semiconductor capacitor. When a sufficiently high negative voltage is applied to this capacitor, electrons may leave traps at the semiconductor–insulator interface, resulting in a positive charge in the insulator. This represents a "normal" shift of the flat-band voltage, i.e., the flat-band voltage shifts in the same direction as the applied voltage. On the other hand, if there are no traps at the semiconductor–insulator interface, and the barrier at the metal contact is low enough, electrons

may be introduced from this contact into the conduction band or directly into traps at this interface. This leaves the opposite polarity charge in the insulator and, therefore, leads to a shift of the flat-band voltage in the opposite direction—"anomalous" hysteresis.

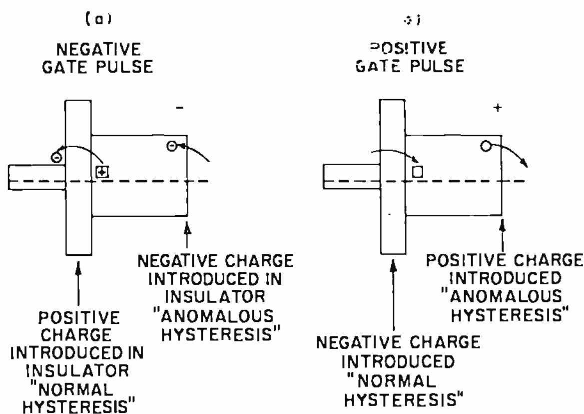

Fig. 12—Band picture to illustrate normal and anomalous hysteresis. Note the polarity of charge left in the insulator for each case.

It is easy to see, as illustrated in Figure 12(b), that a positive voltage gives similar results, i.e., charge transport across the semiconductor–insulator interface gives normal hysteresis, while charge transport across the metal–insulator interface gives anomalous hysteresis. The arguments are the same if the charges are holes rather than electrons.

Returning now to Figure 9, note that in two cases where high negative pulse amplitudes have been used, the shift first increases and then decreases. Pulsing to still higher voltage has been tried and leads to further decrease of the flat-band voltage shift. It is possible to bring the entire family of curves for negative pulses into a series of parallel-shifted curves identical to the curve for 1-second pulses by correcting them with an assumed curve over the injected negative charge at the gate contact. This is shown in Figure 13. To each ordinate has been added the ordinate of a hypothetical injection curve chosen for best fit.

If this picture is correct, it should be possible by choice of a gate metal with higher work function, such as gold, or by modifying the insulator at the interface, to transpose the injection of electrons to electric fields higher than those used for switching and, thereby, much improve the symmetry of switching.

The Silicon Dioxide Layer

The role of the silicon dioxide layer is to create a tunnel barrier and to control the tunneling distance to the disorder states. The layer should not be too thick, as this would cause the tunneling probability to decrease and the response time of the states to become too long. On the other hand, it should not be too thin, as then excessive switching voltages would be needed as explained later. It is very difficult to prepare a layer in room ambient that is thinner than about

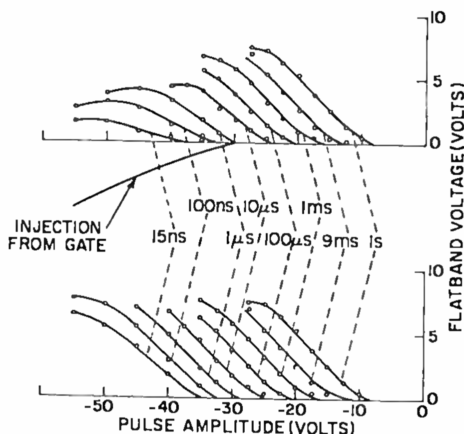

Fig. 13—Figure 9(b) corrected by combining it with a curve showing injection of electrons with voltage.

15 Å. By special measures, such as preparing the nitride at very high temperature, the oxide could be taken up by the nitride, but then the trap density would be that of the nitride, i.e., very low. Also the dielectric constant of the nitride is high, about 7, so that the field would not be concentrated at the surface and, therefore, the switching voltages would be twice as large (or the thickness of the insulator half as large) for the same tunneling distance, i.e., the same frequency response. The problem of growing a nitride layer as perfect as the oxide layer and with the large number of states at the proper distance has not yet been solved. While we must, at present, accept an inner layer of silicon dioxide, there are many alternatives to the silicon nitride layer on the outside, as described later.

The role of the thin silicon dioxide layer closest to the silicon surface is illustrated by the experiment summarized in Figure 14. In this

experiment, seven wafers were prepared on which the silicon dioxide layer thickness was varied. The thinnest layer was prepared as described earlier. Thicker layers were obtained by first preparing the thin layer and subsequently continuing the oxidation of each sample for 30 minutes in the range 600–800°C. The thicknesses covered the range 14–118 Å. The covering silicon nitride layer was deposited under

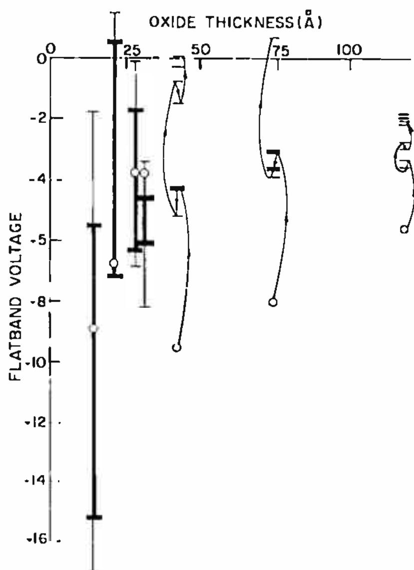

Fig. 14—Flat-band voltage for seven samples with different oxide thickness. The initial flat-band voltage is shown as a circle. The hysteresis window for ±30 V is shown as a thick vertical bar. The hysteresis window for ±35 V is shown as a thinner vertical bar. For oxide thicker than about 35 Å, no appreciable hysteresis is obtained. Instead, the flat-band voltage shifts towards zero each time a positive pulse is applied. Pulse lengths were about 1 sec.

identical conditions for each wafer and had a thickness of 750 Å. On two of the samples, those with oxide thickness of 28 and 31 Å, the silicon nitride layer had a thickness of 350 Å.

Standard capacitors were prepared on each wafer and capacitance versus voltage curves were taken. The initial flat-band voltage for each sample is indicated by a circle. This initial value is dominated by the charge present initially in the nitride layer, as shown later, and need not concern us here. Under the conditions at hand, the initial flat-band voltage is approximately −8 volts. The samples with thinner silicon nitride show an abnormally low initial flat-band voltage which is explained later.

As a next step the capacitors were subjected to positive and negative voltage pulses of about one second duration and of successively increasing amplitude. For voltages less than ±20 volts, no change in the flat-band voltage was observed; 20 volts corresponds to a silicon nitride field of about 2×10^6 V/cm. For voltages of ±20 volts, minute changes were observed that were too small to show in Figure 14. For voltages of ±30 volts, the flat-band voltage shifted as indicated by the thick horizontal bars in Figure 14. For low oxide thickness, these flat-band voltages were reproducible, and cycling back and forth between positive and negative applied voltages did not change the values. The resulting hysteresis window is indicated in Figure 14 by a thick vertical line. It is immediately apparent from Figure 14 that this window is largest for very thin oxide layers and that it approaches zero in the range of 35-40 Å oxide thickness.

The same behavior was obtained when the applied voltage was increased to ±35 volts. The corresponding flat-band voltages are indicated in Figure 14 by thin bars. Again, the values were reproducible and cycling back and forth did not change them. The corresponding windows, shown in Figure 14 as thin lines, are larger than at ±30 volts and again approach zero somewhere in the range 35-40 Å .

For oxide thicknesses above 40 Å, the behavior was entirely different. For applied voltages less than 20 volts no change was observed. For ±20 volts, the changes were too small to show in Figure 14. For −30 volts, the change was also too small to show. For +30 volts, a large shift towards less negative flat-band voltage, similar to that observed with thin oxide samples, was observed. However, a subsequent −30 volt pulse produced only a minor negative shift. A following, positive, applied voltage resulted in another large shift to less negative values. After a few steps, the flat-band voltage was close to zero, and further applied voltages only gave an imperceptable window. The sample with 118 Å oxide was even less sensitive to voltage, the oxide here taking up an appreciable fraction of the voltage.

The Silicon Nitride Layer

Several alternatives for the outer insulator layer are possible. The ones tried and reported here are silicon nitride deposited by reaction of silane in ammonia at 600-800°C; aluminum oxide deposited by oxidation of trimethylaluminum at 450°C; aluminum oxide formed by anodic oxidation of aluminum in a gas discharge in oxygen at essentially room temperature; silicon dioxide deposited by oxidation of silane in oxygen at 330°C; silicon nitride deposited by high-frequency sputtering.

Most of the deposition methods suffer from the same basic difficulty—the layers form by nucleated growth and, therefore, must be comparatively thick to achieve sufficient uniformity and freedom from defects to avoid pinhole problems. As a consequence, films with a thickness in excess of 800 Å have been used in most of the work reported. For such thick insulator layers, the switching voltage becomes very large, >30 volts. In a practical memory such large voltages would be very awkward, or even prohibitive, if high-speed switching is desired.

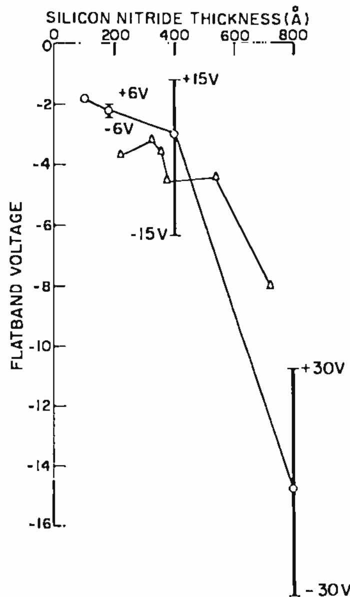

Fig. 15—Flat-band voltage for 10 samples of two runs with different silicon nitride thickness. The initial flat-band voltage is indicated by a circle (triangle). The hysteresis window for positive and negative voltages scaled approximately to the thickness is indicated by vertical bars. The oxide thickness was 15 Å.

The problem is illustrated by the experiment sumarized in Figure 15. The silicon nitride layers of various thicknesses in the range 100-800 Å were applied over a 15-Å layer of SiO_2 on identical wafers. The thickness was controlled by varying the time in the nitride deposition furnace. Figure 15 shows the initial flat-band voltage and the hysteresis window for voltages corresponding to $\pm 3.8 \times 10^6$ V/cm in the nitride for one of the runs.

Considerable difficulty was encountered by breakdown in the thin samples and only a few of the capacitors withstood the test voltages.

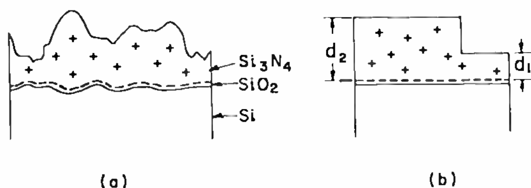

Fig. 16—(a) Schematic picture of the nitride layer in cross section and (b) highly idealized cross section with only two thicknesses.

If the bulk charge in the silicon nitride is responsible for the initial flat-band voltage and the middle point of the window, then one would expect the results in Figure 15 to show a linear relationship, i.e., the window midpoint and the initial flat-band voltage should be a linear function of the nitride thickness, and at zero nitride thickness there would be zero voltage. The reason this is not the case is believed to be the unevenness of thin nitride layers, as illustrated in Figure 16. In Figure 16, the nitride insulator layer has schematically been divided into two parts, one of thickness d_1 and the other of thickness d_2. The overall capacitance of the structure is determined mainly by the thin section, which has a larger capacitance, rather than by the thick section. The measured amount of nitride charge will also be weighted more by the thin section, where the bulk nitride charge is less.

Figure 17 shows similar results for the outer insulator layer consisting of aluminum oxide 600, 800, and 1200 Å deposited by oxidation

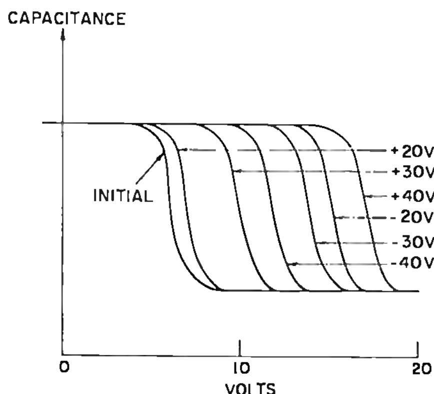

Fig. 17—Capacitance-versus-voltage curves for unit capacitor with 800 Å pyrolytically deposited aluminum oxide outer insulator. The curves are measured initially, and after the application of 1-sec pulses of 20, 30, 40, −20, −30 and −40 V, in that order.

of trimethylaluminum with nitrogen as diluent in oxygen at 450°C,* again with an underlying 15-20 Å SiO_2 layer. Here the bulk charge is negative but the general trend is the same as with silicon nitride. However, compared to silicon nitride samples, these samples had less uniformity of characteristics from sample to sample and had a high incidence of anomalous hysteresis and breakdown. For this reason no further experiments were performed.

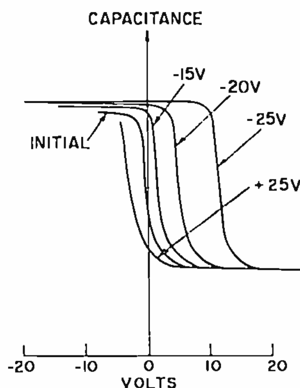

Fig. 18—Capacitance-versus-voltage curves for unit with 1300 Å low-temperature deposited silicon dioxide outer insulator. Strong anomalous hysteresis.

Figure 18 shows results with a unit with an outer insulator of 1300 Å silicon dioxide deposited by oxidation of silane in oxygen at 330°C.† It shows capacitance versus voltage curves obtained initially and those obtained after the application of 1 second pulses of −15, −20, −25 and +25 V. The hysteresis is large but entirely anomalous. The memory retention is short, of the order of seconds. The interpretation of this result is that because of the low dielectric constant of silicon dioxide (3.8) compared to silicon nitride (≈7) the electric field at the gate contact is much higher in the dioxide case, resulting in injection of electrons from the gate and, consequently, anomalous hysteresis. The absence of any normal hysteresis shows that the interface trap density utilized for the normal memory effect must be small. The injected electrons are trapped in shallow traps from which they are easily excited, leading to the short memory retention observed.

Aluminum oxide, 300, 450, and 700 Å, prepared by anodic oxidation

* Sample prepared by W. Kern, RCA Laboratories.

† Samples prepared by D. Flatley, RCA Laboratories.

of aluminum in oxygen gas, was also tried.‡ Although hysteresis was observed, no complete measurement could be made because of conduction and breakdown in the films.

A final experiment was made using silicon nitride films 200, 500, and 800 Å thick, prepared by high-frequency sputtering of silicon in nitrogen gas.* These films apparently contained such a large positive charge density (perhaps of excess silicon) that the surface potential could not be varied enough for the test. The films often broke down during measurement, indicating nonuniform structure.

Table I—Summary of Outer-Insulator Experiments

Insulator	Deposition Method	Bulk State Type	Bulk State Density	Threshold Voltage	Thickness of Layer
Silicon Nitride	600°-800° Silane + NH_3 + Ar	Donor	2×10^{18} cm^{-3}	−2 to −15 V.	(200-800 Å)
Silicon Dioxide	330° Silane + O_2 + N_2	Acceptor	4×10^{17} cm^{-3}	+3V	(1300 Å)
Aluminum Oxide	450° Trimethyl-aluminum + N_2 + O_2	Acceptor	1×10^{18} cm^{-3}	+6V	(1000 Å)
Silicon Nitride	High Frequency Sputtering of Si in N_2	Donor	High	—	

The conclusions to these experiments with different outer insulator layers are that at least one insulator, deposited aluminum oxide, works as well as silicon nitride, except that the deposition needs attention to give more uniform layers. It is believed that many other high-dielectric-constant, high-bandgap insulators would do as well if the technology of deposition could be worked out.

The bulk charge and the uniformity of the layers are strongly dependent on the deposition conditions. Layers of silicon nitride have been obtained with less charge, and even with opposite polarity charge, by the use of different deposition conditions and by different heat treatments.

Low-Voltage Operation

Most of the experiments described here have been performed with rather thick silicon nitride layers requiring switching voltages in the

‡ Samples prepared by A. Waxman, RCA Laboratories.
* Sample prepared by G. Stockdale, RCA Laboratories.

range 10-50 volts. Similarly, published reports on hysteresis effects in silicon nitride layers usually have employed voltages in the range 40-130 volts. The reason is that thick films, 800 Å and thicker, are less subject to breakdown by pinholes or defects in the film. Furthermore, thin films, 100-200 Å, are seldom uniform enough over device dimensions. One reason is that deposited films grow by nucleation, and it takes appreciable thickness to grow the nuclei into an even film.

On the other hand, operation of memory-transistor systems with microseconds or shorter pulses becomes impractical for a pulse height greater than about 10-20 volts, because of the requirements on the driving circuits and the large power losses. A practical memory transistor should, therefore, operate at a voltage level of about 10 volts or lower. This requires an insulator layer more free of defects than that obtained by conventional deposition.

One method, suggested and tried by A. Goodman*, would be to deposit a thin, imperfect, layer of silicon nitride. Subsequently, the wafer would be subjected to oxidation, e.g., 30 minutes in steam at 1050°C, as in conventional processing. During the oxidation treatment, pinholes would be expected to heal by the formation of oxide. It is well known that defects offer rapid diffusion paths and, therefore, would also be expected to oxidize. The oxidized areas would not contain traps and, therefore, would not contribute to the memory action, but if they were sufficiently small they might not interfere with the transistor performance.

Figure 19 shows results on a capacitor* made with 15 Å oxide, 120 Å nitride, and subsequently oxidized 12 minutes at 900°C in steam to grow thermal SiO_2 to plug up the pinholes. The capacitance-versus-voltage curves indicate switching at voltages as low as 5-10 volts, the theoretically expected values for this nitride thickness. The control units having the same thickness of nitride, but not oxidized after the nitride deposition, were all shorted. However, the oxidized units were very uneven, with most of the units shorted initially, or shorting at low voltages. Better control of this method must be found.

TRAP DENSITY IN BULK SILICON NITRIDE

When the silicon nitride is formed there is a built-in charge density that is linear with thickness and, therefore, appears to be uniformly distributed throughout the bulk. This density may be calculated from the initial capacitance-versus-voltage curve.

---

* Samples prepared by A. Goodman, RCA Laboratories.

Consider a silicon nitride layer 800 Å thick between two conducting layers, with a voltage threshold of −8 volts, as shown in Figure 15. The solution of Poisson's equation gives a charge density of

$$N = 1 \times 10^{18}\ \text{cm}^{-3}$$

and an electric field at the surface of

$$E = 2 \times 10^{6}\ \text{V/cm}.$$

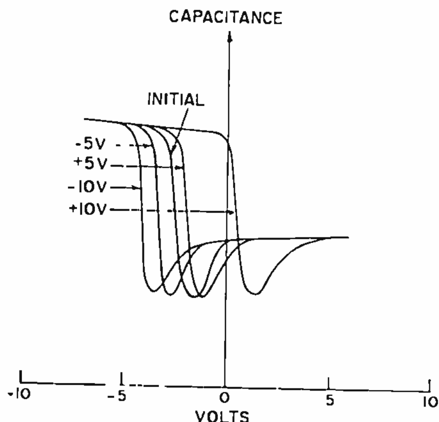

Fig. 19—Capacitance-versus-voltage curves for sample with an outer insulator of 120 Å nitride, oxidized 12 minutes at 900°C in steam.

This charge density indicates that the average distance between states, d, is about 100 Å. It is believed that this state density results from unsaturated bonds in the nitride. The density is strongly dependent on processing parameters. It has been found that heat treatment to temperatures in the range 800-1200°C reduces the state density. However, in the experiment performed, this reduction in state density is achieved at the cost of reduced memory retention.

Trap Density at the Silicon-Dioxide–Silicon-Nitride Interface

For useful operation of the memory transistor, the trap density at the interface between the silicon dioxide and the silicon nitride should be as high as possible. It must be much higher than the density of traps in the bulk of the silicon nitride derived above. The density may be calculated from the data in Figure 14. Assuming a thick nitride layer, so that the charges induced at the gate contact may be neglected, the

state density N_t per unit area is

$$N_t = \frac{\epsilon V}{d_1 q}$$

where ϵ is the dielectric constant of silicon dioxide (3.85), V is the window voltage, q is the electronic charge, and d_1 is the distance from the states to the silicon. Inserting data from Figure 14 for the thinnest oxide layer, we get

$$N_t = 2 \times 10^{14} \text{ cm}^{-2}.$$

This density corresponds to an average distance between traps of $d = 7$ Å.

Thus, since the average distance between silicon atoms in glassy silica layers is 3.0 Å, somewhat less than 50% of the silicon atoms contribute traps. Compared to this very large density, the contribution to the interface density by bulk silicon nitride states within tunneling distance from the silicon surface is negligible.

Physical Model for the Memory Mechanism

The experimental results reported above can be summarized and understood on the basis of a physical model of the memory mechanism utilizing band theory. While some of the effects observed have already been partly explained using this model, this section presents the picture in more detail. The quantitative aspects of this model are treated in a separate paper.[16] The description starts with the fundamental memory effect and then deals with second-order effects.

The band picture for the Si-SiO_2-SiN_2-Al system has been assembled using the following values for the energy levels* (see Figure 20):

The energy difference between the silicon conduction band and the silicon dioxide valence band is 4.92 eV.[17]

The energy difference between the silicon conduction-band edge and the silicon nitride valence band is 3.05 eV.[18]

---

[16] E. C. Ross and J. T. Wallmark, "Theory of Switching Behavior of MIS Memory Transistors," RCA Review, Vol. 30, p. 366, June 1969.

* A. M. Goodman, RCA Laboratories, private communication.

[17] A. M. Goodman, "Photoemission of Holes from Silicon into Silicon Dioxide," *Phys. Rev.*, Vol. 152, p. 780, 1966.

[18] A. M. Goodman, "Photoemission of Electrons and Holes into Silicon Nitride," *Appl. Phys. Letters*, Vol. 13, p. 275, 1968.

The silicon dioxide bandgap is 8 eV.[19]

The bandgap of the silicon nitride as prepared here is 5.1 eV.[18]

The electron affinity of the silicon dioxide is 1.0 eV.[20]

The vacuum work function of aluminum is 4.20 eV.[21]

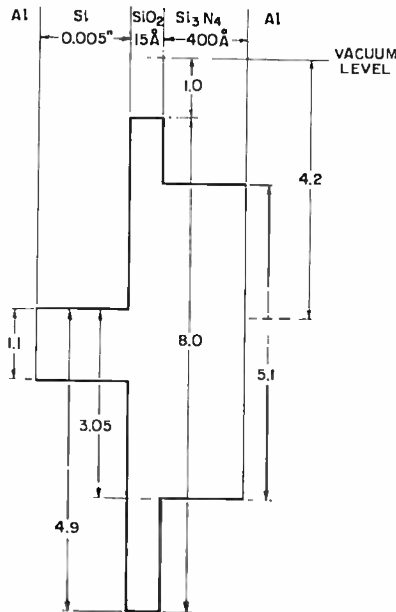

Fig. 20—Band diagram of the silicon–silicon-dioxide–silicon-nitride–aluminum system with quantitative values of the energy levels.

Fundamental Effect of Memory Storage

The fundamental effect of memory storage is illustrated in Figure 21, which shows the band picture of the silicon–silicon-dioxide–silicon-nitride system. Let us assume, initially, that each layer is ideal and that there are no states in the bulk of the materials. The only charges we need consider then are the doping atoms and the corresponding free carriers in the silicon.

To explain the memory effect, let us assume that at the silicon-

---

[19] R. Williams, "Photoemission of Electrons from Silicon into Silicon Dioxide," *Phys. Rev.*, Vol. 140, p. A569 (1965).

[20] A. M. Goodman and J. J. O'Neill, Jr., "Photoemission of Electrons from Metals into Silicon Dioxide," *J. Appl. Phys.*, Vol. 37, p. 3580 (1966).

[21] J. C. Riviere, "Contact Potential Difference Measurements by the Kelvin Method," *Proc. Phys. Soc.* (London), Vol. B70, p. 676, 1957.

dioxide-silicon-nitride interface there are states with a density of 2×10^{14} cm^{-2} at an energy level inside the forbidden band in silicon. These states may be caused by the mismatch between the silicon dioxide lattice and the silicon nitride lattice.

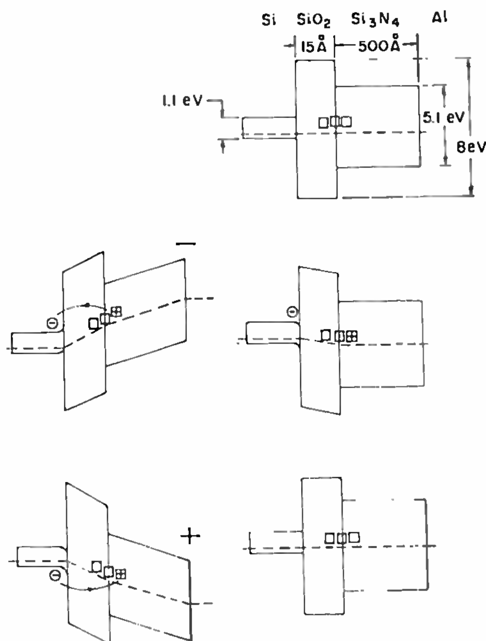

Fig. 21—Band-diagram sequence showing the fundamental effect responsible for the memory action: (a) before pulsing; (b) during a negative pulse, and after the pulse has terminated (note the positive charge in the traps); and (c) during a positive pulse and after the pulse has terminated (note that the traps end up being neutral).

In equilibrium, these states could not exchange charge with the silicon. When a large negative voltage is applied to the nitride electrode, the states are raised so that they can exchange charge with the conduction band of the silicon. Let us assume, in agreement with experimental findings, that the states are donor-like. In that case electrons will tunnel through the thin oxide layer from the states to the silicon.

If the silicon band does not bend but remains horizontal (as in Figure 22(a)) and the electron lifetime is long compared to the pulse duration, the electrons will tunnel right back again when the applied voltage is terminated. If, on the other hand, the electrons are removed from the silicon surface as they arrive, either by recombination or by transport away from the surface and into the bulk by the electric field

at the surface, the traps that have lost electrons will remain positively charged.

The time for the electrons to move a distance x into the silicon away from the interface in a constant electric field is

$$t \approx \frac{x\,\epsilon_{Si}}{\mu E_{Si_3N_4}\epsilon_{Si_3N_4}}.$$

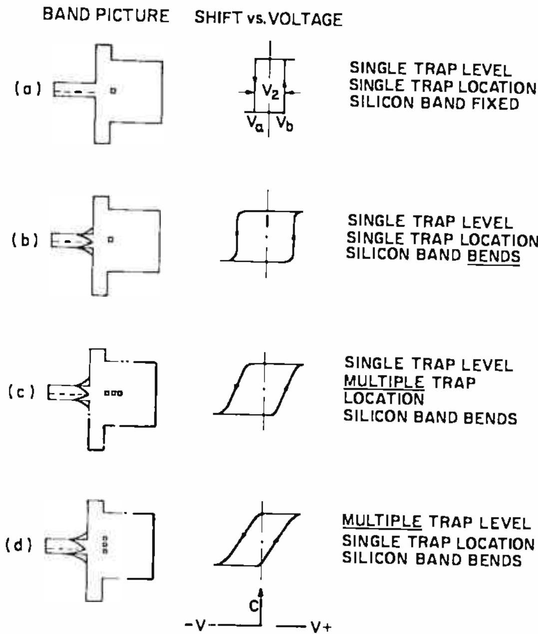

Fig. 22—Simplified summary of trap alternatives. The main features of the resulting switching hysteresis curve, similar to those shown in Figure 9, are shown for each case. Note that in (c) there is both a definite threshold and sloping flanks while (b) and (d) each have only one of these characteristics.

For $x = 50$ Å, i.e., out of tunneling range, $t = 10^{-15}$ sec, which is completely negligible for even the shortest pulses used. The maximum speed of switching is therefore set by the *RC* time constant of the surface of the silicon, and is about 1 ns.

In addition, there are usually states in the insulator bulk that can exchange charge, particularly at high voltages. These states are re-

sponsible for many second-order effects, e.g., the anomalous hysteresis observed by many investigators and discussed previously.

Single Trap Level—Silicon Band Fixed

Let us now consider different alternatives for the distribution of the states in energy and in space. First, let us consider a single trap level located only at the interface and, for simplicity, let us assume that the silicon band is fixed and does not bend at the surface. The arguments are simplest when the silicon is intrinsic and the trap level is in the middle of the band. Then the capacitance-versus-voltage curve will shift on the application of a negative voltage $-V_1$ that is just large enough to raise the trap indicated as a box in Figure 21 to the silicon conduction-band edge. The curve will remain there (the positive charge in the traps will remain constant) until a positive voltage V_1 is applied that is just large enough to lower the trap to the valence band edge of the silicon. Then the *CV* curve will shift to the position marked $-V_b$, resulting in a hysteresis loop as shown in Figure 22a.

The switching voltage V_1 is easily computed to be

$$V_1 = \frac{E_g}{2}\left(1 + \frac{\epsilon_1 d_2}{\epsilon_2 d_1}\right),$$

where ϵ_1 is the dielectric constant of silicon dioxide,

ϵ_2 is the dielectric constant of silicon nitride,

d_1 is the thickness of silicon dioxide layer,

d_2 is the thickness of the silicon nitride layer,

E_g is the bandgap of silicon.

The shift in flat-band voltage V_2, which is the width of the hysteresis loop, depends only on the stored charge, i.e., on the number N of traps charged or discharged.

$$V_2 = V_a - V_b = \frac{qNd}{\epsilon},$$

where q is the electronic charge.

Single Trap Level—Silicon Band Bends

Now let the silicon band bend under the influence of the applied voltages. The maximum band bending indicated in Figure 22b widens the forbidden band to very nearly $2E_g$. It must be remembered that the surface space-charge region in the silicon is much wider than indicated in Figure 22b (100-10,000 Å, depending on the doping level). The effect on the capacitance-versus-voltage curves is twofold. First, the voltages needed for shifting between the two flat-band voltages V_a and V_b will double. V_a and V_b, on the other hand, will not change appreciably. Second, tunneling is already possible before the trap level reaches the top of the conduction or the bottom of the valence band. However, as the surface space-charge region is very wide, the voltage needed for a partial shift is still close to V_1.

Distribution in Space of Single Trap Level—Silicon Band Bends

Now let us consider the distribution of trap levels as a function of distance from the silicon surface as indicated in Figure 22c. Such a distribution would result from slight variations in oxide thickness, and from the randomness of the disorder states. There could also be a slight diffusion of these states at the deposition temperature (700°C). Furthermore, the presence of bulk states in the silicon nitride adds to the distribution. The application of bias first brings the trap most remote from the silicon surface even with the conduction or valence bands. For these traps, tunneling then becomes possible at voltages considerably lower than $2V_1$.

A quantitative derivation of the switching voltage is given in a separate paper.[16]

Multiple Trap Level—Silicon Band Bends

Now let us consider a set of traps distributed in energy as shown in Figure 22d. This distribution disagrees with the measured results in two respects. First, as all traps are at the same distance from the silicon surface, there should be little time dependence on the switching voltage. Low voltages should result in nearly the same time constant as the high voltages because only the shape, not the width or height, of the barrier would change. This does not agree with the measured results shown in Figure 9. Second, the minimum voltage for switching should be lower than that found; actually, it should be close to zero

for a distribution all the way to the silicon band edge. For these reasons, the main trap distribution is in space, not in energy, although a small distribution in energy superimposed on the distribution in space cannot be ruled out and appears likely. A quantitative justification is presented in a separate paper.[16]

ACKNOWLEDGMENT

This work was performed in the Computer Research Laboratory under the guidance of R. Shahbender and under the direction of J. Rajchman.

The assistance of D. Maurizi, H. James and R. Gilchrist in device fabrication is gratefully acknowledged. Discussions with J. R. Burns on the read-only memory, with G. Briggs on general memory applications, and with E. C. Ross on various aspects of the device were very helpful. Various techniques were contributed by D. Flatley, A. Goodman, W. Kern, W. H. Schilp, G. Stockdale, and A. Waxman.

THEORY OF THE SWITCHING BEHAVIOR OF MIS MEMORY TRANSISTORS

BY

E. C. ROSS* AND J. T. WALLMARK†

Summary—The available theories to explain the switching behavior of MIS memory transistors have all dealt with the specific case in which the silicon dioxide layer adjacent to the silicon surface is sufficiently thick (> 50Å) that direct tunneling of charge between the interface traps and the silicon is negligible. This paper presents a theory to explain the switching behavior of MIS memory transistors in which direct tunneling is the principal mechanism of charge transfer. The theory predicts that charge transfer in such a device is logarithmically dependent on the applied gate pulse duration and exponentially dependent on the amplitude of the applied gate pulse. The theory is shown to be in good agreement with experimental results.

INTRODUCTION

A new memory element has recently emerged that utilizes the hysteresis effects observed in connection with certain insulators on MOS field-effect transistors.[1-3] In more conventional approaches to the application of transistors to provide information storage, the transistors, which exhibit no hysteresis, are combined into a circuit that does exhibit hysteresis.[4] The memory function then, is a property of the circuit. In the memory behavior described in this paper, the transistors, themselves, have memory; each transistor is capable of storing one "bit" of information. A quantitative treatment of these MIS memory transistors is presented.

---

* RCA Laboratories, Princeton, N. J.

† Formerly RCA Laboratories, Princeton, N. J.; now at Chalmers University, Göteborg, Sweden.

[1] H. C. Pao and M. O'Connell, "Memory Behavior of an MNS Capacitor," *Appl. Phys. Letters*, Vol. 12, p. 260, 15 April 1968.

[2] D. Kahng and S. M. Sze, "A Floating Gate and Its Application to Memory Devices," *Bell. Syst. Tech. Jour.*, Vol. 46, p. 1288, July-Aug. 1967.

[3] J. T. Wallmark and J. H. Scott, Jr., "Switching and Storage Characteristics of MIS Memory Transistors," *RCA Review*, Vol. 30, p. 335, June 1969.

[4] J. F. Allison, F. P. Heiman, and J. R. Burns, *IEEE Jour. Solid-State Circuits*, Vol. SC-2, p. 208, 1967.

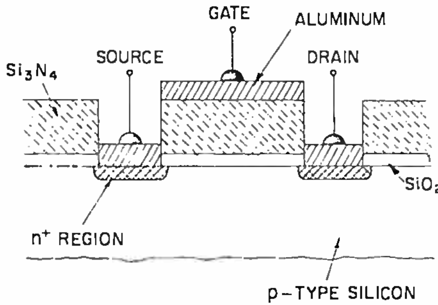

Fig. 1—Schematic illustration of a metal-nitride-oxide-silicon memory transistor.

Physical Model of the Memory Effect

The memory element is a field-effect transistor in which the gate insulator is a sandwich structure of two insulating layers. The layer closest to the silicon is silicon dioxide, and the top layer is silicon nitride (see Figure 1).

It has been shown that a heavy concentration of donor-type traps exists at the interface between these two layers; these traps can communicate with the silicon when a field is applied across the insulators.[3] The operation of an n-channel, enhancement-type device is illustrated in Figure 2. As indicated in Figure 2(a), the traps are neutral when filled. If the gate is held at ground potential, no inversion layer is formed in the channel region, and the transistor conducts no drain

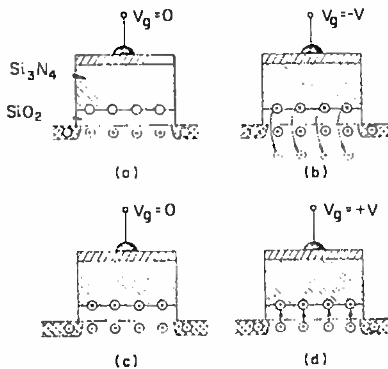

Fig. 2—Schematic illustration of the state of the trapping centers and the free carriers at the silicon surface for (a) traps neutral, gate potential at ground; (b) traps being charged, gate potential at $-V$; (c) traps charged, gate potential at ground; (d) traps being discharged, gate potential at $+V$.

current. If a large negative potential is now applied to the gate, as shown in Figure 2(b), the electrons in the traps are transferred to the silicon, leaving the trapping centers positively charged. If the gate is now held at ground potential, an inversion layer is induced in the channel region by the field associated with the positive charge at the traps, and drain current can flow. This condition is shown in Figure 2(c). The effect is reversed by applying a large positive potential to the gate, as shown in Figure 2(d). Electrons return to the traps and the positive charge is neutralized. Application of ground potential to the gate now results in the condition shown originally in Figure 2(a).

The charge-transfer mechanisms in MIS memory transistors have been investigated by other workers[5,6] for the specific case where the thickness of the silicon-dioxide layer is 50 Å or greater. This restriction ensures that direct tunneling between the traps and the silicon can be neglected. The charge transfer in this case results from Fowler–Nordheim tunneling into the conduction band of the silicon dioxide[7] and/or bulk limited conduction in the silicon nitride.[8,9] The disadvantage of such an approach is primarily that only relatively small currents can flow, even for very large fields. The switching speed or the storage time of transistors fabricated in this configuration must be compromised.

An alternative approach is to make the thickness of the silicon dioxide layer less than ≈ 35 Å.[10] In this case, tunneling can occur directly between the silicon and the traps at the silicon-dioxide–silicon-nitride interface. The advantage of this approach is that the current that flows for a given applied field can be made relatively large. Thus, a device that switches in nanoseconds can be fabricated.

The electron energy-band diagram of the physical model that is used to explain the switching characteristics of such a transistor—in this case an n-channel unit—is shown in Figure 3. Initially, the

---

[5] D. Frohman-Bentechkowsky and M. Lenzlinger, Int. Electron Devices Mtg., Washington, D. C., Oct. 1968.

[6] F. A. Sewell, Jr., H. A. R. Wegener, and E. T. Lewis, "Charge Storage Model for Variable Threshold FET Memory Element," *Appl. Phys. Letters*, Vol. 14, p. 45, 15 Jan. 1969.

[7] M. Lenzlinger and E. H. Snow, "Fowler-Nordheim Tunneling into Thermally Grown SiO_2," *Jour. Appl. Phys.*, Vol. 40, p. 278, Jan. 1969.

[8] S. M. Sze, "Current Transport and Maximum Dielectric Strength of Silicon Nitride Films," *Jour. Appl. Phys.*, Vol. 38, p. 2951, June 1967.

[9] G. A. Brown, W. C. Robinette, Jr., and H. G. Carlson, *Jour. Electrochem. Soc.*, Vol. 115, p. 948, 1968.

[10] F. P. Heiman and G. Warfield, "The Effects of Oxide Traps on the MOS Capacitance," *IEEE Trans. on Electron Devices*, Vol. ED-12, p. 167, April 1965.

transistor has a threshold voltage of about −5 V, indicating that positive charges are stored in the insulator. If, for simplicity, these initial charges are replaced by an equivalent charge at the silicon-dioxide–silicon-nitride interface, the band diagram of Figure 3(a) results. It is assumed that no charges are found in the silicon dioxide.

When a negative voltage is applied to the gate, the trap level (indicated in Figure 3 by squares and assumed to be monoenergetic) is

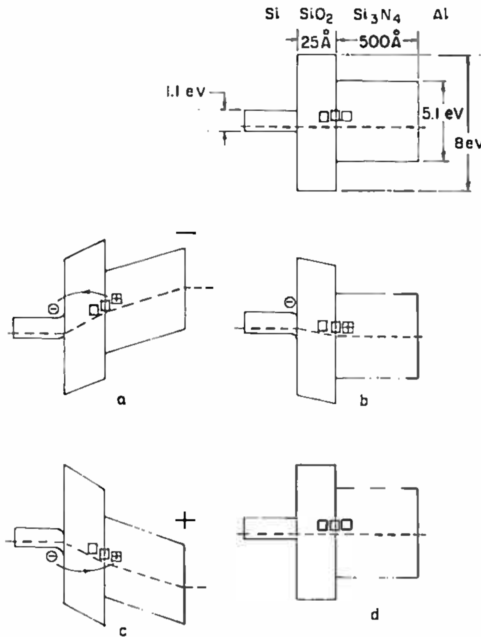

Fig. 3—Band diagram of switching behavior: (a) traps being charged by application of negative gate potential; (b) channel inverted at $V_g = 0$; (c) traps being discharged by application of positive gate potential; (d) channel depleted at $V_g = 0$.

lifted in energy relative to the silicon. For a moderate voltage, traps deep in the nitride have sufficient energy to tunnel through the oxide into the silicon conduction band; and for a large voltage, traps closer to the interface also can tunnel into the silicon conduction band. Electrons can then tunnel from the traps to the silicon as indicated in Figures 3(a) and 3(b). Tunneling from the traps to the silicon conduction band is possible when the trap is less than ≈35 Å from the silicon. This distance defines the smallest voltage at which switching starts. The voltage at which switching saturates is assumed to be set by the condition that the traps closest to the silicon surface are lifted in energy and become even with the silicon conduction band.

For positive gate voltages, the process is similar, but now the traps communicate with the valence band of the silicon. This is illustrated in Figures 3(c) and 3(d).

As described elsewhere,[3] very large gate voltages result in the injection of electrons into the silicon nitride conduction band or conduction in the silicon nitride or both. Injection occurs from the gate contact at negative gate voltages, and by Fowler–Nordheim tunneling from the silicon at positive gate voltages. The physical model described above is only valid for applied gate voltages that are sufficiently small to avoid these injection mechanisms.

Experimental measurements on devices operating through this mechanism are discussed in a paper by Wallmark and Scott.[3] The experimental results shown in Figure 9 of their paper are replotted in a more convenient form in Figure 4, which shows the pulse width versus shift in the capacitance-versus-voltage curve, with pulse amplitude as a parameter. The lines drawn through the data are extrapolations of the large data shift back to the origin, and will be useful in the following sections.

Derivation of the Switching Characteristics

A simple theory, which is in good agreement with the form of the experimental results shown in Figure 4, can be derived based on the model illustrated in Figure 5. The model assumes a monoenergetic trap level, distributed spatially at or near the interface between the silicon dioxide and the silicon nitride. The traps are assumed to extend into the oxide and into the nitride from the interface, as indicated in Figure 6, and to be located energetically in the forbidden bandgap of the silicon. When a field is applied to the insulator, the trap level is shifted in energy, and tunneling is possible between the silicon and trap states in the nitride at distance x greater than x_0. All charge transfer is assumed to be through direct tunneling between trap states in the composite insulator and the silicon conduction and valence bands. The following notation is employed for a given gate voltage:

$T_1(x,t)$ = transition rate of charges from the traps to the silicon conduction band, per unit volume, per unit time,

$N_1(x,t)$ = concentration per unit volume of filled trap states,

$P_1(x,t)$ = transition probability per unit time for an electron from traps at a distance x from the silicon to the silicon conduction band,

$Q_1(t)$ = total amount of charge transferred to the silicon per unit area after time t has elapsed.

All results are valid for charge exchange from the silicon valence band to the traps if the subscripts are changed from 1 to 2 and the words "filled states" are replaced by "empty states".

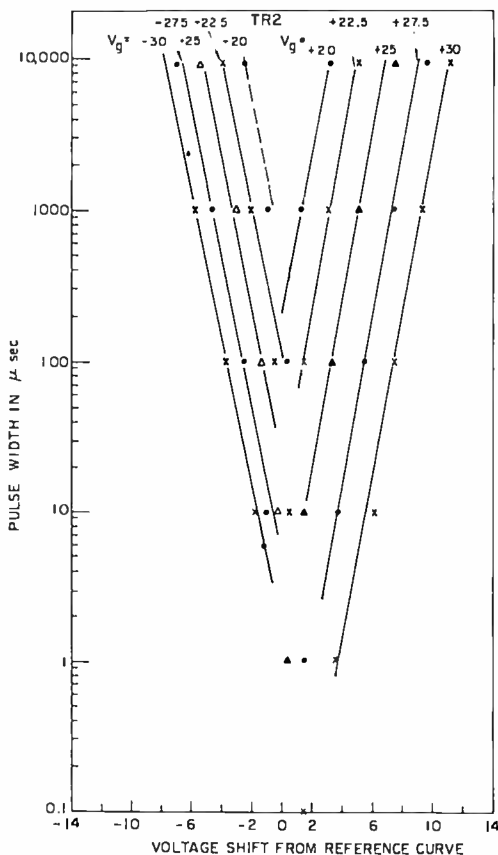

Fig. 4—Experimental data showing pulse duration versus flat-band voltage shift, with pulse amplitude as a parameter (standard MOS field-effect transistor, except for gate insulator of 500 Å SiN_2 over 25 Å of SiO_2).

By definition,

$$T_1(x,t) = N_1(x,t)P_1(x,t) , \tag{1}$$

and from charge conservation,

$$T_1(x,t) = -\frac{dN_1(x,t)}{dt} . \tag{2}$$

We equate the right-hand sides of Equations (1) and (2) and obtain

$$\frac{dN_1(x,t)}{dt} = -N_1(x,t)P_1(x,t) . \tag{3}$$

We now make the assumption that the transition probability for an individual electron at distance x is independent of time. Implicit in this assumption is that the transfer of charge does not appreciably

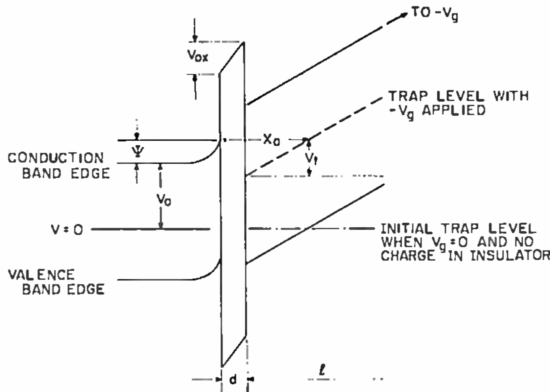

Fig. 5—Band diagram of memory transistor with negative gate potential applied.

affect the electric field strength in the oxide. We then obtain the usual results for constant transition probabilities, with the solution of Equation (3), as

$$N_1(x,t) = N_1(x,0) \exp[-P_1(x)t] . \tag{4}$$

We assume that the functional form of the transition probability is similar to that for tunneling through a rectangular barrier.[11] The transition probability is then taken to be of the form

$$P_1(x) = P_1(0) \exp[-x/\lambda] , \tag{5}$$

where $P_1(0)$ is a constant, and λ is an effective constant that depends on the details of the potential barrier. An expression for λ is given by

[11] E. Merzbacher, *Quantum Mechanics*, p. 93, John Wiley and Sons, Inc., New York, 1961.

$$\lambda = \frac{h}{[4\pi\sqrt{2m^*E}]}, \tag{6}$$

where h is Planck's constant, m^* is the electron effective mass inside the barrier, and E is the effective magnitude of the energy barrier. When Equation (6) is evaluated with the values $E = 3$ eV and $m^* = 0.4m_o$, where m_o is the free electron mass,[7] λ is estimated to be of the order 0.8 Å.

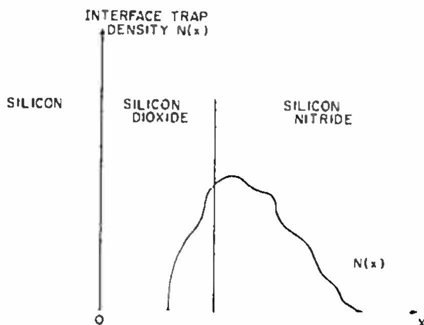

Fig. 6—Schematic representation of the spatial distribution of the interface traps.

The transition rate from the entire distribution of traps for a silicon nitride thickness l is

$$\pi_1(t) \equiv \int_{x=x_0}^{l} T_1(x,t)\,dx\,. \tag{7}$$

If we substitute Equations (1), (4), and (5) in Equation (7), it becomes

$$\pi_1(t) = P_1(0)\int_{x=x_0}^{l} N_1(x,0)\exp\left[-\frac{x}{\lambda} - P_1(0)\,t\exp\left(-\frac{x}{\lambda}\right)\right]dx\,. \tag{8}$$

Since λ is of the order 0.8 Å, and l for the samples used is 500 Å, the integrand converges sufficiently rapidly to zero to replace the upper limit of the integration by infinity. Also, the exponential-to-exponential

dependence on x of one factor of the integrand suggests that the spatial distribution of the traps can be considered constant as a first approximation (N_1 independent of x) and pulled outside the integral. If this is done, Equation (8) can be integrated in closed form to obtain

$$\pi_1(t) = N_1(x_o,0)\lambda \left[\frac{1 - \exp[-t/t_o]}{t}\right], \tag{9}$$

where we have made the substitution

$$t_o \equiv [P_1(0) \exp[-x_o/\lambda]]^{-1}. \tag{10}$$

The total charge transferred at time t is

$$Q_1(t) = q \int_0^t \pi_1(t)\,dt. \tag{11}$$

When Equation (9) is substituted into Equation (11) and the integration is performed, the result is

$$Q_1(t) = qN_1(x_o,0)\lambda[0.577 + \ln(t/t_o) - E_i(-t/t_o)], \tag{12}$$

where $E_i(-t/t_o)$ is a tabulated function that goes rapidly to zero[12] for $t > t_o$.

The charge transferred is simply related to the shift in the flat-band voltage of the capacitance versus gate voltage characteristic V_s by the expression

$$Q_1(t) = \frac{\epsilon_n V_s(t)}{l}, \tag{13}$$

where ϵ_n is the dielectric constant of the silicon nitride.

Finally, for times such that $t > t_o$, we obtain the expression

$$V_{s_1}(t) = \frac{qN_1(x_o,0)\lambda l}{\epsilon_n}[0.577 + \ln(t/t_o)], \tag{14}$$

[12] Jahnke-Emde-Lösch, *Tables of Higher Functions*, p. 17, McGraw-Hill Book Co., Inc., New York, 1960.

which predicts that the flat-band shift obtained for a particular applied voltage pulse will depend logarithmically on the pulse duration. This is in good agreement with the experimental data shown in Figure 4.

Comparison of Theory with Experiment

Representative values for the physical parameters are now obtained. The slopes of the experimental curves in Figure 4 for $t > t_o$ are obtained by differentiating Equation (14).

$$\frac{\partial V_s}{\partial \ln (t)} = \frac{qN_1(x,0)\lambda l}{\epsilon_n}. \tag{15}$$

We evaluate Equation (15) using the experimentally determined slopes from Figure 4, $l = 500$ Å, and $\epsilon_n = 7.0\epsilon_o$ [9] (where ϵ_o is the permittivity of free space); the result is

$$qN_1(x_o,0)\lambda = 1.2 \times 10^{-3} \text{ coulomb/m}^2 \tag{16}$$

A similar calculation for the case of a positive gate voltage gives

$$qN_2(x_o,0)\lambda = 1.0 \times 10^{-3} \text{ coulomb/m}^2 . \tag{17}$$

Since N_1 and N_2 are about equal at $(x_o,0)$, the implication of the above calculations is that λ, as a crude first approximation, is nearly the same for both polarities of gate potential.

If we extrapolate Equation (14) back to the time t' such that $V_s(t') = 0$, t' and t_o are related by the simple expression

$$\ln (t'/t_o) = -0.577 . \tag{18}$$

We now substitute Equation (10) for t_o into Equation (18), and obtain

$$\ln t' = \frac{x_o}{\lambda} - \ln [P_1(0)] - 0.577 . \tag{19}$$

In order to derive the dependence of $\ln t'$ upon the applied gate voltage, we must find x_o as a function of gate voltage. It should be noted that we are specifically neglecting the voltage dependences of the barrier height and the final density of states into which the traps are emptying. This is justified by the relatively slight voltage dependence

of these parameters with respect to x_o. A simple calculation, using the energy-band diagram shown in Figure 5, gives the result for negative gate voltages

$$x_o = \frac{V_o}{E_n} - \frac{V_{ox}}{E_n} + d , \tag{20}$$

where V_o is the difference in voltage between the traps and the silicon conduction band at flat-band condition and no charge in the traps, V_{ox} is the potential drop across the silicon dioxide, E_n is the electric field in the silicon nitride, and d is the thickness of the silicon dioxide.

From displacement continuity,

$$E_n = \frac{\epsilon_{ox}}{\epsilon_n} E_{ox} + \frac{Q_1}{\epsilon_n} , \tag{21}$$

where ϵ_{ox} is the dielectric constant of silicon dioxide, ϵ_n is the dielectric constant of silicon nitride, E_{ox} is the electric field in the silicon dioxide, and Q_1 is the charge stored in the traps. The convention E_n positive for negative gate potential is used.

The summation of voltage drops across the structure gives

$$V_g = V_n + V_{ox} + \psi , \tag{22}$$

where V_g is the applied gate voltage, V_n is the potential across the silicon nitride, V_{ox} is the potential across the silicon dioxide, and ψ is the potential from the silicon surface to the bulk.

Substitution of Equation (21) into Equation (22) gives, after a little manipulation,

$$V_{ox} = \frac{(V_g - \psi)}{\left(1 + \dfrac{\epsilon_{ox} l}{\epsilon_n d}\right)} + \frac{Q_1}{\left(\dfrac{\epsilon_{ox}}{d} + \dfrac{\epsilon_n}{l}\right)} . \tag{23}$$

The electric field in the silicon nitride can then be expressed in the form

$$E_n = -\frac{(V_g - \psi)}{\left(l + \dfrac{\epsilon_n}{\epsilon_{ox}} d\right)} + \frac{Q_1}{\left(\epsilon_n + \epsilon_{ox} \dfrac{l}{d}\right)} . \tag{24}$$

Q_1 can be found experimentally from the relation

$$Q_1 = -\frac{V_s}{l} \times 0.64 \text{ coulomb/m}^2 , \tag{25}$$

where V_s is the flat-band shift in volts and l is in Å.

The charge stored in our experimental sample at saturation for negative gate voltage is 1.2×10^{-2} coulomb/m², which corresponds to 7.5×10^{12} electronic charges/cm² of surface area. By substitution of this value for Q_1 and known values for the physical constants into Equation (24), it can be shown that for our experimental condition, Equation (24) can be approximated with less than a 3% error as

$$E_n = -\frac{(V_g - \psi)}{\left(l + \frac{\epsilon_n}{\epsilon_{ox}} d\right)} . \tag{26}$$

For negative gate polarities, the switching characteristics are taken starting from a state in which the charge in the traps is nearly neutralized. During the initial switching period, the charge in the traps is small enough that the term containing Q_1 in Equation (23) can be neglected with respect to the other term. Under these conditions, Equation (20) can be approximated as

$$x_o = \frac{V_o\left(l + \frac{\epsilon_n d}{\epsilon_{ox}}\right)}{V_g - \psi} - d\left(\frac{\epsilon_n}{\epsilon_{ox}} - 1\right) \tag{27}$$

Substitution of Equation (27) into Equation (19) gives

$$\ln t' = \frac{V_o\left(l + \frac{\epsilon_n d}{\epsilon_{ox}}\right)}{\lambda[V_g - \psi]} + C , \tag{28}$$

where C is a constant.

A similar calculation for the case of positive gate voltage gives the result

$$\ln t' = \frac{\left(1.1 + \frac{Q_R d}{\epsilon_{ox}} - V_o\right)\left(l + \frac{\epsilon_n d}{\epsilon_{ox}}\right)}{\lambda (V_g - \psi)} + C', \tag{29}$$

where C' is a constant, Q_R is the charge in the traps at the reference state, and the bandgap of silicon is taken as 1.1 eV.

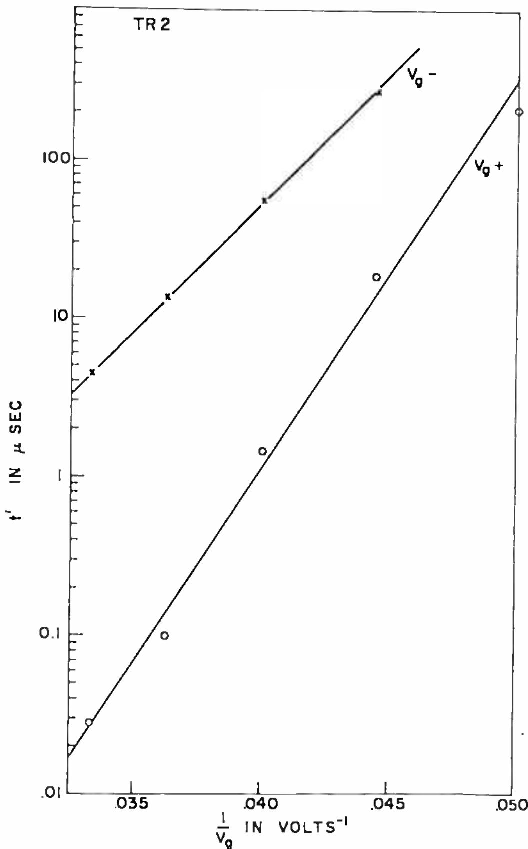

Fig. 7—Experimental data showing t' (see text) versus V_g^{-1} for positive and negative gate potentials (same device as for Figure 4).

Equations (28) and (29) predict that $\ln t'$ should vary linearly with $(V_g - \psi)^{-1}$ for both gate polarities. A plot of the experimental values of t' from Figure 4 versus $(V_g - \psi)^{-1}$ for both gate polarities is shown in Figure 7.

From the slopes of the experimental curves in Figure 7 and Equations (28) and (29), we obtain the relationships

$$\left.\frac{V_o}{\lambda}\right|_{-V_g} = 0.7 \text{ eV/Å} \tag{30}$$

and

$$\left.\frac{2.0 - V_o}{\lambda}\right|_{+V_g} = 1.0 \text{ eV/Å} \tag{31}$$

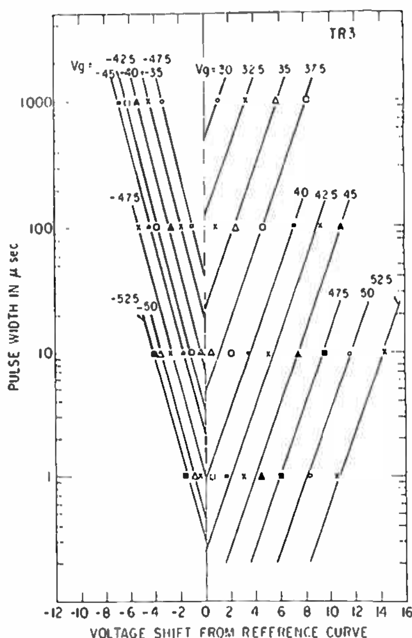

Fig. 8—Experimental data on devices with oxide thickness of 15 Å and silicon nitride thickness of 820 Å, showing pulse duration versus flat-band voltage shift, with pulse amplitude a parameter.

If we now use the condition that λ is the same for both gate voltage polarities, Equations (30) and (31) can be solved simultaneously to find that representative values

$$\lambda = 1 \text{ Å}$$
$$V_o = 0.8 \text{ eV} \tag{32}$$

A second set of experimental samples was prepared with oxide thickness 15 Å and silicon nitride thickness 820 Å. The experimental

data for one of these units is shown in Figures 8 and 9. The values for λ and V_o obtained from this data are

$$\lambda = 1 \text{ Å}$$
$$V_o = 0.5 \text{ eV} \tag{33}$$

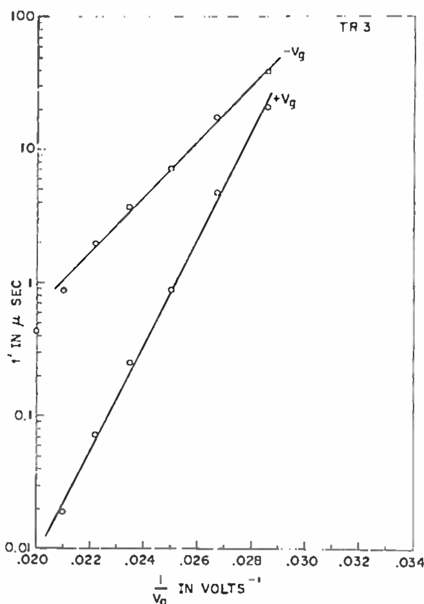

Fig. 9—Experimental data (same device as for Figure 8), showing t' (see text) versus V_g^{-1} for positive and negative gate potentials.

The density of the traps can now be estimated from Equations (16) and (17), using the value of 1 Å for λ. The result is

$$N \approx 6 \times 10^{19} \text{ cm}^{-3} . \tag{34}$$

The amount of positive charge in the traps at the ON state can be estimated in the following way. The application of -22.5 V for 1 second will empty the traps within $\approx$35 Å of the silicon. Since the oxide thickness is 25 Å, the traps within $\approx$10 Å of the silicon-dioxide–silicon-nitride interface are emptied. From the density of traps in Equation (34), the number of traps emptied is about 6×10^{12} cm^{-2}. This is in good agreement with the experimental value of 7.5×10^{12} cm^{-2}, which is found by the shift in the capacitance-versus-voltage characteristics.

The values of the physical constants that were determined in this section are consistent with the values that are expected or measured, and demonstrate the applicability of the switching theory to the experimental observations.

CONCLUSIONS

We have presented a simple switching theory to explain the behavior of MIS memory transistors in which direct tunneling between the interface traps and the silicon is permitted. The theory predicts that the shift in the flat-band voltage for a given applied potential is proportional to the logarithm of the time for which the potential is applied. It also predicts that the switching speed of the transistor is exponentially dependent upon the amplitude of the applied potential.

ACKNOWLEDGMENT

The authors are indebted to I. Lundström for bringing Reference (13) to their attention, and to A. M. Goodman for a critical reading of the manuscript.

RCA Technical Papers

First Quarter, 1969

"Amplitude Modulation of Microwave Signals Using Transferred-Electron Diodes," F. Sterzer, *Proc. IEEE* (Letters) (January) 1969

"An Approximate Theory of Skin-Effect Acoustic Generation in Conductors," P. D. Southgate, *Jour. Appl. Phys.* (January) 1969

"Conductivity of Superconducting Tin Films at 20 GHz," R. V. D'Aiello and Coauthor, *Jour. Appl. Phys.* (January) (Communications) 1969

"Dispersion-Corrected Three-Wavelength Laser Heterodyne Measurement of Plasma Densities," C. S. Liu and Coauthors, *Jour. Appl. Phys* (January) 1969

"Frequency Modulation of Three-Terminal Gunn Devices by Optical Means," F. P. Califano, *Trans. IEEE GED* (Correspondence) (January) 1969

"A New Electric Field Controlled Reflective Optical Storage Effect in Mixed Liquid Crystal Systems," G. H. Heilmeier and J. E. Goldmacher, *Proc. IEEE* (January) 1969

"A Note on Integral Equations and Wolf's Theorem," A. A. Clark and R. F. Barry, *Trans. IEEE GAES* (Correspondence) (January) 1969

"Optical and EPR Studies of Photochromic $SrTiO_3$ Doped with Fe/Mo and Ni/Mo," B. W. Faughnan and Z. J. Kiss, *IEEE Jour. Quantum Electronics* (January) 1969

"Photochromic Materials for Quantum Electronics," Z. J. Kiss, *IEEE Jour. Quantum Electronics* (January) 1969

"Physical Basis of Noncatastrophic Degradation in GaAs Injection Lasers," H. Kressel and N. E. Byer, *Proc. IEEE* (January) .. 1969

"Signal Processors and Accuracy of Three-Beam Monopulse Tracking Radar," P. Z. Peebles, Jr., *Trans. IEEE GAES* (January) .. 1969

"Stable Space-Charge Layers Associated with Bulk, Negative Differential Conductivity: Further Analytic Results," M. A. Lampert, *Jour. Appl. Phys.* (January) 1969

"Molecular Theory of Flow Alignment of Nematic Liquid Crystals," W. Helfrich, *Jour. Chem. Phys.* (1 January) 1969

"Critical-Point Behavior of Classical Heisenberg Ferrimagnets," S. Freeman and P. J. Wojtowicz, *Phys. Rev.* (10 January) 1969

"Determination of e/h, Using Macroscopic Quantum Phase Coherence in Superconductors. I. Experiment," B. N. Taylor and Coauthors, *Phys. Rev.* (10 January) 1969

"An Algorithm for Finding the Reachability Matrix of a Directed Linear Graph," S. H. Unger, *Trans. IEEE GCT* (Correspondence) (February) 1969

"The Effect of a Field-Independent Polarization Discontinuity on Heterojunction Characteristics," R. M. Moore, *Trans. IEEE GED* (February) 1969

"A Flexible Approach to Emitter-Coupled Logic Arrays," M. V. D'Agostino and A. Feller, *IEEE Jour. Solid-State Circuits* (February) 1969

"High Efficiency X-Band Gunn Oscillators," F. P. Califano, *Proc. IEEE* (Letters) (February) 1969

"Impact Ionization of Filled Traps in Cadmium Sulfide," M. Simhony and R. W. Williams, *Jour. Appl. Phys.* (February) 1969

"Loudspeaker Compensation Using Integrated Circuits," L. B. Shulakewych and Coauthor, *Trans. IEEE GBTR* (February) 1969

"Microwave Power Transistors," H. C. Lee, *Microwave Jour.* (February) 1969

"The Performance of High-Gain First-Dynode Photomultipliers," G. A. Morton, H. M. Smith, Jr., and H. R. Krall, *Trans. IEEE GNS* (February) 1969

"An SCR Horizontal-Sawtooth-Current and High-Voltage Generator for Magnetically Deflected Picture Tubes," W. F. Dietz, *Trans. IEEE GBTR* (February) 1969

"Switching-Device Requirements for a New Horizontal-Deflection System," D. E. Burke, *Trans. IEEE GBTR* (February) 1969

"A Well-Type Ge(Li) Detector," P. P. Webb and Coauthors, *Trans. IEEE GNS* (February) 1969

"Optical-Rotatory Power and Linear Electro-Optic Effect in Nematic Liquid Crystals of p-Azoxyanisole," R. Williams, *Jour. Chem. Phys.* (1 February) 1969

"No Newcomer," J. A. Collins, *Electronics* (Readers Comment) (February 3) 1969

"Anomalous Population Distributions in an Optically Excited Metastable Level in $CaF_2:Tm^{2+}$," C. H. Anderson and E. S. Sabisky, *Phys. Rev.* (10 February) 1969

"Anisotropy of the Optical Constants and the Band Structure of Graphite," D. L. Greenaway, G. Harbeke, and Coauthors, *Phys. Rev.* (15 February) 1969

"Direct Electromagnetic Generation of Transverse Acoustic Waves in Metals," R. C. Alig, *Phys. Rev.* (15 February) 1969

"COS/MOS: The Best of Both Worlds," G. B. Herzog, *Electronics* (February 17) 1969

"Avalanche Diodes as UHF and L-Band Sources," K. K. N. Chang, *RCA Review* (March) 1969

"A Broadband High-Gain L-Band Power Amplifier Module," R. L. Bailey and J. R. Jasinski, *RCA Review* (March) 1969

"Close Confinement Gallium Arsenide P-N Junction Lasers With Reduced Optical Loss at Room Temperature," H. Kressel and H. Nelson, *RCA Review* (March) 1969

"Electronic Boresight Shift in Space-Borne Monopulse Systems," H. Honda, *RCA Review* (March) 1969

"Large-Signal Transit-Time Effects in the MOS Transistor," J. R. Burns, *RCA Review* (March) 1969

"Multielement Self-Scanned Mosaic Sensors," P. K. Weimer, W. S. Pike, G. Sadasiv, F. V. Shallcross, and L. Meray-Horvath, *IEEE Spectrum* (March) 1969

"On Narrow-Band LC70 MHz IF Filters," H. K. H. Yee, *Proc. IEEE* (Letters) (March) 1969

"Optimum Shapes for Inductors," B. Astle, *Trans. IEEE GPMP* (March) 1969

"Ph.D. Shortage," S. S. Perlman, *IEEE Spectrum* (Forum) (March) 1969

"A Potential Solid-State Flying-Spot Scanner," J. I. Pankove and A. R. Moore, *RCA Review* (March) 1969

"Resolution Limitations of Electromagnetically Focused Image-Intensifier Tubes," I. P. Csorba, *RCA Review* (March) 1969

"Signal-to-Noise Ratio Requirements of Filtered Biphase Channels," C. Devieux, *Trans. IEEE GAES* (Correspondence) (March) 1969

"The Status of Threshold Logic," R. O. Winder, *RCA Review* (March) 1969

"Stepped-Scanned Ring Array," J. Epstein and O. M. Woodward, *RCA Review* (March) 1960

"Trade Secrets," E. W. Herold, *IEEE Spectrum* (Forum) (March) 1969

"Exchange Interactions in $Mn[Sc_2]S_4$," P. J. Wojtowicz, L. Darcy, and M. Rayl, *Jour. Appl. Phys.* (1 March) 1969

"Exchangestriction in $CdCr_2S_4$ and $CdCr_2S_4$," H. Pinch and Coauthors, *Jour. Appl. Phys.* (1 March) 1969

"Unique Behavior of Seebeck Coefficient in N-Type $CdCr_2Se_4$," A. Amith and G. L. Gunsalus, *Jour. Appl. Phys.* (1 March) ... 1969
"Missing in Action," A. M. Durham, *Electronics* (Readers Comment) (March 3) 1969
"AC Field-Induced Flux Jumps in Nb_3Sn," D. A. Gandolfo and Coauthors, *Jour. Appl. Phys.* (15 March) 1969
"Computer Solutions of Lorentz-Field Amplification in a Bounded Semiconductor Medium," J. R. Golden and K. K. N. Chang, *Jour. Appl. Phys.* (15 March) 1969
"Lattice Dynamics and Second-Order Raman Spectrum of NaF," J. P. Russell and Coauthors, *Phy. Rev.* (15 March) 1969
"Scattering of Highly Focused Kilovolt Electron Beams by Solids," R. W. Nosker, *Jour. Appl. Phys.* (15 March) 1969
"Cryoelectric Memories: Best Hope for Large and Fast Storage Units," R. A. Gange, *Electronics* (March 17) 1969
"Microwave Conductivity of Granular Aluminum Films in the Superconducting Transition Region," R. V. D'Aiello and Coauthor, *Phy. Rev. Letters* (17 March) 1969
"Propagation of Strong-Field Electromagnetic Waves Through Plasmas Near the Electron Cyclotron Frequency," M. P. Bachynski and B. W. Gibbs, *Phy. Rev. Letters* (24 March) .. 1969

Patents Issued to RCA Inventors

First Quarter 1969

January

3,419,950 Method of Making a Vapor Device, *William B. Hall.*
3,420,534 Phonograph Pickup, *Michael E. Miller.*
3,420,707 Deposition of Niobium Stannide, *Joseph John Hanak.*
3,420,952 Non-Random Field Shift Apparatus for a Television Waveform Monitor, *Leonard J. Baun.*
3,420,954 Signal Translating System, *Henry M. Bach, Jr.*
3,420,991 Error Detection System, *Andrew T. Ling.*
3,421,098 Signal Translating System, *Michael S. Fisher.*
3,421,100 Direct Coupled Amplifier Including Two-Stage Automatic Gain Control, *Kiamil Giontzeneli.*
3,421,101 Broad Band High Gain Video Amplifier, *Laurance C. Drew and Harold F. King.*
3,421,938 Method of Fabricating Improved Solderable Lands, *George W. Leck.*
3,422,240 Microwave Oven, *William N. Parker*
3,422,369 Oscillator Using a Transistor as Voltage Controlled Capacitance, *Thomas J. Campbell.*
3,422,420 Display Systems, *Robert J. Clark.*
3,422,425 Conversion from NRZ Code to Self-Clocking Code, *John A. Vallee.*
3,423,525 Line-Select Apparatus for a Television Waveform Monitor, *Leonard J. Baun.*
3,423,536 Automatic Stereo Switching and Indicating Circuit, *Donald J. Snyder.*
3,423,621 Color Picture Display Containing a Red-Emitting Europium-Activated Yttrium Oxysulfide Phosphor, *Martin R. Royce.*
3,423,630 Retrace Driven Deflection Circuit with SCR Switch, *John Brewer Beck.*
3,423,650 Monolithic Semiconductor Microcircuits with Improved Means for Connecting Points of Common Potential, *Gene Cohen.*
3,423,654 Bistable Ferroelectric Field Effect Device, *George H. Heilmeier and Philip M. Heyman.*
3,432,725 Remote Control System, *Leopold A. Harwood.*
3,423,756 Scanning Antenna Feed, *Peter Foldes.*
3,424,866 Television Synchronizing Delay Compensation System, *Jarrett L. Hathaway.*
3,424,941 Transistor Deflection Circuit With Clamper Means, *James A. McDonald and John Brewer Beck.*
3,424,942 Auxiliary Beam Deflection Yoke, *Robert L. Barbin.*
3,425,001 Dielectrically-Loaded, Parallel-Plane Microwave Ferrite Devices, *Bernard Hershenov.*
3,425,021 Method and Apparatus for Connecting Leads to a Printed Circircuit Board, *Robert S. Fow and Joel R. Oberman.*

February

3,426,210 Control Circuit for Automatically Quantizing Signals at Desired Levels, *Julius Agin.*
3,426,220 Heat-Sensitive Seal for Thermionic Converters, *Fred G. Block and William B. Hall.*
3,426,235 Pickup Device, *Otto H. Schade, Sr.*
3,426,344 Character Generator for Simultaneous Display of Separate Character Patterns on a Plurality of Display Devices, *Robert John Clark.*
3,427,453 System for Switching the Attitude Reference of a Satellite from a First Celestial Body to a Second Celestial Body, *William Lee Gill and Harold Perkel.*
3,427,460 Beam-of-Light Transistor Utilizing P-N Junctions Which are Non-Abrupt and Non-Tunneling With a Base Region of Degenerate Material, *Hans P. Kleinknecht.*
3,427,509 Asymmetrical Triggering Diode Composed of Three Opposite Conductivity Regions, *Harry Weisberg.*
3,427,511 High Frequency Transistor Structure with Two-Conductivity Emitters, *Ronald Rosenzweig.*
3,427,514 MOS Tetrode, *John Olmstead, Lewis A. Jacobus, Jr., and Eleftherios G. Athanassiadis.*
3,427,515 High Voltage Semiconductor Transistor, *Adolph Blicher and Bohdan R. Czorny.*
3,427,631 Light Beam Recorder Using Vibrated Lens System, *Philip J. Donald.*
3,428,452 Photoconductive Compositions and Electrophotographic Recording Elements Made Therefrom, *Edward C. Giaimo, Jr.*
3,428,845 Light-Emitting Semiconductor Having Relatively Heavy Outer Layers for Heat-Sinking, *Herbert Nelson.*
3,428,854 Temperature Compensation of Deflection Circuits, *James A. McDonald.*
3,428,855 Transistor Deflection Control Arrangements, *James A. McDonald.*
3,428,857 Step Recovery Damper Diode for Retrace Driven Horizontal Deflection Circuits, *Richard C. Lemmon.*
3,428,885 Voltage Regulated Power Supply Including a Breakdown Device and Means Tending to Keep the Current Flow Therethrough Constant, *David Wilson Hall, II.*
3,428,900 Distributed Feedback Frequency Compression in Frequency Modulation Reception, *Arnold Newton.*
3,429,030 Method of Fabricating Semiconductor Devices, *Matthew M. Bell.*
3,429,033 Method of Securing a Rod to a Supporting Structure, *John David Callaghan.*
3,430,071 Logic Circuit, *Alfredo S. Sheng.*
3,430,075 Highly Stable Pulse Generator, *Robert A. Gange and John F. Thompson.*
3,430,110 Monolithic Integrated Circuits with a Plurality of Isolation Zones, *Haig Goshgarian.*
3,430,154 Circuit for Stabilizing the DC Output Voltage of a Gain Controlled Amplifier Stage in a Direct Coupled Integrated Circuit Signal Translating System, *Leopold A. Harwood.*
3,430,155 Integrated Circuit Biasing Arrangement for Supplying V_{be} Bias Voltages, *Leopold A. Harwood.*
3,430,207 Vector Display System, *William J. Davis.*

March

3,431,437 Optical System for Performing Digital Logic, *Walter F. Kosonocky.*
3,431,505 Emitter Follower Circuit Having Substantially Constant Current Emitter Supply, *Michael V. D'Agostino.*
3,431,890 Apparatus for Replenishing Developer in an Electrophotographic System, *Russell R. Ulary.*
3,432,035 Document Handling Apparatus, *Robert L. Adams.*

3,432,718 Television Focus Voltage Supply, *Joseph O. Preisig.*
3,432,720 Television Deflection Circuit with Linearity Correction Feedback, *Eduard R. Brunner.*
3,432,785 Coil Form, *Gené R. Solmos.*
3,432,920 Semiconductor Devices and Methods of Making Them, *Ronald Rosenzweig.*
3,433,932 Punched Card Reader, *William Rolke.*
3,433,993 Time Switch Controlled Energizing Circuit for Automatic Degaussing Apparatus, *Ronald R. Norley.*
3,434,000 Stabilization of Television Deflection Circuits, *James Alexander.*
3,434,014 Packaging of Electrical Equipment, *Ralph Taynton.*
3,434,019 High Frequency, High Power Transistor Having Overlay Electrode, *Donald R. Carley.*
3,434,021 Insulated Gate Field Effect Transistor, *Steven R. Hofstein.*
3,434,058 Ring Counters Employing Threshold Gates, *Robert O. Winder.*
3,434,112 Computer System Employing Elementary Operation Memory, *Richard H. Yen.*
3,434,119 Magnetic Memory Employing Stress Wave, *Lubomyr S. Onyshkevych.*
3,434,121 Cryolectric Memory System, *Robert A. Gange.*
3,434,123 Sense Amplifier for Magnetic Memory, *Robert A. Williams.*
3,434,156 Write Verification for a Recording System, *Emrys C. James.*
3,434,876 Photosensitive Cathodes, *Richard G. Stoudenheimer and Daniel L. Thoman.*
3,434,877 Metallic Connection and the Method of Making Same, *Robert S. Degenkolb and William H. Liederbach.*
3,435,129 Circuit for Distinguishing Interrupt Signal from Other Signals, *Robert A. Rodner.*
3,435,134 Digital Television Data Compression System, *Gerald P. Richards.*
3,435,138 Solid State Image Pickup Device Utilizing Insulated Gate Field Effect Transistors, *Harold Borkan.*
3,435,276 Convergence Apparatus for Nullifying Unwanted Induced Deflection Currents, *Gene Karl Sendelweck.*

AUTHORS

N. K. CHITRE received the B.Sc. and M.Sc. degrees in Physics from the Banaras Hindu University in 1953 and 1955, respectively, and the M. Tech. degree in Electronics from the Indian Institute of Technology, Kharagpur, in 1956. After a year with Van der Heem, N.V., the Hague, he studied at the Imperial College, London, where he received his diploma (D.I.C.) and, in 1962, the Ph.D. degree of the University of London. In March 1963, Dr. Chitre joined the RCA Victor Co. Ltd., Montreal, where he has worked on microwave communications systems, both overland and satellite, and designed various microwave multiplexing networks, filters, and ferrite components. For the past year, Dr. Chitre has been one of the core team working on a proposal for the Canadian Government involving a domestic communication satellite system. Dr. Chitre is a Member of I.E.E.

JOSEPH DRESNER received the B.S. degree in 1949 and the M.S. in physics in 1950 from the University of Michigan. From 1950 to 1953, he did research on the medical uses of high-energy x-rays at the Hospital for Joint Diseases in New York. He was research assistant at the Laboratory of Professor Kallmann at N.Y.U. in 1953-1958, at which time he did research on luminescence in solids. He received the Ph.D. in physics in 1958 from N.Y.U., following which he joined the Technical Staff of RCA Laboratories. Since that time Dr. Dresner has done research on television pickup tubes and on the study of electronic processes in photoconductors and insulators.

Dr. Dresner is a member of Sigma Xi and Sigma Pi Sigma.

ISTVAN GOROG received the B.Sc. degree in Electrical Engineering in 1961 from the University of California, Berkeley, and subsequently, the M.Sc. (1962) and Ph.D. (1964) degrees from the same University. His doctoral studies concerned radiation losses from high-temperature plasmas as possible sources of light. Between 1957 and 1964, he was employed by the Wesix Company, San Francisco, studying the natural ion content of air; the E-H Laboratories, Oakland, developing microwave circuit components; and with the University of California Electronics Research Laboratories working on lasers and plasmas. He joined RCA Laboratories, Princeton, N. J., in 1964, where his research has centered on high-power high-efficiency gas lasers and laser components.

Dr. Gorog is a member of Eta Kappa Nu and the American Physical Society.

RICHARD E. HONIG received the BSEE from Robert College, Istanbul, Turkey, in 1938; the MS in physics from MIT in 1939 and the PhD in physics from MIT in 1944. He is an adjunct Research Professor at Rensselaer Polytechnic Institute. From 1941 to 1946, he devoted part time to teaching physics at MIT and part time to work in radiation chemistry. From 1946 to 1950, he was employed by Socony Vacuum Research Laboratories, where he conducted research in mass spectromety, studying in particular the ionization of gases. He joined RCA Laboratories in the fall of 1950 and he has been engaged in solid state research, including the analysis of solids by mass spectrometry, vaporization studies of Group 4B elements, and the sputtering of surfaces by low energy positive ions. In 1955-56, on a year's leave of absence, he studied vaporization phenomena at the University of Brussels. More recently, he has critically reviewed vapor pressure data of the elements and worked on various types of ion sources and detectors. This includes studies of laser-induced emission of charged particles from solid surfaces.

Dr. Honig is a Fellow of the American Physical Society and a member of Sigma Xi.

JOHN J. HUGHES attended the 7th Army Electronics School in Germany and is presently attending Middlesex County College. He joined ITT Federal Laboratories in 1950, where he worked in the Chemical Department, the Countermeasures Department and the Microwave Tube Department. From 1958 to 1961 he was assigned to Associated Testing Laboratories as a representative of ITT, where he monitored and evaluated the environmental testing of microwave tubes. In 1962 he joined the RCA Electronic Components, Harrison, New Jersey, where he was a production foreman in the Microwave Tube Division. In 1963 he joined the Microwave Research Laboratory at RCA Laboratories, Princeton, New Jersey, where he has worked on plasma-tube studies, klystron design, and integrated solid-state microwave techniques. He has worked on the "Blue Chip" program since its inception and participated in the work on microstrip properties and the development of the integrated receiver.

Mr. Hughes is a member of the Institute of Electrical and Electronics Engineers.

DEAN A. KRAMER received his Associate in Engineering degree from the Pennsylvania State University in 1955. From 1955 until 1957 he worked at the Bell Telephone Laboratories, Murray Hill, N. J., where he was engaged in the development of a 1 MHz submarine cable tube. Upon joining RCA Laboratories in 1957, he engaged in the study of the band structure of semiconductor compounds through the use of infrared spectroscopy and, later, lasers. Since 1965 he has worked with the mass spectrograph and is presently involved in the application of a mass spectrometer to gas analysis.

CHANDRA M. KUDSIA received his B.Sc. degree in Physics from Delhi University in 1961 and B.E. degree in Electrical Communication Engineering from Indian Institute of Science, Bangalore, in 1964. In 1966, he received his M.Eng. degree in Electrical Engineering from McMaster University, Hamilton, Ontario. After a year with Amphenol Canada Limited, Toronto, where he was involved in the design of special rf and microwave connectors, he joined RCA Victor Company, Limited, Montreal, in May 1967. At RCA he has worked on the design of microwave components and sub-systems for high-quality microwave links and ground stations for Satellite Communications. He is presently engaged in the feasibility study of certain microwave components for the Canadian Communication Satellite. Mr. Kudsia is a registered Professional Engineer of the Province of Ontario and a member of the Institute of Electrical and Electronics Engineers.

ROBERT J. LINHARDT received a BEE from Manhattan College in 1948, an MS from Stevens Institute of Technology in 1951, and an MSE in Systems Engineering and Operations Research from the University of Pennsylvania in 1967. In 1955, when he joined RCA, he was engaged in the development of analog and digital computers for various military programs. In 1960, Mr. Linhardt transferred to the Advance Development group of the RCA Information Systems Division and worked in the system and logic design of ultra-high-speed digital computers. Since the beginning of 1966, he has been involved in the system design of digital computers using large-scale integration. Mr. Linhardt is a licensed professional engineer in New York and New Jersey, and a senior member of the Institute of Electrical and Electronics Engineers.

HENRY S. MIILLER received the BSEE degree from the University of Illinois in 1958 and the MSEE degree from the University of Pennsylvania in 1960. He has done additional graduate work at the University of Pennsylvania in the field of computer and information sciencies. Mr. Miiller joined RCA Laboratories in 1958, working on semiconductor devices and circuits, and microwave parametric phase-locked-oscillator and tunnel-diode circuits for kilomegahertz computer circuits. He has also contributed to the fields of tunnel-diode transistor hybrid circuits, majority-logic synthesis by geometric means, and resolution of multiple responses in associative memories. Currently, he is working on the development of computer architectures suited to large-scale integration. Mr. Miiller is a member of Eta Kappa Nu and the Institute of Electrical and Electronics Engineers.

LOUIS S. NAPOLI received his B.S. in 1959 and the M.S. in 1961 in Electrical Engineering, both from Rutgers University. He has pursued further studies in electrophysics at the Polytechnic Institute of Brooklyn. He joined the technical staff of RCA Laboratories in June, 1959, and has engaged in research in phase-locked oscillators as a microwave logic device. He has specialized in research relating to microwave phenomena in gaseous plasmas, solid-state microwave devices, and is now engaged in research on solid-state microwave integrated circuits. His work in collaboration with Dr. George Swartz on amplification at 24 Gc by the interaction of an electron beam with a cesium plasma was cited by Industrial Research Magazine as one of the 100 most important achievements in 1963.

Mr. Napoli is a member of Sigma Xi, the Institute of Electrical and Electronics Engineers, Tau Beta Pi, and Eta Kappa Nu.

EDWARD C. ROSS received the BSEE degree from Drexel Institute of Technology in 1964 and the MSE, MA, and Ph.D. degrees from Princeton University in 1966, 1967 and 1969, respectively. He joined RCA Laboratories in 1964, where he has been working in the fields of integrated arrays of MOS field-effect transistors, the electrical and physical characteristics of silicon-on-sapphire films, and the physics and application of field-effect storage transistors.

Dr. Ross is a member of Tau Beta Pi, Eta Kappa Nu, and the Institute of Electrical and Electronics Engineers.

Joseph H. Scott received the A.B. degree in chemistry from Lincoln University, Pennsylvania. In 1958 he attended graduate school at Howard University, Washington, D.C., and is presently pursuing a degree in Electrical Engineering at Newark College of Engineering. In 1959, he joined RCA Electronic Components and Devices, Somerville, N.J., where he engaged in research and development of semiconductor devices. He has worked on GaAs solar cells, p-n junction unipolar devices, high-frequency high-power bipolar transistors and, most recently, MOS transistors. Together with J. A. Olmstead he did the initial work on multi-emitter "overlay" transistors. In 1966, he joined RCA Laboratories, Princeton, N.J. Mr. Scott is a member of the Electrochemical Society.

Fred W. Spong received the B. S. degree in physics from the University of Utah, Salt Lake City, in 1958, and the Ph.D. degree in physics from the University of California at Berkeley. His dissertation involved an experimental investigation in Fermi surface physics, namely cyclotron resonance in aluminum. In 1964 he joined RCA Laboratories, Princeton, N. J., where his studies have centered on high power, high efficiency gas lasers.

Dr. Spong is a member of the American Physical Society, Sigma Ki, and Phi Beta Kappa.

J. Torkel Wallmark received the degrees of Civilingenjor in electrical engineering in 1944, Teknologie Licentiat in 1947, and Teknologie Doktor in 1953, from the Royal Institute of Technology, Stockholm, Sweden. From 1944 to 1945 he was a vacuum-tube Designer for the A. B. Standard Radiofabrik, Stockholm. He was with the Royal Institute of Technology as a Research Assistant on vacuum-tube problems from 1945 to 1953. At the same time he spent periods at the RCA Laboratories in Princeton, N. J., and at Elektrovarmeinstitutet and Tekniska Forskningsradet, both in Stockholm, engaged in work on secondary emission tubes, semiconductors, and research administration. In 1953 he joined RCA Laboratories, Princeton, N. J., where he has been engaged in research on magnetrons, color television, semiconductor devices, and integrated electronics. He is presently a professor in the Electrical Engineering Department of Chalmers University in Gothenburg, Sweden.

RICHARD WILLIAMS received the degree of A.B. in chemistry from Miami University in 1950 and the Ph.D. in physical chemistry from Harvard University in 1954. After three years spent as an instructor in physical chemistry at Harvard, he joined the technical staff of RCA Laboratories in 1958. Since coming to RCA Laboratories, he has been engaged in experimental work on high electric fields in insulators, properties of interfaces between insulators and other materials, liquid crystals and ferroelectrics. Dr. Williams has been granted a Fulbright-Hays Fellowship and is presently lecturing and conducting research in physics at the Departamento de Física, Escola de Engenharia, São Carlos, Brazil. He is a member of the American Physical Society.

C. R. WRONSKI obtained the B.Sc. in 1960 and the PhD in 1963 in physics from the Imperial College, London University. His thesis was devoted to the subject of electron diffraction and thin films. From 1963 to 1966, he was with the 3M Research Laboratories in St. Paul, Minnesota, working on photoconductivity and thin Films. Since joining RCA Laboratories in 1966, he has worked on thin films and metal-semiconductor barriers. Dr. Wronski is a member of the American Physical Society.